DISS. ETH Nr. 19530

Dielectric Coordination of High Voltage Gas Circuit Breakers

A dissertation submitted to
ETH Zurich

for the degree of
Doctor of Sciences

presented by
Philipp Simka
MSc ETH, Electrical Engineering and Information Technology

Date of birth
16. December 1978

citizen of
Tomils, GR

accepted on the recommendation of:
Prof. Dr. C.M. Franck
Prof. Dr. J. Kindersberger

2011

Acknowledgements

First and foremost I thank Prof. Christian M. Franck for his supervision and guidance during my PhD project - he showed me the effectiveness and inspiring power of scientific discussion. I also thank Prof. Klaus Fröhlich for the initiation of this research project and his faith in my experimental skills. I thank Prof. J. Kindersberger for being a member of my thesis committee.
I would like to thank my office colleague Dr. U. Straumann for the great working atmosphere, his friendship and the valuable scientific advice through the last four years. His preciseness, analytical and mathematical skills are very impressive and helped me a lot during my PhD project.
I am grateful for the collaboration with Martin Seeger from ABB Corporate Research, Max-Steffen Claessens and Per Skarby from ABB Power Products and I thank ABB Switzerland Ltd. for the financial support.
Special thanks goes to Hans Jürg Weber and Henry Kienast from the High Voltage Laboratory, ETH Zurich. They taught me a lot about high voltage laboratory techniques and mechanical constructions. I also want to thank Hans-Rudolf Benedickter from the Microwave Electronics Laboratory of ETH Zurich who showed me the beauty of high frequency measurements.
Thanks goes to all the students who worked for this project during the past years. Special thanks goes to Rowan Sinton from the University of Canterbury, Christchurch. His constructive and analytical skills are very well developed and he made a valuable contribution to the project.
Last but not least I thank my parents for their constant support throughout the years. Special thanks goes to my amazing wife Tatiana. She supports me in everything I do and helped me keep up my spirit throughout the last four years.

Zürich, December 2010

Philipp Simka

Contents

Abstract

High voltage circuit breakers serve two important functions in the electrical power grid. On the one hand they regulate the power flow by connecting and disconnecting further network elements and on the other hand they have to separate faulty components from the grid quickly and reliably. The requirement for interruption capability of circuit breakers is constantly increasing and these days circuit breakers are capable of switching approximately 20 GVA per interrupting unit. This performance is reached by SF_6 insulated circuit breakers of puffer- or self-blast type.

The requirements to carry the nominal current with low losses in closed position and to control a high power switching arc are conflictive with respect to an optimization of the contact system. This challenge is solved by the use of two different contact systems, each optimized for their respective purpose. These are the main and the arcing contacts. For a safe and reliable operation of the circuit breaker it is necessary, that the switching arc does not occur on the main contacts. A proper dielectric coordination of the contact system allows control of arc formation and localization.

The objective of this thesis was to evaluate and investigate different mechanisms which disturb the dielectric coordination of high voltage circuit breakers. Two different approaches were followed: First, a distortion, caused by the overlap of breakdown probability curves of single contacts when composing the multi-contact system was analyzed. Second, a possible distortion by the occurrence of very fast transient voltages in the switching chamber was investigated. Due to their different causal nature the two approaches were called implicit and explicit distortion of dielectric coordination, respectively.

Implicit distortion was investigated by electrostatic field analysis of contact arrangements and by the development and construction of an experimental setup to accurately determine and compare breakdown probabilities of single and multi contact systems.

Explicit distortion was investigated through the development, implementation and validation of an equivalent network model. Using this model, transient simulations revealed the occurrence of certain over-voltages based on the geometrical characteristics of the circuit breaker.

Investigation of the implicit distortion mechanism uncovered an unexpectedly wide difference in breakdown voltages due to the voltage polarity applied. However, not only the breakdown voltage but also the breakdown distribution on arcing and main contacts was significantly influenced by the voltage polarity. In a contact vs plane electrode arrange-

ment, breakdowns occurred on the main contact with 23% percent probability although the maximum electric field on the arcing contact was 40% elevated. These effects could neither be foreseen nor explained through the evaluation of breakdown probabilities of single contact arrangements. In a complete circuit breaker contact system this effect was maintained however attenuated as the main contact breakdowns happen less frequently when both contact sides are coordinated.

The transient simulation within single interrupting units revealed an increase in very fast transient voltages dependent on the length, shape and connection of the inner contacts albeit the effect was not very pronounced. Although breakdown in SF_6 excites traveling wave phenomena, the very inner structure of the circuit breaker is too short to provoke significant potential differences between main and arcing contacts. The highest influence is achieved by changing load elements attached to the circuit breaker and not the circuit breaker geometry. Analysis of double interrupting units showed that a contact system experiences high electrical stress in terms of frequency and amplitude after the breakdown of the adjacent interruption unit. This resulted in a strongly increased breakdown probability on the main contact whereas no significant voltage difference across main and arcing contacts was detected. This problem can be mitigated through the application of grading capacitors but their influence depends on the geometry and the high frequency characteristics of the specific item used.

Based on these findings, design criteria for future gas-insulated high voltage circuit breaker contact systems can be extended:

If the maximum electric field at certain electrodes is used as coordination and breakdown criteria it has to be evaluated through breakdown experiments with the combined contact system. Analysis of single contacts and extrapolation of these results to combined contact systems does not result in a correct design.

Further, the breakdown probability on the main contact system can generally be decreased by coordinating both sides of the contact system.

Zusammenfassung

Hochspannungsleistungsschalter übernehmen im elektrischen Verbundnetz zwei wesentliche Aufgaben. Zum einen steuern sie den Lastfluss im Netz durch das Zu- und Abschalten von Netzelementen und zum anderen müssen sie fehlerhafte Komponenten schnell und zuverlässig vom Netz trennen können. Die Anforderung an Hochspannungsschalter steigen stetig. So beträgt die Unterbrechungskapazität einer einzelnen Schaltkammer in modernen Hochspannungsschaltern um die 20 GVA. Diese Leistung wird erreicht durch SF_6 isolierte Schalter, die nach dem Puffer- oder Selbstblasprinzip arbeiten.
Die Anforderungen an ein Kontaktsystem, gleichermassen optimale Leitfähigkeit im geschlossenen Zustand und Widerstandsfähigkeit gegen den Schaltlichtbogen zu besitzen sind gegensätzlich im Bezug auf die Optimierungsstrategie für das Kontaktsystem. Dieses Problem wird üblicherweise durch die Verwendung von zwei verschiedenen Kontakten, optimiert für die jeweilige Anforderung, gelöst: Die Abbrand- und Nennstromkontakte. Für den sicheren und zuverlässigen Betrieb des Leistungschalters muss sichergestellt werden, dass der Lichtbogen nicht auf dem Nennstromkontakt auftritt. Eine angemessene dielektrische Koordination des Kontaktsystems erlaubt es, den Ort der Lichtbogenentstehung zu kontrollieren.
Das Ziel dieser Arbeit war verschiedene Mechanismen, welche die dielektrische Koordination in Hochspannungsschaltern stören können, zu evaluieren und zu untersuchen. Zwei unterschiedliche Ansätze wurden verfolgt: Zum einen, wurde eine Störung der dielektrischen Koordination, hervorgerufen durch die Überlappung der Durchschlagswahrscheinlichkeitskurven verschiedener Einzelkontakte bei einer Zusammenführung zum Gesamtsystem, analysiert. Zum anderen wurde eine mögliche Störung durch das Auftreten von sehr schnellen transienten Spannungen innerhalb der Schaltkammer untersucht.
Aufgrund der unterschiedlichen, zugrunde liegenden Kausalität wurden diese beide Mechanismen als implizite und explizite Störung der dielektrischen Koordination bezeichnet.
Die implizierte Störung wurde durch elektrostatische Feldanalyse des Kontaktsystems und die Entwicklung und den Aufbau eines experimentellen Versuchsstandes zu einer detaillierten Untersuchung und einem Vergleich von Durchschlagswahrscheinlichkeiten einzelner Kontakte oder eines Kontaktsystems untersucht. Die explizite Störung wurde durch die Entwicklung, Berechnung und experimentelle Validierung eines elektrischen Ersatzmodell untersucht. Simulationen transienter Spannungen innerhalb dieses Modells offenbarten das Auftreten von definierten Überspannungen die auf die Geometrie des

Leistungsschalters zurück zu führen sind.
Die Untersuchung der impliziten Störungsmechanismen zeigte unerwartet grosse Unterschiede in den Durchschlagsspannungen in Abhängigkeit der angelegten Spannungspolarität. Jedoch war nicht nur die Durchschlagsspannung sondern auch die Durchschlagsverteilung zwischen Abbrand und Nennstromkontakt massgeblich von der angelegten Spannungspolarität abhängig. In einer Kontakt-Platte Anordnung erfolgte ein Durchschlag am Nennstromkontakt mit einer Wahrscheinlichkeit von 23% obwohl das maximale elektrische Feld am Abbrandkontakt 40% überhöht war. Dieser Effekt konnte durch die experimentelle Untersuchung einzelner Kontakte weder vorhergesehen noch erklärt werden. Im vollständigen Kontaktsystem war dieser Effekt immer noch vorhanden, wenn auch in abgeschwächter Form, da die Anzahl nennstromseitiger Durchschläge verringert wurde, wenn beide Seiten des Kontaktystems koordiniert waren.
Die transiente Simulation bei Einkammer Schaltern zeigten eine Verstärkung sehr schneller transienter Spannungen abhängig von der Länge, Form und Verbindung der inneren Kontakte, doch der Effekt ist nicht sonderlich ausgeprägt. Obwohl Durchschläge in SF_6 Wanderwellen im Schalter auslösen, ist die innerste Struktur des Schalters zu klein um massgebliche Potentialunterschiede zwischen Abbrand- und Nennstromkontakten hervorzurufen. Am meisten wird das System nicht durch eine Änderung der Leistungsschaltergeometrie sondern durch den Austausch von Lastelementen, die mit dem Leistungsschalter verbunden sind, beeinflusst. Die Untersuchung von Zweikammer Schaltern zeigte, dass das Kontaktsystem erheblicher Beanspruchung bezüglich Spannungsamplitude und Frequenzinhalt ausgesetzt wird, wenn ein Durchschlag in der benachbarten Schaltkammer erfolgt. Dieser Vorgang hatte eine dramatische Erhöhung der Durchschlagswahrscheinlichkeit am Nennstromkontakt zur Folge, obwohl kein wesentlicher Unterschied zwischen den zeitlichen Potentialverläufen an Abbrand- und Nennstromkontakt festgestellt werden konnte. Dieser Effekt kann durch den Einsatz von Steuerkondensatoren verringert werden, wobei jedoch deren Einfluss von der Geometrie und dem Hochfrequenzverhalten des jeweilig eingesetzten Produkts abhängig ist.
Aufbauend auf diesen Ergebnissen können die Designrichtlinien für zukünftige gasisolierte Hochspannungsschalter ergänzt werden:
Wenn das maximale elektrische Feld einer Elektrode als Koordinations- und Durchschlagskriterium verwendet wird, muss es durch Durchschlagsversuche an der kompletten Kontaktgeometrie evaluiert werden. Die Untersuchung von Einzelkontakten und die Extrapolation der Ergebnisse auf kombinierte Anordnungen führt nicht zum richtigen Resultat.
Im weiteren kann die Durchschlagswahrscheinlichkeit an den Nennstromkontakten allgemein verringert werden, wenn beide Seiten des Kontaktsystems koordiniert werden.

1. Introduction

1.1. The Power Grid and the High Voltage Circuit Breaker

Through the last century, electricity has become the world's most reliable and flexible form of power. European and global demand is increasing (see Fig. 1.1) and in the future, electricity will take on duties which were fulfilled by limited sources of energy like fossil fuels previously. Due to geographical, economical or political constraints, the vast production of electric power is rarely in the vicinity of the major consumption. This implies the need for electric power transmission. The respective transmission lines connect areas which can be several hundreds up to a few thousand kilometers apart. In order to achieve a maximal reliability and security of the supply system, the transmission lines are interconnected and form a large scale grid with a large number of consumers and producers.
The power loss through transmission is inversely proportional to the voltage level applied. Consequently, the usage of the maximum possible voltages would be favorable. In contrast, the reliable and secure utilization of very high voltages requires complicated and expensive engineering. Hence, the voltage level used is usually a compromise between optimal economical and technical solution. This compromise is again variable with respect to the environment and results in many different standardized voltage levels which cover a range of approximately three orders of magnitude. Not only does the transmission line have to be designed for the respective voltage level, but also any other component of the power grid like transformers, bushings, surge arrester, disconnect switches and circuit breakers have to be optimized.

High voltage circuit breakers are an essential part of contemporary electrical power grids. They serve two main functions: First, circuit breakers direct the flow of electrical power through the network by connecting or disconnecting different elements with the grid. Second they isolate specific elements from the network in case of a fault. These main functions imply three basic requirements the circuit breaker has to fulfill:

1. In open position it shall be a perfect insulator, able to withstand all possible voltages according to its ratings.

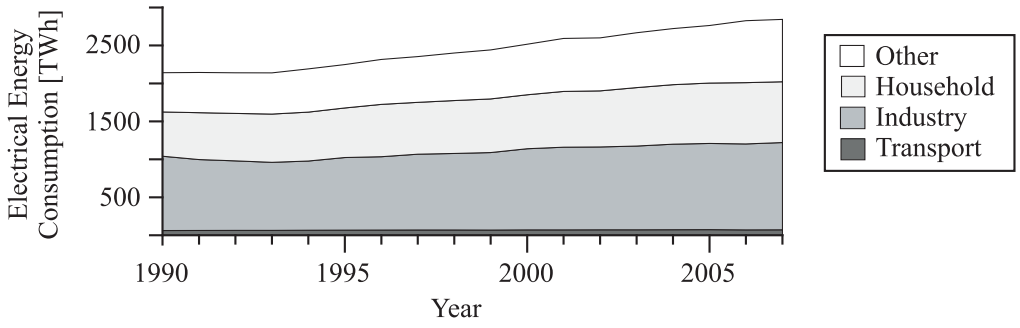

Figure 1.1.: Electrical energy consumption in the European Union from 1990 to 2007 [1] shows a 32% growth within 17 years

2. In closed position it shall be a perfect conductor, carrying its rated nominal current with the lowest possible losses.

3. Any switching operation shall be executed with maximum reliability especially in the rare but most severe case of interrupting a short circuit current.

The growing demand as depicted in Fig. 1.1, has to be fulfilled by increased production and higher transmission capacity. Increasing transmission leads to an increasing prospective short circuit current of a certain transmission line. To date, the development of high voltage circuit breakers kept up with the need for higher ratings as well as with the demand for smaller, cost effective items. The interruption capability of high voltage circuit breakers was mainly improved through the application of different insulation media. The transition from oil to SF_6 insulated circuit breakers around the early seventies represents one of the major steps in the increase of interruption capability. The subsequent invention of self-blast and double motion type circuit breakers led to a significant decrease in required drive energy and therefore to additional compactness and cost effectiveness. Today, SF_6 insulated high voltage circuit breakers are state of the art.

The basic working principle of a SF_6 insulated high voltage circuit breaker is explained by describing an interruption sequence of a puffer breaker whose layout is schematically depicted in Fig. 1.2. The general geometry of the circuit breaker can be divided into three major parts:

1. Gastight, pressurized enclosure.

2. Contact system, referred to as fixed and moving contact in Fig. 1.2.

3. Main insulator.

The interruption of the prevailing current is performed basically by the mechanical separation of the contacts, whereas either one contact side (depicted in Fig. 1.2) or both can

be accelerated. The main insulator provides a stable mechanical connection between the two contact sides.
In closed position, all contacts touch and form a conductive path with low resistance. Especially the main contacts are designed for minimal contact resistance. In order to interrupt this conductive line, a drive pulls the control rod and initiates the separation of the contacts. The main contacts separate first, followed by the arcing contacts. Hence, the current through the breaker commutates from the main to the arcing contacts. Thus the main contacts are protected from the subsequent switching arc. As soon as the arcing contacts separate, an electrical arc forms across the widening gap. Simultaneously, the gas pressure in the compression volume rises due to the decrease of volume[1]. At the zero crossing of the alternating current, the switching arc extinguishes due to the absent energy input at that very instant in time. The pressurized gas in the compression volume flows through the nozzle channel into the gap between the contacts, cooling the present ionized gas. To achieve a successful interruption this cooling process needs to be stronger than the reheating of the gas by the post arc current that flows after current zero. The specific time frame in which this happens is generally called the *thermal recovery phase* and is for SF_6 typically smaller than $1\,\mu s$.
Once the flow of current is stopped the gap between the electrode represents a high resistive path with a corresponding voltage drop, the recovery voltage. In the following *dielectric recovery phase*, the contacts have to be separated fast in order to avoid a breakdown due to this rising voltage. The recovery voltage can have different amplitudes and frequencies depending on the network topology [2]. If the breaker manages to handle the dielectric recovery phase without re-ignition, the interruption process is complete.

The circuit breaker as depicted in Fig. 1.2 is designed to meet certain requirements in withstand-voltage and current interruption capability. For higher rated voltage it is common practice to construct circuit breakers with several interrupting units in series.

1.2. Insulation Coordination and Dielectric Coordination

The International Electrotechnical Commission (IEC) introduced and defined the horizontal standard *Insulation Co-ordination* [3]. This standard specifies requirements for high voltage apparatus with the purpose to render them stable against the prevailing electric stresses without using excessive security margins. In this regard stability means the absence of insulation failure through breakdown.
Proper insulation coordination prevents high voltage apparatus from breakdowns and

[1] The pressure rise in self-blast circuit breakers is additionally boosted by the inflow of hot gas from the switching arc itself.

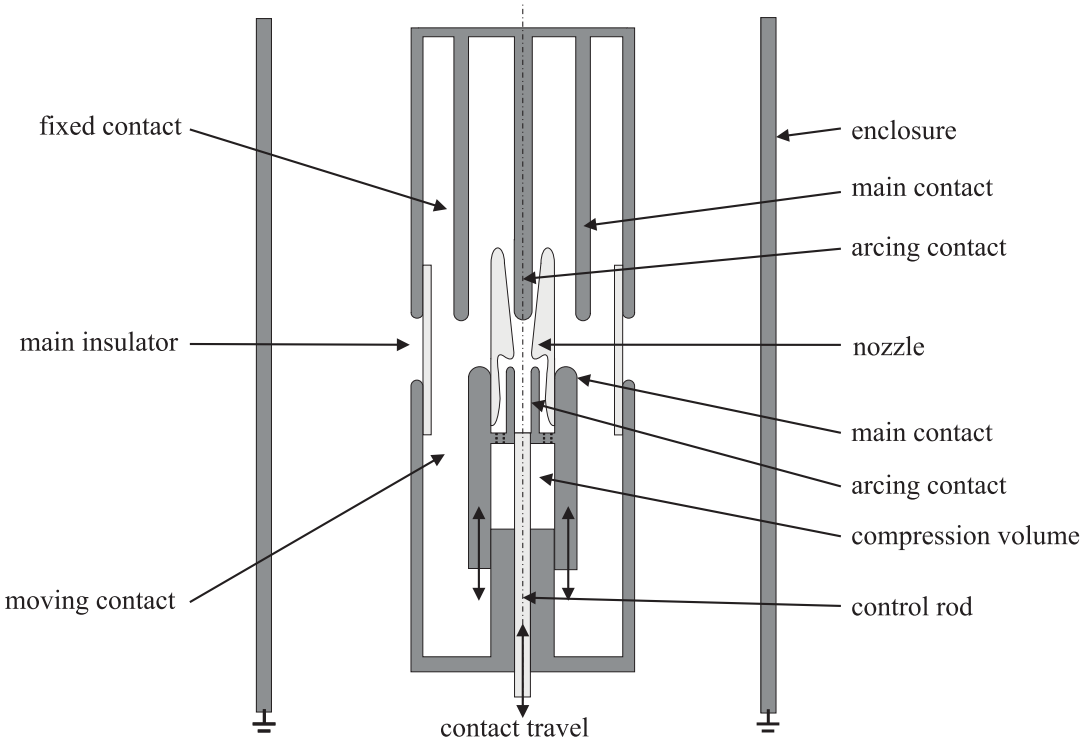

Figure 1.2.: Schematic drawing of a gas insulated, high voltage, puffer circuit breaker

consecutive damage. However, in the special case of high voltage circuit breakers, breakdown and arc formation between the contacts is inevitable (section 1.1) and therefore the insulation coordination is translated to dielectric coordination. The purpose of the dielectric coordination is not to avoid arc formation but to control arcing location and development in order to prevent a destruction of the circuit breaker. The dielectric coordination is therefore one of the most delicate design criteria in circuit breakers.
Dielectric coordination is achieved by regulating the location and strength of the electric field. The electric field between two electrodes is defined by the shape, the distance between and the potential difference of the electrodes. In order to roughly describe a field, the *field efficiency factor* η can be calculated [4]:

$$\eta = \frac{E_0}{E_{max}} = \frac{V}{dE_{max}} \tag{1.1}$$

This factor describes the ratio of the field strength of a homogeneous electric field E_0, determined by contact distance d and Voltage drop V and the maximum electric field strength E_{max} of an inhomogeneous electrode arrangement, having the same parameters V and d. Eq. (1.1) is only adequate to describe simple electrode arrangements since in more complicated setups the maximum electric field does not necessarily appear at the

point of shortest distance between two electrodes.
The major reason to control the strength of the electric field is its effect on the effective ionization-coefficient α^*. The parameter α^* is a measure for the number of ionizations along a certain path [5], [6]. Once it becomes positive, a path of ionized gas starts to grow which may induce a breakdown. As the arc formation is supposed to occur at the arcing contacts, the main criteria for the dielectric coordination can be derived:
The maximum electric field strength on the arcing contacts shall exceed the field strength on the main contacts if any of the field strengths is high enough $E \geq E_{crit}$ to induce a positive α^*.

1.3. Breakdown Prediction and Distortion of Dielectric Coordination

The evaluation of the maximum electrical field value at the respective electrode surfaces is a simple and indicative basis to estimate the breakdown voltage and the dielectric coordination of high voltage circuit breaker contact systems.
Although the basic physical principles of breakdown in SF_6, and its dependence on electric field distribution are known, it remains very difficult to predict breakdown voltages accurately. This fact is nicely illustrated through an investigation published in 2007 [7]. A benchmark circuit breaker contact system was given to six different manufacturers of high voltage circuit breakers with the task to determine the prospective breakdown voltage. The comparison between predicted and tested voltages showed a deviation between 2% and 42%. However, five of the six candidates predicted a breakdown voltage, lower than the measured voltage, what indicates that the design criteria includes a certain safety margin.
The determination of the breakdown voltage for a certain contact geometry is particularly difficult as several interfering factors are subject to a certain probability to occur. This results not only in an absolute breakdown voltage but in a breakdown-probability curve, characteristic for every contact and its environment. Whether the overlap of these curves in multi-contact systems can be represented by the maximum field criterion or not, is still to be determined.
Since the electric field is the basis of the design procedure, it has to be assured that its calculation represents the circuit breaker environment accurately. A wrong electric field calculation is quite likely based on missing or wrong input parameters. These could either be in the spatial or in the time domain.
An imprecise spatial domain is a consequence of neglecting elements which may arise during the operation of the circuit breaker and have a significant influence on the electric field

distribution. Candidate elements are space or surface charges and/or (semi-)conductive material deposition on the surface of the main insulator or the nozzle. Furthermore, damage on the conductive surfaces or micro-protrusions can lead to an electric field which is locally enhanced and therefore deviates from the calculated one.
The electric field calculation discussed so far implied an electrostatic or quasi-electrostatic image. However, this assumption is only correct if the investigated item is geometrically short in comparison to the electrical wavelength. If this condition is violated, an imprecision in the time domain is the consequence.
In the power grid there is only one transient event fast enough to provoke an electrodynamic field distribution; This is the formation of an arc and the consequent stepwise equalization of potentials leads to traveling wave phenomena and hence an non-electrostatic condition. This imprecision in time domain was investigated earlier in the context of disconnect switch induced VFT in Gas Insulated System (GIS) [8]. This phenomenon is known to have an impact on the insulation coordination of gas insulated equipment. Therefore this approach is the most promising for a distortion of the dielectric coordination.

1.4. Objective of the Thesis

Circuit breakers are subject to a constant development with the claim for higher performance at lower costs. As the design of the contact system (contacts and nozzles) represents the core of the circuit breaker, it is the principal subject of any design process. Improvements are rarely achieved by nozzle and contact changes but have to be adjusted and optimized according to the whole geometry of the breaker.
The objective of this thesis is to expand the knowledge of circuit breaker contact design by evaluating and investigating mechanisms which may lead to a distortion of the dielectric coordination and eventually to a breakdown between the main contacts.
These mechanisms are no problem for today's circuit breakers that are fully type tested but could become important in future in more compact designs with reduced security margins.
For the investigation of possible distortion mechanism of the dielectric coordination in high voltage circuit breakers two different strategic approaches were theoretically analyzed, experimentally explored and interpreted:

- Implicit distortion through the overlap of breakdown probability curves.
- Explicit distortion through the occurrence of VFT.

The present work is structured as follows: In the following chapter 2 a brief overview of the state of knowledge is given. The established experimental techniques to evaluate breakdown probabilities are presented as well as the basic mechanisms of VFT development

and propagation in GIS, concluding with possible effects on the withstand capability of SF_6 with respect to VFT.

In chapter 3 an experimental setup is described which was used to explore the implicit distortion of dielectric coordination. Measured breakdown probability distributions of different electrode combinations are presented and discussed in combination with electrostatic field calculation of the items investigated.

The investigation of the explicit distortion of the dielectric coordination is summarized in chapter 4. VFT promoting factors are evaluated by calculating an equivalent circuit model of the circuit breaker and corresponding simulations by using this model. The influence of these parameters was experimentally tested and is described and discussed at the end of the chapter.

The conclusion and outlook in chapter 5 concludes the work.

2. State of Knowledge

2.1. Breakdown Procedure in SF_6

Discharge inception requires a free electron in the gas volume as well as a present electric field to accelerate the electron. If the electron gains sufficient kinetic energy to ionize further gas molecules by collision ionization, the number of free electrons duplicates exponentially. In SF_6 this condition is fulfilled if the electric field exceeds a value of $E_{cr} = 89\,\mathrm{kV/cm\ bar}$. The growing electrode avalanche represents a self sustaining discharge if it reaches a size of approximately 10^6 [9] which is known as fulfillment of the streamer criterion [10]. In electrode arrangements with homogenous electric field, the fulfillment of the streamer criterion leads directly to breakdown. In strong inhomogeneous electrode arrangements the fulfillment of the streamer criterion either remains a stable discharge (corona) or grows through the electrode gap by consecutive streamer-leader transitions, finally leading to breakdown. The different steps of breakdown initiation are described in more detail in the following sections.

2.1.1. Origin of First Electron

The discharge initiating first electron originates either from the electrode surface or from the gas molecules. Within the gas, free electrons appear because of ionization process or as detachment from negative ions SF_6^-. The latter has been shown to play the major role in SF_6 insulated applications [11]. Conductive surfaces with high electric field stress emit electrons through field emission if a negative electric potential is applied. The necessary electric field has to be approximately $10^4 - 10^5$ kV/cm [5] and is consequently only exceeded in strong inhomogeneous electrode arrangements or in the microscopic range at micro protrusions or surface roughness.

2.1.2. Ionization and Recombination

The multiplication of a single electron to a space charge cloud is the product of ionization and recombination processes. Ionization due to an electric field is mainly based on collision ionization and quantified by the factor α determining the number of ionziations per unit length. The generation of free electrons by collision ionization is arrested by recombination of positive ions and electrons or more likely, by electron attachment to a

neutral SF_6 molecule. This rate is expressed by the recombination factor η. Deciding wether an electrode avalanche is growing is the difference of α and η expressed by the effective ionization factor $\alpha^* = \alpha - \eta$. Ionization and recombination factors are shown in Fig. 2.1 for SF_6 from approximations given in [12]. Both factors are dependent on the electric field and gas pressure whereas α^* is positive at electric fields, higher than $E_{cr} = 89\,\mathrm{kV/cm\ bar}$.

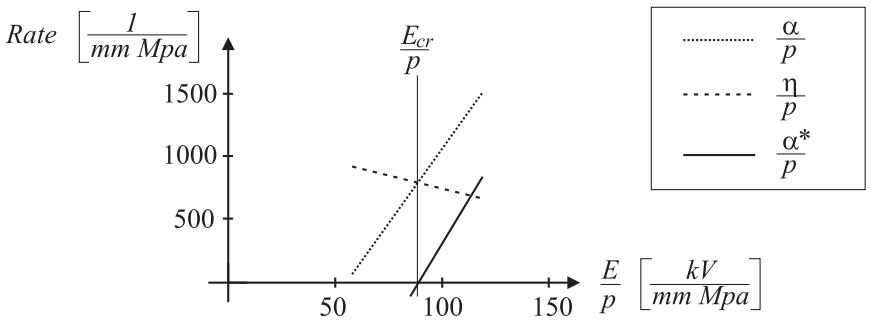

Figure 2.1.: Ionization, recombination and effective ionization coefficient as function of electric field. The effective ionization coefficient is bigger than 0 at approximately $E_{cr} = 89\,\mathrm{kV/cm\ bar}$ [12]

2.1.3. Streamer Breakdown

Starting with N_0 electrons, initiating collision ionization the number of electrons in the head of the avalanche at the point x within the gas volume is calculated by [9]:

$$N(x) = N_0 \cdot e^{\int_0^x \alpha - \eta dx} \tag{2.1}$$

$$N_0 = \text{Number of initial electrons} \tag{2.2}$$

If $N(x)$ reaches a value of $N_{crit} = 10^6 \ldots 10^8$ the prevailing electric field is significantly influenced by the presence of the moving negative electrons and the relatively static positive ions. This leads to an increased ionization and molecular excitation which leads to an increased photon density and consequently a further increase of ionizations providing first electrons for further avalanches. Often, the more convenient expression of the amplification factor k_{st} is used, whose boundaries determining the critical size of an avalanche of $13.8 \ldots 18.4$ represent the natural logarithm of N_{crit}. The described structure of several self sustaining avalanches is called Streamer. If the background field is homogenous or slowly decaying, the streamer will grow towards the opposite electrode, leading to a current peak if it reaches the electrode with following thermic ionization of the streamer and the formation of a high conductive arc. In the case of a strong inhomogeneous electric

field, recombination will dominate at a certain point and streamer growth is stopped. The corresponding, stable discharge is called corona.

Consequently the decay of the electric field between two electrodes determines the point in space, where the value α^* becomes negative and a certain avalanche ceases growing. This location is commonly denoted as decision length x_{crit} displaying the upper boundary in the streamer integral 2.1.

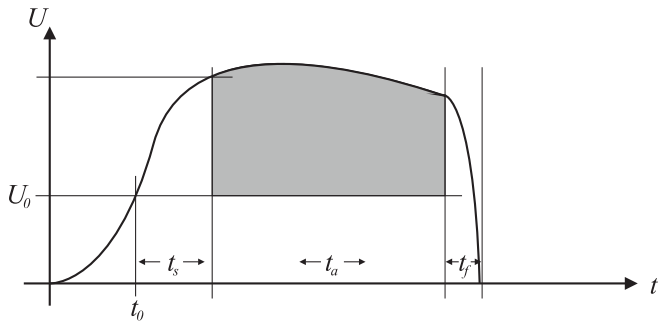

Figure 2.2.: Different temporal phases of gaseous discharge based on an impulse shaped voltage form [13]

Surface Roughness

In high pressurized SF_6 applications ($0.4 - 0.7$ MPa) the effective ionization coefficient grows rapidly if the critical electric Field E_{cr} is exceeded. Consequently the decision length is very small (several hundred μm) and an excess of E_{cr} is often equivalent to the fulfillment of the streamer criterion. This fact gains importance when electrodes with a certain surface roughness are used. Rough surfaces lead to microscopic electric field enhancements close to the electrode surfaces. This often leads to significantly higher electric fields compared to the macroscopic electric field. If the range of the field enhancement is similar to x_{crit} surface roughness leads to a strongly reduced breakdown strength of the electrode arrangement [14]. This effect can be accommodated by a reduction of E_{cr} when calculating the streamer criterion [12].

2.1.4. Temporal Development

Fig. 2.2 shows the temporal development of a breakdown sequence based on an applied impulse voltage form. The voltage starts rising at $t = 0$ and reaches a value U_0 after a time delay t_0 which causes an electrical field exceeding E_{cr}. Due to the statistical nature of first electron generation, the discharge initiation starts after a further time delay t_s, called the statistical time lag. The statistical time-lag is either determined by the electron-production rate from the electrode surface (field emission at negative

polarity) or by the electron production rate within the gas (at positive polarity). The time frame t_a following the statistical time-lag is the formative time lag representing the time necessary to build up a streamer which spans both electrodes and/or the time frame for repeated streamer-leader transition until the electrodes are bridged. To reach complete thermic ionization of the channel, a rather short time t_f is necessary.

In electrode arrangements where the statistical time delay is neglectable compared to the formative time delay, the grey marked area in Fig. 2.2 poses a certain area characteristic to describe the electrode arrangement.

The statistical time lag at positive polarity can be evaluated by the application of the volume-time law. It describes the probability to encounter a free electron, able to initiate an avalanche of sufficient size within a certain volume and time. The corresponding formula is [15]:

$$\begin{aligned} p &= 1 - e^{\int_{t_0}^{t_1} \int_V \frac{dn_e(E)}{dt}\left(1-\frac{\eta}{\alpha}\right) dV dt} \\ \frac{dn_e(E)}{dt} &= \text{Field dependent electron production rate} \end{aligned} \tag{2.3}$$

2.1.5. Streamer-Leader Transition

The streamer-leader transition describes the transformation of a low conductive space-charge filled volume into a high conductive plasma channel with low voltage drop. By the formation of a highly conductive leader, the electric field is severely changed and promotes further streamer development and further streamer-leader steps until the leader has crossed the whole gap [16], [17]. The formation of a leader requires a certain amount of heating energy in the streamer volume. So far, three different mechanisms have been identified to provide this heating on a molecular basis: Stem-, Precursor [17] and High-Frequency [18] or Energy [19] mechanism. Stem- and Precursor mechanism induce a leader by ion- or electron-current and corresponding ohmic heating whereas High-Frequency and Energy mechanism cause heating due to a displacement current.

Mechanism and Frequency Range

With respect to the formation of VFT within a GIS, the High Frequency Mechanism is explained in more detail. In the schematic drawing Fig. 2.3 a time dependent voltage $V(t)$ produces a time dependant electric field between the needle shaped and the plane electrode. Around the tip of the needle the electric field enhancement is very high implying a positive α^* and accordingly a streamer formation. Because of the high frequent oscillation of the voltage $V(t)$, a displacement current $i(t)$ is provoked which flows through the streamer volume and the stray capacitance between streamer volume and electrode. According to [18] the displacement current consists of two parts: The displacement current

through the stray capacitance $C(t)$ and the current induced through the time dependent change of capacitance through the change of streamer volume.

$$i(t) = C(t)\frac{\delta u(t)}{\delta t} + u(t)\frac{\delta C(t)}{\delta t} \tag{2.4}$$

If the ohmic heating of the streamer volume through the current $i(t)$ is high enough, a streamer-leader transition will take place. The high-frequency mechanism is dominant if the period T of the high frequent oscillation is shorter than an according precursor formation would take. This coherence is depicted in Fig. 2.3b.). The frequency range coincides with the values given in Tab. 2.2.

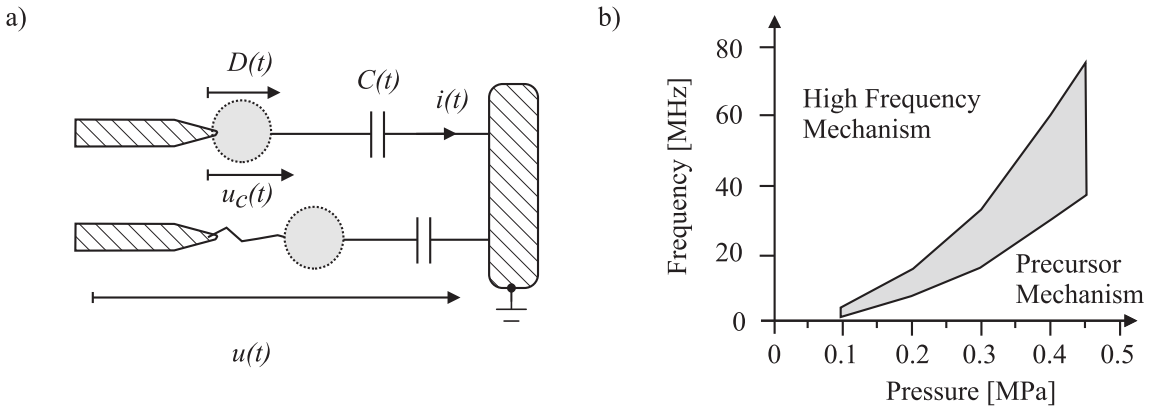

Figure 2.3.: Streamer-leader transition according to high frequency mechanism [18]:
a.) Basic mechanism
b.) Necessery frequency range of voltage applied

Influence of Field Efficiency

A streamer-leader transition according to the high frequency mechanism accounts for a present and stable streamer-corona. A stable streamer volume which does a priori not lead to breakdown is most easily achieved in a strong inhomogeneous electrode arrangement. Apparently, the effect of high frequency oscillating voltages is highest under this condition. Fig. 2.4 shows an overview of relative dielectric strength of different electrode arrangements [20] compared to the lightning impulse withstand voltage. According to [20] highly inhomogenous electrode arrangements show a lower withstand capability when stressed with fast transients whereas the opposite applies for homogenous electrodes. The expression *insulation system in sound condition* from Fig. 2.4 stands usually for a coaxial geometry without any surface defects. In the case of an optimal designed coaxial geometry [13], having an inner radius of r_i and an outer radius of r_a, the field efficiency

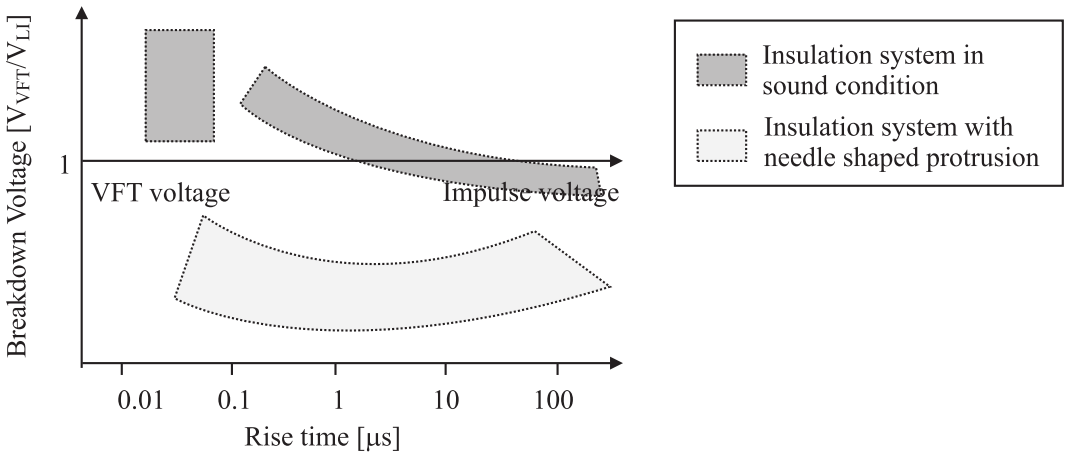

Figure 2.4.: Dielectric withstand level dependant on front risetime and electrode shape, adapted from [20]. Strong inhomogenous field arrangements stressed with VFT voltage show lower breakdown voltage, compared to low inhomogeneous field arrangements when both are normalized to their Lightning Impulse withstand level

factor is calculated as:

$$\eta = \frac{E_0}{E_{max}} = \frac{r_i \log\left(\frac{r_a}{r_i}\right)}{r_a - r_i} = \frac{1}{e-1} \tag{2.5}$$

$$\text{with} \quad \frac{r_a}{r_i} = e \tag{2.6}$$

The upper limit for the field efficiency factor in a coaxial geometry is therefore $\eta = 0.58$ and lies in the same range as circuit breaker contacts.
Except for [20], few data exist which verify a specific strength of electrodes with low inhomogeneous electric fields towards VFT-stress. In Fig. 2.5 the relative breakdown strength of electrodes with low inhomogenous fields with respect to VFT is shown [21]. It can be seen, that the weakness towards fast transient voltages is distinct for inhomogenous fields but not reversed for homogenous arrangements. According to this study, the mentioned coaxial geometry ($\eta = 0.58$) and circuit breaker contacts ($\eta = 0.4 \ldots 0.8$) would both be sensible with respect to VFT stress.

2.2. Evaluation of Breakdown Probabilities in SF_6

Due to the statistical nature of breakdown development in gases, no simple mathematical model that is able to predict the breakdown voltage of low inhomogeneous electrodes accurately has been developed thus far. Nevertheless, the contact system of a circuit

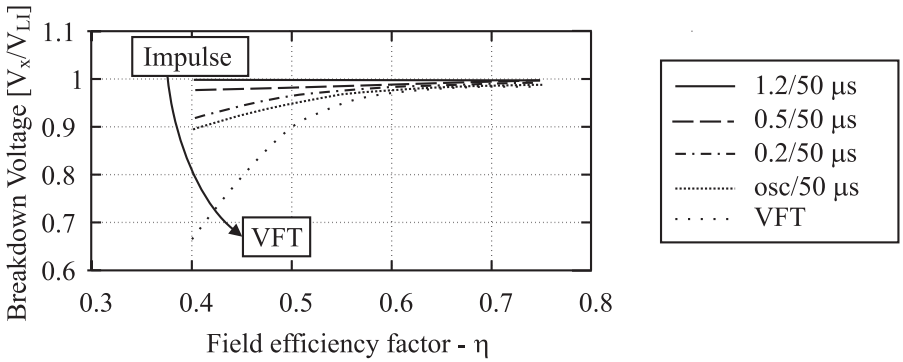

Figure 2.5.: Dielectric withstand level of impulse voltages with different frequency contenct compared to lightning impulse as function of field efficiency [21]

breaker has to be designed according to some criteria. Thus, experimental investigation and empirical description of the results is an accepted technique for providing the necessary information.

2.2.1. Measurement Procedures

To get a reliable and quantitative description of the breakdown behavior of an electrode arrangement through experiments, basically three different procedures can be applied:

Constant Voltage Method

The constant voltage method [22] or multiple level test [23] consists of the repetitive execution of measurements with the same parameters. In disruptive discharge tests a certain voltage V_i is applied n-times. This results in $k_i \leq n$ breakdowns. The number of different voltage levels is $i = 1 \ldots m$. Performing measurements with the constant voltage method starting with a voltage level V_1 with $k_1 = 0$ and ending with a voltage level V_m with $k_m = n$ results in dataset where the breakdown probability $p_i = p(v = V_i)$ for each voltage level can be estimated through

$$p_i = p(v = V_i) \approx p(V_{i-1} < v < V_{i+1}) = \frac{k_i}{n} \quad . \tag{2.7}$$

The resulting empirical distribution function is schematically depicted in Fig. 2.6a.). This method is applicable for impulse-, Direct Current (DC)- or Alternating Current (AC)-voltages. By applying impulse voltage stress, one measurement usually consists of one voltage application. Under DC or AC stress, a measurement is defined as application of the voltage for a defined time and amplitude.

Rising Voltage Method

The rising voltage method [22] or progressive stress test [23] is likewise applicable for any voltage shape. The experiment consists of repetitive measurements, whereas in each individual measurement the voltage is increased until a disruptive discharge occurs. If impulse voltage is used, the voltage increment is discrete and one measurement consists of several voltage applications. In the case of a rising voltage test with AC and DC one measurement consists of one voltage application with discrete or continuously rising voltage. In this test, the parameters are the initial voltage V_1, the increment ΔV or the rate of rise of voltage $\Delta V/\Delta t$, the number of individual tests n, which in this case is equal to the number of discharges $n = k$. The resulting dataset is only a series of voltage values V_{BD} and therefore only the cumulative probability $p_c = p(v > V_c)$ can be estimated (2.8).

$$p_c = p(v > V_c) \approx \frac{\sum_{t=1}^{n} [V_{BD} < V_c]}{n} \tag{2.8}$$

The resulting empirical cumulative distribution function is schematically depicted in Fig. 2.6b.).

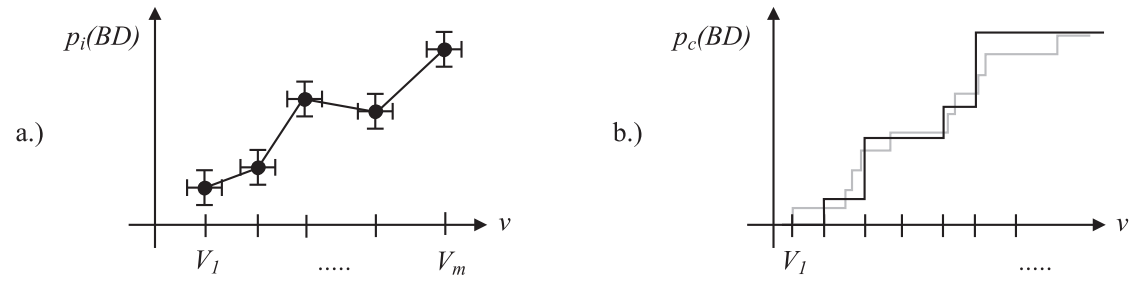

Figure 2.6.: Empirical breakdown probability distribution functions:
a.) Performance function as a result of constant voltage experiments
b.) Cumulative distribution function as a result of rising voltage experiments for continuously rising voltage (grey) or discrete rising voltage (black)

'Up and Down' Method

In contrast to the previously described methods, the up and down procedure [22], [23] does not result in a probability distribution for a certain voltage range, but rather in the voltage for a specific breakdown quantile. The most common procedure is the evaluation of the 50% quantile [24], which consists of a previously defined number of measurements $e = 1 \ldots n$, where the starting voltage V_1 is raised for each measurement by a voltage step ΔV until a breakdown occurs. After this event, the voltage level of any subsequent measurement will be determined by the outcome of the preceding. If measurement e

led to a breakdown, then the next voltage level is lowered $V_{e+1} = V_e - \Delta V$. If no breakdown occurred, the voltage level is raised $V_{e+1} = V_e + \Delta V$. For large values of n the 50% breakdown voltage V_{BD-50} can be estimated as the arithmetic mean of the voltages applied. Alternatively a test set out of the experimental series containing $m < n$ measurements has to be chosen. This is given the index $b = 1 \dots m$. Within this set, voltage classes can be defined, according to $V_b = V_1 + (b-1)\Delta V$ with a count of breakdowns within this group h_b. The V_{BD-50} can then be estimated with (2.9).

$$V_{BD-50} \approx V_1 + \Delta V \left(\frac{\sum_{b=1}^{m} b h_b}{m} - \frac{1}{2} \right) \tag{2.9}$$

2.2.2. Test for Independence

When executing repetitive measurements whose results are subject to a probabilistic distribution, the natural variation of the parameters and the course of the experiment shall not have a significant impact on its results. The individual measurements shall be statistically independent from each other. This requirement is usually controlled in two different ways:

Monitoring of the Course of Experiment

In the event that strong dependencies are observed during the execution of the experimental series it must be ceased and the reason for the dependance shall be investigated. Dependencies often manifest in a clustering of events.

Mathematical Test of Independence

In order to test for independence mathematically the hypothesis to verify is *The measurements are independent from each other.* For different procedures, different mathematical approaches to test this hypothesis exist. For constant voltage and rising voltage test, there is the iteration-test [25][1] and the modified iteration-test [22] respectively.

The iteration-test detects a clustering of events or periodical changes of events, which are both indicators for a statistical dependent measurement series. The test variable z is defined as follows:

$$z = \frac{r - \frac{2(n-k)k}{n}}{\frac{2(n-k)k}{n\sqrt{n}}} \qquad \begin{aligned} k &= \text{Number of Breakdowns} \\ r &= \text{Number of Iterations} \\ n &= \text{Number of Measurements} \end{aligned} \tag{2.10}$$

The hypothesis is rejected if $|z| > \lambda_q$, whereas λ_q is derived from the standard normal distribution as quantile of the order q and is given in Tab. 2.1. For investigation, the number

[1] Summary, originally published: [26] and [27]

of iterations i.e. the number of groups with consecutive same outcome r, the number of breakdowns k and the total number of measurements n, have to be known. At constant voltage experiments, the number of iterations r is the number of groups of breakdowns and holds, whereas in the modified iteration-test for rising voltage experiments, r is the number of groups of positive or negative sign when calculating the difference between the breakdown voltage and the arithmetic mean of the voltages of the whole experimental series.

Table 2.1.: Critical values to compare with independence tests [22]

Order q	Quantile λ_q
0.9	1.282
0.95	1.645
0.975	1.96
0.99	2.326
0.995	2.576
0.999	3.090

Another test for constant voltage experiments is the comparison of different control samples out of the total experimental series in order to detect long term trends during the execution of the experiment [22]. For this purpose two groups of consecutive measurements are extracted from the measurement series and their probability p_1 and p_2 are estimated according to (2.7). The hypothesis to be tested is *The two probabilities are identical,* $p_1 = p_2$. The test variable z is defined as follows:

$$z = \frac{p_1 - p_2}{\sqrt{\frac{p_1 n_1 + p_2 n_2}{n_1 + n_2} \left(\frac{n_1(1-p_1) + n_2(1-p_2)}{n_1 n_2} \right)}} \quad \begin{array}{l} n_1 = \text{Number of Measurements in Group 1} \\ n_2 = \text{Number of Measurements in Group 2} \end{array} \tag{2.11}$$

The hypothesis is also rejected if $|z| > \lambda_q$.

In order to test for deviations of the measurement series from stochastic behavior the phase-test [28], [29] can be applied. The hypothesis is in this case: *The difference of the results of consecutive measurements gives a random image.* For rising voltage method, the sign of the difference is used for the test and consequently the test can only be applied for this experimental method. The test is also known as the difference-sign-iteration-test. The number of consecutive changes of the sign, i.e. the number of consecutive changes of the phase is counted as h. Then the corresponding test variable z is defined as follows:

$$z = \frac{\left| h - \frac{2n-7}{3} \right|}{\sqrt{\frac{16n-29}{90}}} \quad \begin{array}{l} n = \text{Number of Measurements}, n > 30 \\ h = \text{Number of Phases} \end{array} \tag{2.12}$$

The hypothesis is rejected if $|z| > \lambda_q$

2.2.3. Ensuring Independence

When measuring the breakdown probability of SF_6 insulated electrodes there are two parameters which may induce statistical dependence.

1. Condition of the electrode
2. Condition of the insulating gas

Various advice exists, which intend to reduce statistical dependence of the experiment [30], [22], [12]. These advice can be divided in means taken during the preparation of the experiment and during the execution of the experiment.

Preparation of Experiment

During preparation of the experiment, the test vessel and the electrodes must be handled with maximum care. The deposition of particles, grease or dust must be avoided, since these surface layers are subjected to changes during the experiment and thus influence the experimental outcome.
The specimen should be cleaned after manufacturing either by ultrasonic or frigen bath or, if a certain irregularity of the surface is allowed or wanted by sand- or glass-blasting. After the cleaning process, the electrodes should only be handled with proper gloves or lint-less cloth.
The test vessel should be cleaned in the following order: using a hoover for large particles, pressurized air for dust and alcohol with lint-less clothes to remove traces of fat.
The evacuation before the filling of the test vessel with the insulating gas shall reach a pressure of maximal 50 Pa[2]. The SF_6 gas used, should have a high purity, and should be especially free of any particles and dissociation products of SF_6. The spare tanks of the gas handling equipment shall always remain pressurized with at least 0.1 MPa. After the filling procedure of the test vessel, the latter shall rest for at least two hours, although one night is recommended in order to settle inner turbulences and the remaining dust.

Execution of Experiment

In the experiment, electrodes are subjected to disruptive discharges, which leave traces on their surface. Therefore, the surface condition of the electrode cannot be kept constant during the experiment. The smoother the electrode's surface is at the beginning, the more severe is this impact. The effect of surface roughness increases considerably at higher pressures [14], [31], [5]. In order to mitigate this problem the energy impact

[2]equal to 0.5 mbar

onto the electrodes during breakdown is usually reduced as far as possible. This can be achieved by introducing a limiting resistor for energy dissipation into the test circuit. Another possibility is to use a triggered spark gap in parallel to the specimen under investigation, which discharges the source at the moment of breakdown in the test vessel [30].

The condition of the gas also changes during the course of the experiment. A breakdown highly distorts the ion density in the test vessel. At higher energy impacts even irreversible dissociation of the gas molecules can occur. Natural ionization and recombination processes will bring the gas back to equilibrium ion density after some time. Therefore, between measurements a sufficiently break has to be applied. Usually, a breaktime of 300 s is reported to be sufficient, irrespective of experimental parameters [21], [32], [16], [12], [33]. A time saving option is to apply a small electric field in between the measurements in order to sweep the excess ions [12]. This field should be big enough to induce a significant acceleration of the ions and still be small enough not to produce additional ionization at the contacts.

2.2.4. Evaluation of Results - Statistical Treatment of data

Constant and rising voltage method are addressing two different questions [22]. The constant voltage method evaluates the probabilities of two complementary events (breakdown or hold) to happen under the assumption of constant boundary conditions. The probability for a certain event bd to occur k-times in a series of n trials is expressed by the unknown bernoulli probability p:

$$p(bd = k) = \binom{n}{k} p^k (1-p)^{N-k} \quad . \tag{2.13}$$

An empirical estimation of the unknown probability p can be achieved by Eq. (2.7). The sum of all the probabilities from $bd = 0$ to $bd = k$ yields the binomial distribution:

$$P(bd \leq k) = \sum_{bd=0}^{k} \binom{n}{bd} p^{bd} (1-p)^{N-bd} \quad . \tag{2.14}$$

The rising voltage method evaluates the cumulative occurrence of a certain voltage level (evaluated by breakdowns). The stochastic event of breakdown in SF_6 is therefore often expressed by a normal distribution

$$P(V_c \leq v) = \frac{1}{\sigma\sqrt{2\pi}} \int_{-\infty}^{v} exp\left(-\frac{1}{2}\left(\frac{t-\mu}{\sigma}\right)^2\right) dt \tag{2.15}$$

The parameter μ is the mean of the corresponding density distribution. The parameter σ corresponds to the standard deviation, which is a measure for the skewness of the

distribution function. These parameters are estimated through adequate algorithms like the maximum-likelihood algorithm or a least-square fit. An empirical estimation of P can be achieved by Eq. (2.8).

If the parameter n of the bernoulli distribution is sufficiently big [25] it can be approximated by a normal distribution. In this case the parameter μ and σ are calculated by:

$$\mu = np \qquad \sigma = \sqrt{np(1-p)} \quad . \tag{2.16}$$

The result of the probability estimation underlies an uncertainty due to the limited number of input data. In order to express this uncertainty, confidence intervals are computed whose size are inversely proportional to the number of input data.

2.3. Very Fast Transient Voltages (VFT) in Gas Insulated Systems (GIS)

2.3.1. Source and Propagation

The normal frequency in the power grid is 50 Hz or 60 Hz. Nevertheless transient events within the power grid can occur which have a significantly higher frequency content. The fastest known event is called VFT and has been extensively investigated since its identification as a result of disconnector switching in GIS [8], [34], [35], [36]. The basic principle is depicted in Fig. 2.7. The figure illustrates a exemplarily disconnect switch interruption action, whereas the contacts reach clearance after a time frame of approximately 1 s. This time is called arcing time, although the arc is not continuously burning during this time. The switch disconnects a floating GIS-compartment therefore the action can be viewed as the interruption of a small capacitive current. The voltage in the floating GIS-compartment V_{GIS} tends to follow the source voltage V_0. Whenever there is a mismatch between V_{GIS} and V_0, a voltage drop across the disconnector results. If the contact separation is too small to withstand this voltage drop, formation of an arc leads to the equalization of the two potentials and the arc extinguishes, as soon as the equalization is complete. Because the source side voltage V_0 changes its polarity in much less time than the than the disconnector contacts are moving, this process results in a large number of re-ignitions during the opening or pre-strikes during the closing of the disconnect switch. This process has basically two effects on the insulations of the GIS. First, the steplike potential equalization results in traveling waves in the coaxial system with high amplitudes. Secondly, a trapped charge remains on the floating GIS busbar.

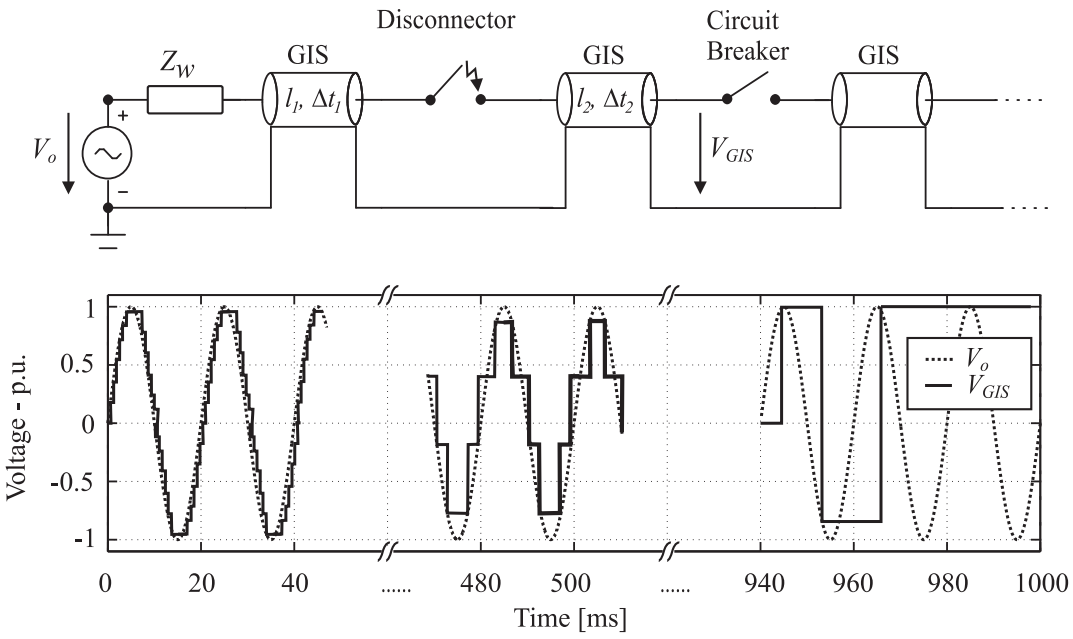

Figure 2.7.: Schematic drawing of disconnect switch induced potential development in GIS during an opening sequence. Until the disconnector reaches clearance a large amount of step-like potential equalizations happen

2.3.2. Rise-time and Frequency Content

The transition time or rise-time of the potential equalization is defined as the period of time between 10% and 90% of the maximum potential. It is determined by the breakdown time in the insulating gas. In an SF_6 insulated system it can be estimated through a rough approximation [37]:

$$t_a = \left(0.9 + 0.45\frac{1}{p\eta}\right) \quad \text{[ns]} \qquad \begin{array}{l} p = \text{gas pressure [MPa]} \\ \eta = \text{field efficiency factor} \end{array} \tag{2.17}$$

This approximation uses empirical data valid in the range of electrical fields of $80\,\text{kV/cm} < E_0 < 400\,\text{kV/cm}$. Eq. (2.17) is plotted in Fig. 2.8 for the technically relevant range of gas pressures $p = 0.1 \ldots 0.7\,\text{MPa}$. Notably the rise-time is shortest for homogeneous electrodes at high pressures and is in the range of nanoseconds. Comparing rise-time, propagation speed of the traveling wave and the size of contemporary GIS-equipment, the basic frequency f_0 of the resulting transient voltage through disconnector switching is determined by the length l between two major discontinuities [37]. In the example, Fig. 2.7 the length l would be the sum of the length of the GIS-compartment left and right of the disconnector $l = l_1 + l_2$ and result in the basic frequency f_0 of:

$$f_0 = \frac{v}{2(l_1 + l_2)} \qquad v = \text{propagation speed} \approx c_0 \tag{2.18}$$

For realistic geometries, eq. (2.18) results in a frequency range of a few MHz [37]. An overview of the transient frequency content is given in Tab. 2.2:

Table 2.2.: Origin of electrical transients and associated frequency ranges [38]

Origin	Frequency Range
Load rejection	0.1 Hz - 3 kHz
Line energization	50/60 Hz - 20 kHz
Transient recovery voltage	
Terminal faults	50/60 Hz - 20 kHz
Short line faults	50/60 Hz - 100 kHz
Multiple restrikes of circuit breaker	10 kHz - 1 MHz
Lightning surges, faults in substations	10 kHz - 3 MHz
Disconnector switching (single restrike)	
Faults in GIS	100 kHz - 50 MHz

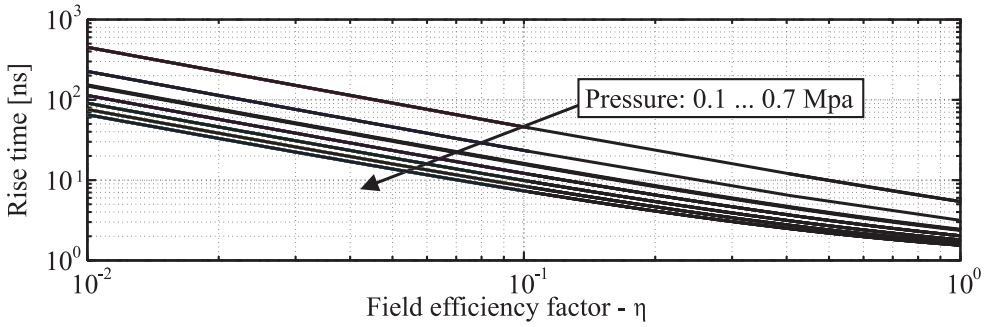

Figure 2.8.: Rise-times of SF_6 breakdown dependent on field enhancement and pressure. Low inhomogeneous field arrangements at high gas pressures show rise-times of few nanoseconds

2.3.3. VFT and Lightning Impulse Amplitudes

Assuming a lossless system, the basis for the description and analysis of traveling wave phenomena is the real value of the surge impedance $Z_w = |\underline{Z}_w|$ describing the ratio between voltage V and current I at a certain point on a waveguide.

$$Z_w = \frac{V}{I} \tag{2.19}$$

When a certain impulse voltage on a waveguide Z_{w1} encounters a discontinuity Z_{w2}, the respective wave is reflected and transmitted according to the reflection Γ and the

transmission T factor which are defined by the respective ratio of surge impedance:

$$\Gamma = \frac{Z_{w2} - Z_{w1}}{Z_{w2} + Z_{w1}} \quad , \tag{2.20}$$

$$T = 1 + \Gamma \quad . \tag{2.21}$$

According to (2.20) the reflection factor Γ can only be in the range of -1...1. Consequently, a wave with the amplitude of 1 per unit (pu) (e.g. V_{in} in Fig. 2.9a.)), reflected with the maximum reflection factor can only achieve 2 pu. In the case of trapped charge on a subsequent waveguide, (c.f. Fig. 2.9d.)) the voltage across an open contact V_{gap} can exceed this value.
Through theoretic consideration, the value of trapped charge is not limited. For example in the case of multiple re-strikes during switching of large capacitive currents the remaining voltage can reach values of several pu [2]. In real application, the value seldom exceeds 1 pu. Measured values related to disconnector switching are in the range of 0.1...0.3 p.u. [8].

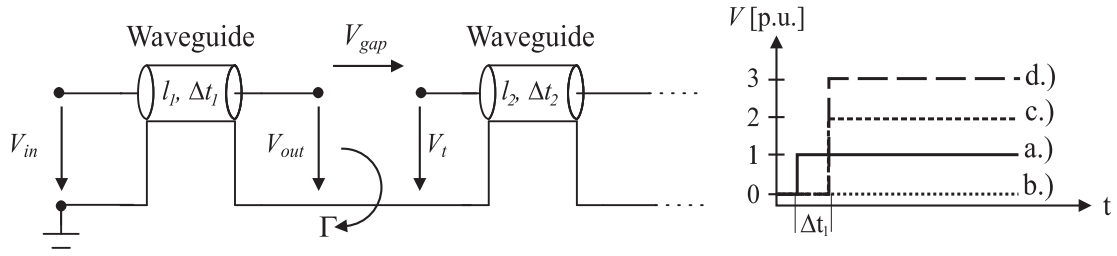

Figure 2.9.: Basic pulse propagation and resulting waveforms (pu):
a.) Input voltage form V_{in}
b.) Output voltage form $V_{out} = V_{gap}$ for short circuit $\Gamma = -1$ and no trapped charge $V_t = 0$
c.) Output voltage form $V_{out} = V_{gap}$ for open circuit $\Gamma = 1$ and no trapped charge $V_t = 0$
d.) Voltage across gap V_{gap} for open circuit $\Gamma = 1$ and trapped charge $V_t = -1$

Usually the insulation coordination of GIS has a rather high security margin in terms of pu stress, since they are tested to withstand lightning impulse voltages. In Fig. 2.10 the required lightning impulse withstand levels are plotted versus the maximum rated phase to earth voltage [3]. Based on the present trend toward higher rated voltages, the gap between service voltage and lightning impulse voltage becomes smaller and an overvoltage of 3 pu caused by VFT can exceed the lightning impulse voltage level for which the equipment is tested.

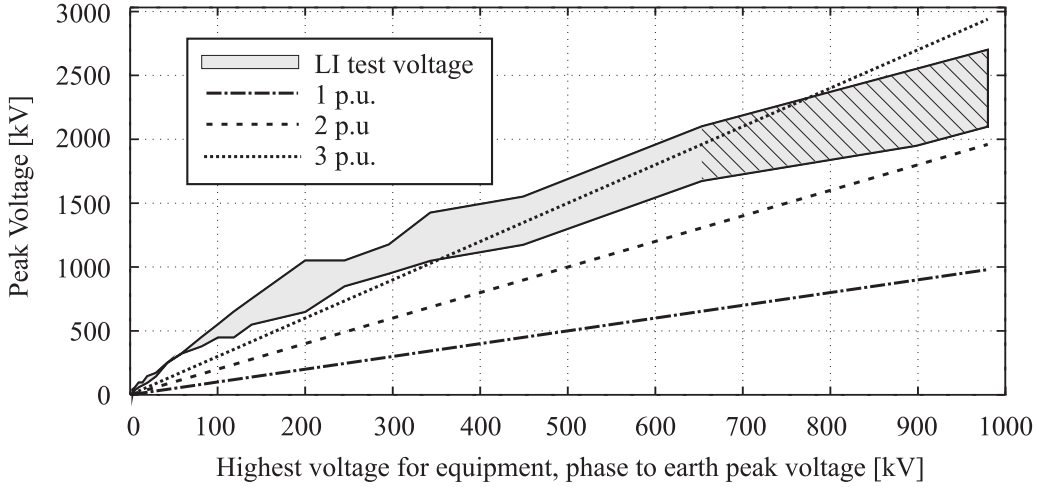

Figure 2.10.: Comparison of Lightning Impulse test voltages and per unit overvoltages as a function of highest phase to earth peak voltage [3] (Values above 653 kV are preliminary (corresponding to $U_{m-rms} = 800\,\mathrm{kV}$))

3. Breakdown Probabilities of Circuit Breaker Contacts

The following chapter describes the assembly and the results of an experimental setup to evaluate the implicit distortion of dielectric coordination. The results of the experiments are breakdown probability curves of different contact systems, representative for circuit breaker contacts and are used to show interactions between several contacts with respect to their probability distribution.

The goal of the investigation is to describe the breakdown behavior of an electrode geometry in the most accurate way possible. Since the 'Up and Down'-method results in only a certain quantile of the breakdown probability it is not an adequate technique. Furthermore, the rising voltage method leads only to the cumulative distribution function and in the case of a not monotonic rising empirical distribution function, this cannot be detected. Therefore the preferred method is the constant voltage test. Although very time consuming it gives the most accurate results and has one additional advantage over the rising voltage method: Statistical dependencies are often very easy to detect within an experimental series, even without using mathematical tools.

3.1. Specimen

Five different electrodes were used to investigate the breakdown behavior (c.f. Fig. 3.1). A plane electrode was used for preliminary experiments and four contacts whose geometry was similar in rough size and curvature to the ones used in high voltage circuit breakers. Since only the breakdown behavior was investigated several simplifications could be made without loosing accuracy:

- The shape of the electrode tips is spherical, which allows simple electrostatic field calculation and comparison of field values used for dielectric coordination. It is an ideal geometry which reveals the basic breakdown behavior but is not directly applicable to realistic circuit breaker contacts.

- The contacts have no functionality with respect to current carrying capability. Consequently they are all made out of the same material and do not support a nozzle.

- In order to get an undisturbed result of the dielectric coordination in one specific situation the influence of the movement of the contacts was neglected. Therefore, the electrode mount system was a full static device.

The electrodes were made out of stainless steel (NiCr) and the surface was sandblasted (80 μm grain) in order to minimize the relative change in surface condition during the experiments. This treatment resulted in a mean surface roughness of $R_a = 1.85\mu m$ and a maximum surface roughness of $R_z = 15.22\mu m$ [1]. In combination with the electrode mount system the contact distance of all four contacts could be individually adjusted[2].

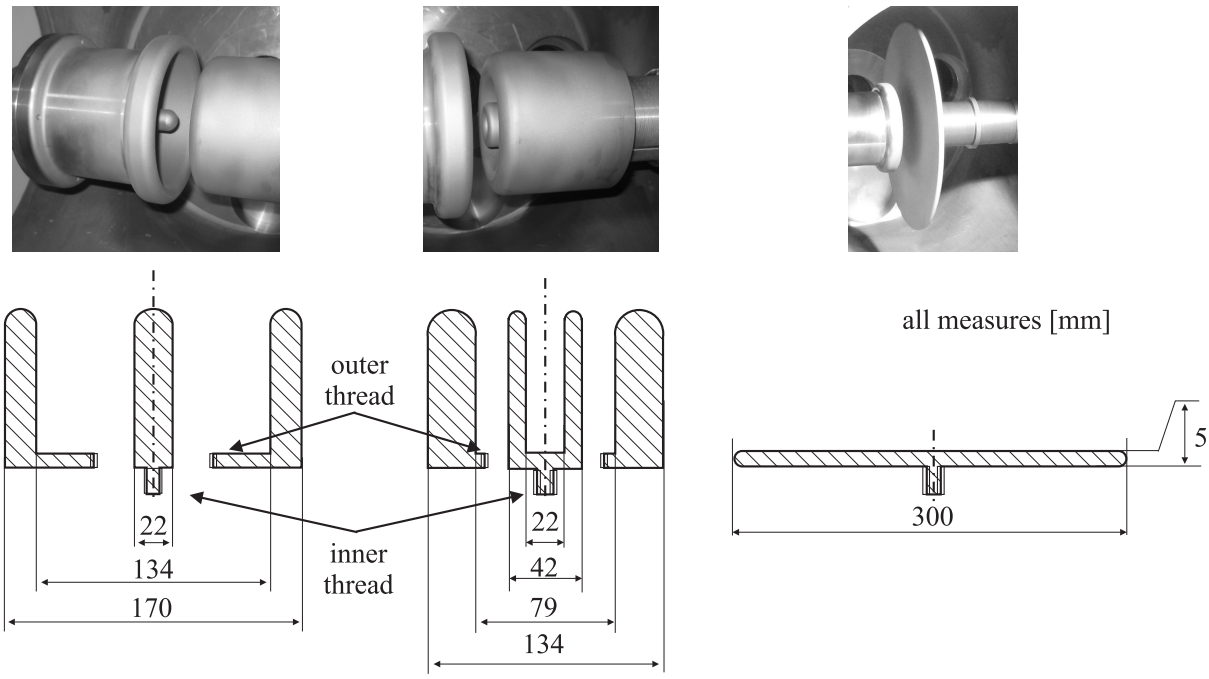

Figure 3.1.: Electrodes under investigation from left to right: Fixed main contact, fixed arcing contact, moving main contact, moving arcing contact, plane electrode

The electric field of an electrode arrangement using all four contacts is depicted in Fig. 3.2. The color-map shows the absolute value of the electric field vector [V/m] with a potential difference of 1 V between the electrodes. In this arrangement the contacts have the same contact separation of $s = 10\,\text{mm}$ and a contact distance of $d = 14.53\,\text{mm}$ and $d = 17.13\,\text{mm}$ between the arcing contacts and the main contacts respectively[3]. The electric field along the shortest distance between the electrodes (*arc length* in Fig. 3.2) showed a favorable dielectric coordination on the fixed contact side but at the same time a poor coordination on the moving contact.

At a contact separation of 10 mm (Fig. 3.2), there was an implicit field enhancement on the fixed contact side between the arcing contact and the main contact due to the

[1] Measured according to ISO 4288:1996E
[2] The terminology, contact travel, contact separation and contact distance is clarified in Appendix B.
[3] Details of the calculations can be found in Appendix B and C

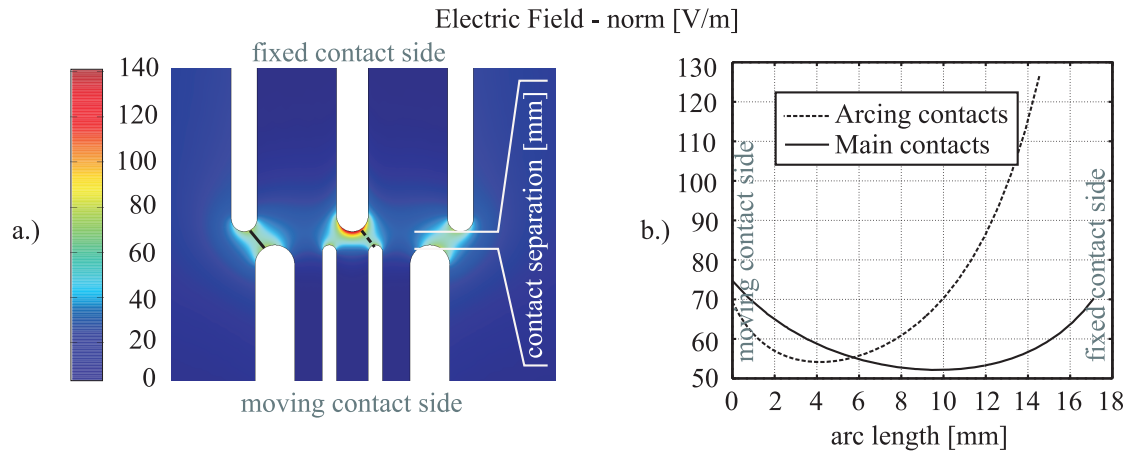

Figure 3.2.: a.) Electric field distribution in a schematic circuit breaker contact system b.) Electric field along shortest distance between the electrodes. Potential difference: 1 V at 10 mm contact separation

difference in shape of the two contacts. The ratio of electric fields depended on the contact separation as depicted in Fig. 3.3. At a certain contact separation the electric field of the arcing contact at the fixed contact side was lower than the field of the main contact of the moving side. In the present example this happened at a relatively wide gap.

Furthermore, the present arrangement revealed that the maximum electric field at three of four contacts was almost identical over a wide range of contact travel. The electric field at the fixed arcing contact was the only contact exceeding the others.

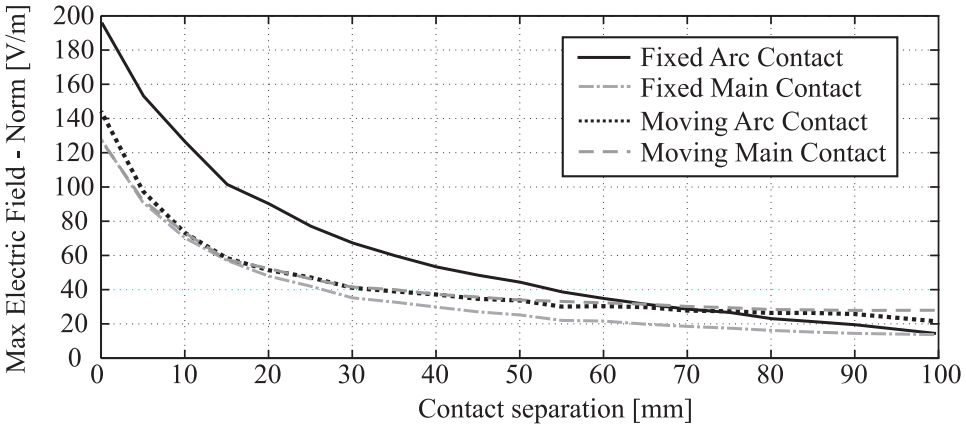

Figure 3.3.: Maximum absolute value of electric field on different contacts as a function of contact travel for the contact system of Fig. 3.2. The field on the fixed arcing contact is enhanced whereas all other fields show comparable values

3.2. Experimental Setup

The application of the constant voltage method implies the execution of a large number of measurements. Therefore, a fully automated test stand was developed and constructed. The experimental setup is depicted in Fig. 3.4 and can be divided into two parts: The air insulated and the SF_6 insulated part.

Air Insulated Part

Either an impulse voltage source or an AC voltage source could be connected selectively to the experimental setup. The switch between the two sources was realized through a motor actuated steel cable. The connection between impulse generator and capacitive voltage divider was either direct or through a spark gap (Fig. 3.4 and Fig. 3.5). The last section of the air insulated part was the load side, which was a limiting resistor as depicted in Fig. 3.4.

SF_6 Insulated Part

The connection between the air and SF_6 insulated parts was made by an SF_6 filled bushing with composite insulator. The following gas compartments were standard GIS components, whereas each compartment was sealed individually. In the center of the test device, the test vessel and the electrodes under investigation were located. In order to ensure maximum flexibility of the setup, on both sides of the test vessel an earth switch and a disconnect switch was installed. An overview of ratings is given in Tab. 3.1.

Table 3.1.: Ratings of used gas insulated equipment

	Bushing	GIS Parts
Max. AC-withstand voltage	460 kV	740 kV
Lightning impulse withstand voltage	1050 kV	1550 kV
Pressure, absolute	0.6 MPa	0.6 MPa
Manufacturer, Type	Trench, Model DFS245	ABB, ELK-3

3.2.1. Source

The impulse voltage source was a Marx-Generator, Type E of Haefely Test AG having ten stages with capacitance of 0.6 μF and a charging voltage of 100 kV (DC) each, resulting in a maximum total energy of 30 kJ. The AC source was a voltage transformer, Type TEO100/10 of Messwandler Bau GmbH. It had a maximum output voltage of 100 kV (rms) at a power rating of 5 kVA.

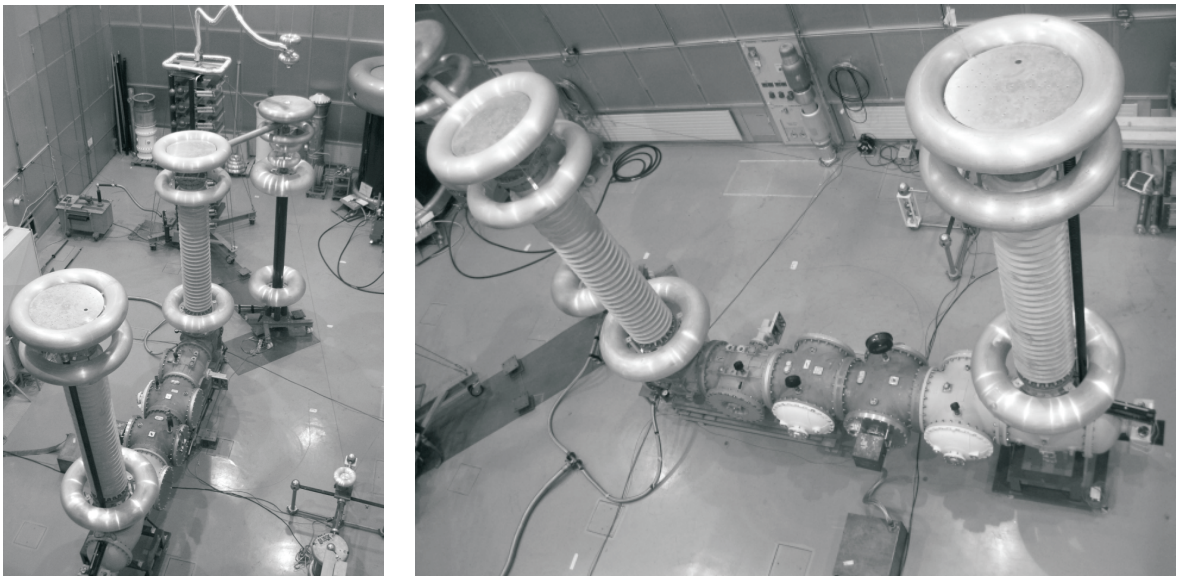

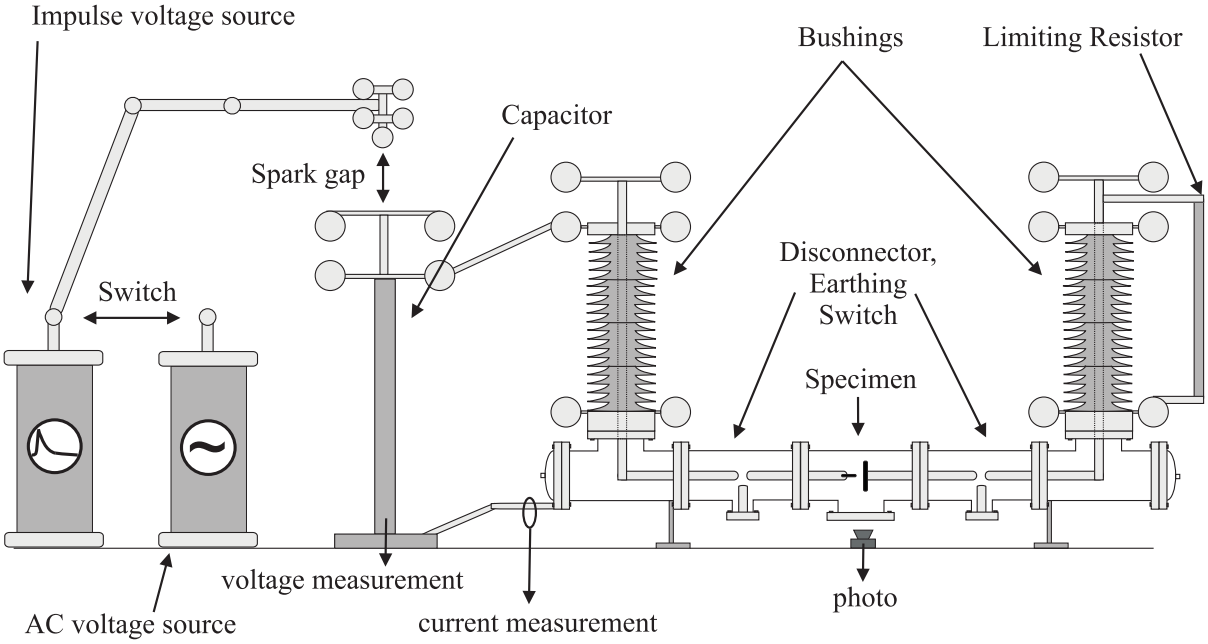

Figure 3.4.: Photos and schematic drawing of the experimental setup for breakdown tests

3.2.2. Voltage Shapes

By using the high voltage transformer, a testing of the breakdown behavior for AC-Stress would be possible, but in the present case the AC-source was only used to sweep excess ions between impulse voltage application (cf. section 2.2.3).

The Marx generator is capable of producing standard [23] lightning and switching impulse voltages. A speciality of the present experimental setup was the ability to produce a steplike DC-voltage using a Marx-generator, an asymmetric spark gap (Fig. 3.5) and

a capacitive voltage divider. For this application the Marx generator had to produce a hybrid impulse form, having front time according to lightning impulse and a time to half value according to switching impulse. With the application of a positive impulse voltage (V_{Marx} in Fig. 3.5) and the correct gap distance chosen, a breakdown occured at the peak of the impulse voltage and charged the attached capacitive voltage divider to the peak voltage, $V_{capacitor} = V_{Marx}$. Since the decay time of switching impulse application was rather long, the peak time of the impulse voltage was much longer than it took to charge the capacitor. Therefore, the arc in the spark gap extinguished. Due to the polarity effect of streamer breakdown in strong inhomogeneous electrode arrangements in air [13], no backflash occured once the Marx generator was fully discharged and the capacitor kept its voltage, acting as a DC voltage source. The DC voltage decayed due to corona losses and resistive losses in the capacitor.

The geometry of the spark gap was a compromise between minimum η to support the polarity effect and maximum η to avoid corona losses. In the experimental setup a 150 mm diameter sphere and a 1200 mm diameter plane electrode showed acceptable behavior between approximately 250 kV and 900 kV, with spark gaps between 500 mm to 2000 mm. For lower voltages, η was not sufficiently small and a smaller sphere had to be chosen.

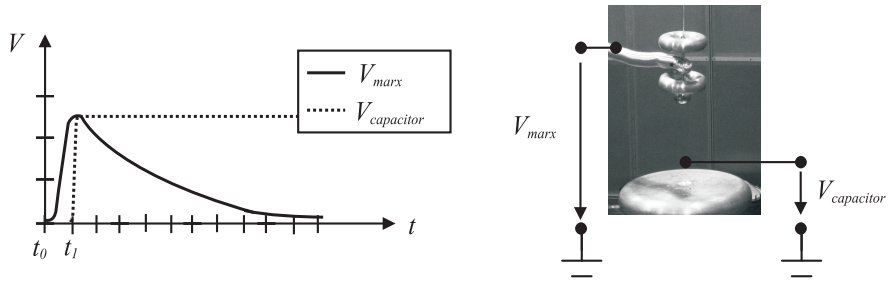

Figure 3.5.: Schematic drawing of quasi-DC waveform produced by asymmetric spark gap

3.2.3. Load

The experimental setup offers the flexibility to attach different loads. An opened disconnector after the specimen resulted in a very small capacitive load (floating electrode) while a closed disconnector and removed resistor resulted in a slightly bigger capacitive load. A closed earth switch resulted in a short circuit. The load side bushing allowed the connection of any further lumped elements.

For most of the experiments a limiting resistor was used (Fig. 3.4). The resistor is a semiconductive PVC-pipe with a resistance of approximately 2.2 MΩ. Through this high

resistive path an effective current limitation could be reached and the duration of current flow across the electrodes was very limited. Thus the damage of the electrode surface during experiments was decreased.

3.2.4. Test Vessel

The test vessel was a standard, cross-shaped GIS-element. It was equipped with a Class: 0.1 Manometer (Wika) having an analogue scale resolution of 0.02 bar. The test vessel had four openings. On two of them, barrier insulators were mounted and their center was used for the installation of the electrode mount system. The remaining openings were closed with plane 60 mm thick aluminium caps. One of these caps was equipped with two 160 mm diameter PMMA windows for optical survey of the electrodes. The test vessel and the electrode mount system can be seen in Fig. 3.6. Each electrode carrier of the electrode mount system consisted of two thread-connected pipes (1 mm/turn). Electrodes could be attached either on the outer or the inner thread of the pipe according to Fig. 3.6d.) and Fig. 3.1. Therefore, the contact distance between opposite contacts as well as the relative location of electrode tips on the same contact side could be adjusted.

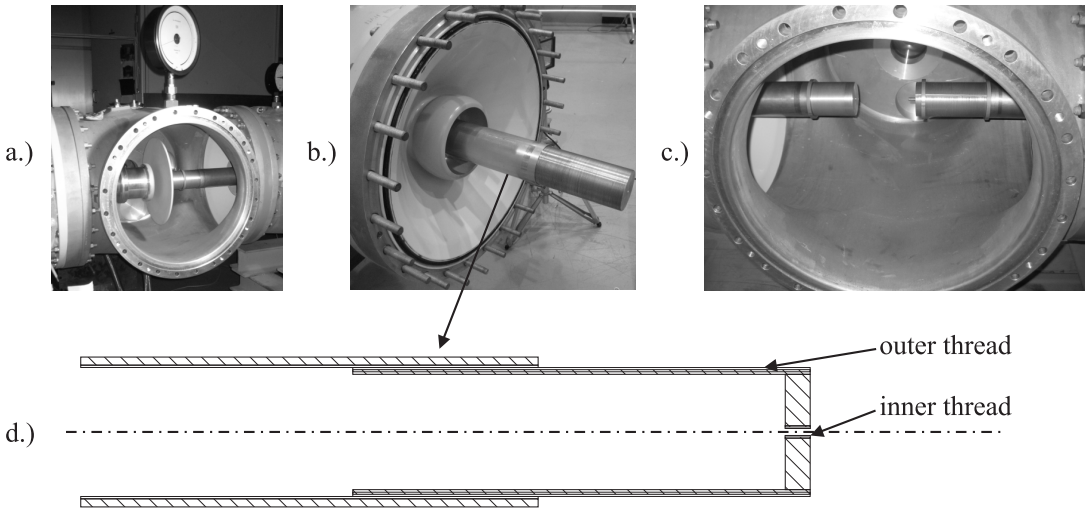

Figure 3.6.: a.) Test vessel b.) electrode mount on barrier insulator c.) electrode mount system d.) schematic drawing of electrode mount with inner and outer thread

3.2.5. Voltage and Current Measurement

The measurement of the voltage was conducted by a series-damped capacitive divider (C_1 =1431 pF, R_1 = 80 Ω, C_2 = 2.88 μF). The divider ratio of 1:2013.6 was relatively low for high voltage application. This was advantageous since the signal to noise ratio

on the transmitting cable is very low. However, it is disadvantageous[4] for the recording instrument. Therefore, a voltage probe (LeCroy, PPE 4 kV) was used to reduce the output signal after the transmission. The probe was an RC-divider with $R_{p1} = 50\,\mathrm{M\Omega}$ and $R_{p2} = 1\,\mathrm{M\Omega}$, which when added to the input impedance of the recording instrument resulted in a divider ratio of 1:100. This combination could have distorted the measurement of very high frequency components due to traveling waves in the measurement cable. But under the assumption of a very high voltage resistance, it contributed to a low cutoff frequency f_c of the voltage-divider, hence making it suitable for the measurement of slow decaying DC voltages:

$$f_c = \frac{1}{2\pi\,\mathrm{C}_2\left(R_{p1} + \frac{R_{p2}}{2}\right)} = 1.1\ \mathrm{mHz} \quad . \tag{3.1}$$

The current measurement was performed on the low voltage side at the enclosure to ground connection as indicated in Fig. 3.4. The device used is a Pearson current monitor (Model 110 A) with a 3 dB cutoff frequency of 1 Hz and 20 MHz respectively. Maximum peak current was 10 kA with an output ratio of 0.1 V/A. This ratio resulted in rather high signals, which were damped by using Micronde 50 Ω attenuators. Depending on the experiment, different attenuation factors were applied, but usually an attenuation of 50 dB was sufficient.

3.2.6. Arc Root Point Detection

The survey of the specimen during breakdown tests is important for two reasons: Firstly, the damage of the electrode during the experiments increases its surface roughness. This process results in the accumulation of arc root points at a certain location on the electrode and consequently in a statistical dependent measurement series. A chronological survey of the arc root points would reveal this. Secondly, the investigation of multi-contact systems requires a distinction between the arcing location on inner and outer contacts. The most convenient way to survey the specimen is through optical monitoring. However, in order to reach the required accuracy a 3-dimensional survey is required. This 3-dimensional survey is explained in the following sections and divided into the parts 'Image Acquisition', 'Detection and Reconstruction' and 'Calibration of the System'.

Image Acquisition

The optical information was assessed through the usage of a digital single lens reflex camera (Nikon D50). The usage of a simple photo camera avoided synchronizing problems with breakdown occurrence, since the shutter of the camera can remain opened during the measurement. The resulting picture was nevertheless of good quality because the arc is not moving on the electrode surface, based on the short time of energy input. Because the

[4]The terminology *disadvantageous* is a synonym for *lethal* in this context

focus of the lens can be mechanically locked, taking pictures with a single reflex camera was highly reproducible. In order to get a high quality image, the camera was set to maximum ISO number and maximum aperture. Although the aperture setting darkened the picture substantially, the resulting photo of the arc was often still too bright. A very simple, effective and adaptive solution to this problem, was the usage of two standard, linear polarization filters in series. The angular difference between the two polarization axes resulted in a light attenuation which could be precisely adjusted.

Detection and Reconstruction of 3-Dimensional Information

A normal photograph provides only 2-dimensional information content of a certain object. To reconstruct a 3-dimensional object based on a 2-dimensional photo, additional information has to be captured in the picture. This was achieved by the insertion of two mirrors in the test vessel (c.f. Fig. 3.7).

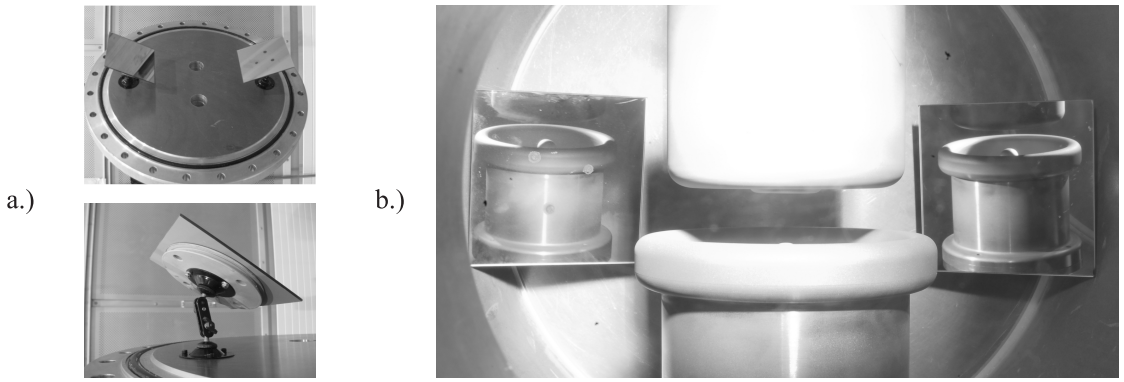

Figure 3.7.: 3-dimensional information on a 2-dimensional photo to reconstruct arc root point location: a.) Mirror mount in test vessel b.) Resulting picture

The picture of an object in the mirror was interpreted as the flipped photo taken by a virtual camera behind the respective mirror (c.f. Fig. 3.8). The position and viewing direction of the virtual cameras were determined by the position and pitch of the mirrors.

In order to allow a reconstruction of the 3-dimensional object, three parameters for each camera had to be known. The position $\vec{c}$ of the camera, the viewing direction $\vec{f}$ and the focal distance $\left|\vec{f}\right|$ (c.f. Fig. 3.9). Under the assumption of an undistorted beam-projection through the lens of the camera, the received picture was re-projected through a point-light source at position $\vec{c}$ and a plane transparency with distance $\left|\vec{f}\right|$ to $\vec{c}$ and a normal vector of the plane having the same direction as $\vec{f}$.
Any pixel $\vec{r}$ of the plane transparency could then be projected according

$$\vec{P} = \vec{c} + m(\vec{f} - \vec{r}) \qquad m \in \mathbb{R} \quad . \tag{3.2}$$

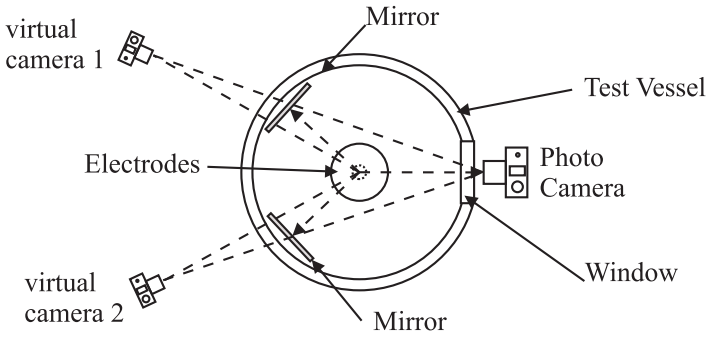

Figure 3.8.: Schematic explanation of picture projection by mirrors in test vessel

This projection $\vec{P}$ is illustrated for the three edges of a triangular object in Fig. 3.9. The procedure to completely reconstruct a 3-dimensional object can be divided into the following steps:

1. Divide picture into three parts. Direct image and two images in the mirror.
2. Extract arc contour and root point of contour by image processing for each picture.
3. Project pixel of root point according to Fig. 3.9 and Eq. (3.2) using all three cameras.
4. Calculate intersection of the three different projections.

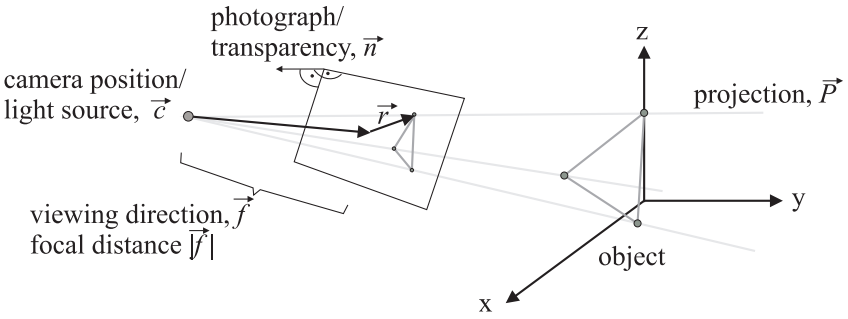

Figure 3.9.: Schematic explanation of re-projection of image to create 3D-object

Calibration of the System

As described previously, the reconstruction requires three parameters for each camera which must be known: The position $\vec{c}$, the viewing direction $\vec{f}$ and the focal distance

$\left|\vec{f}\right|$. These parameters were extracted through a calibration of the system. Calibration consisted of the reconstruction of an object with well known geometry. In the present case this was a pyramid with laser pointer illuminated edges (Fig. 3.10). Using this pyramid, a three dimensional space could be defined (cartesian coordinates according to Fig. 3.10 and Fig. 3.9) with the pyramid in the center of the coordinate system. By choosing realistic initial values, position, viewing direction and focal distance was iteratively adjusted for all three cameras until the projected image showed minimal difference to the real object.

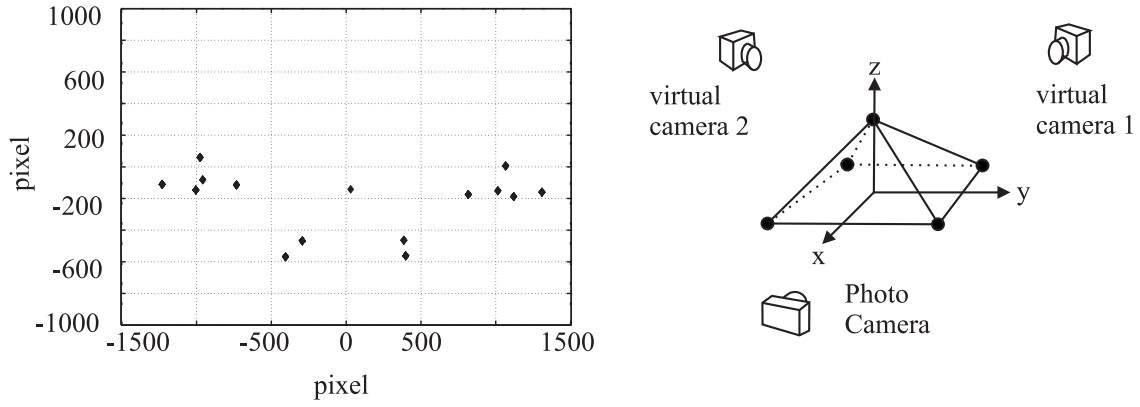

Figure 3.10.: Definition of camera position and viewing direction by reconstruction of a known object. The scatter plot in the left picture shows the photographed edges of the object in the right picture. The axes indicate the resolution of the photo camera (3008x2000 pixels)

Calibrating the system in this manner is very convenient since the physical setup does not have to be adjusted itself. The camera and mirrors only have to be arranged in a way, that the desired object is visible in the photo on all three locations. The calibration and reconstruction algorithm was developed and implemented in Matlab R2007b. The image processing toolbox of Matlab offers a large amount of useful photo editing commands, like filtering and contour extraction.

3.2.7. Control, Recording and Connections

The experimental setup was controlled by a computer. The cycle of an experimental series was implemented in a Matlab R2007b script with corresponding graphical user interface (c.f. Fig. 3.11).

The PC had three control points: The control box of the Marx-Generator, the digital storage oscilloscope (LeCroy, Wavepro7000, 1 GHz, 10 GS/s) which recorded the measured data, and the photo camera (remote control). The PC collected the recorded data via ethernet (oscilloscope) or fiber-optic USB-connection (photo camera). The wiring of the complete setup can be seen in Fig. 3.12.

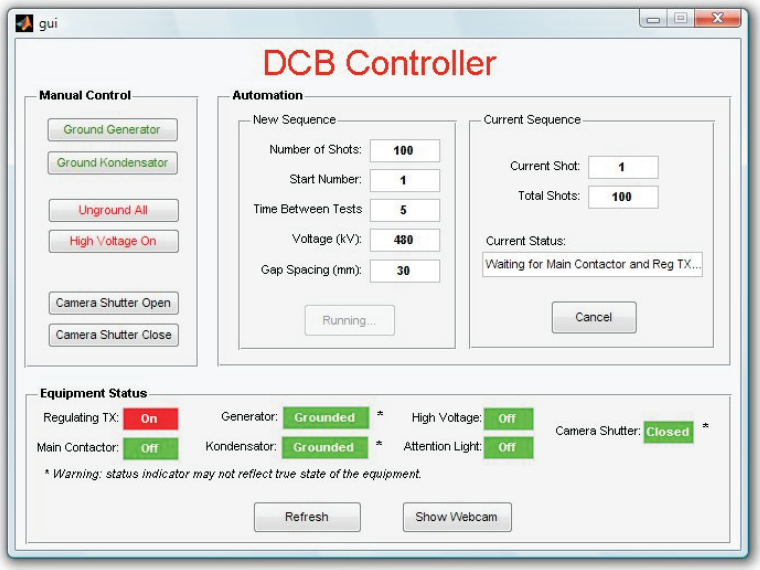

Figure 3.11.: Grafical user interface to control automatic experimental setup

Breakdown experiments in SF_6 are characterized by very steep and high current pulses. Therefore, they are most critical with regard to electromagnetic compatibility (EMC). The following guidelines were considered:

- The Test circuit must be characterized completely. Not only do the high voltage connections have to be carried out as low resistive, low inductive elements but also the low voltage connections, i.e. earth connection.
- Any electrical connection carrying signal voltages should either be an optic link or properly shielded.
- Only EMC-robust electronic equipment shall be used. In particular the usage of USB-connection for the photo camera and the control box of the Marx generator has to be reviewed critically.

3.3. Evaluation of Experimental Setup

3.3.1. Voltage and Current Shapes

The experimental setup allowed the execution of experiments with various voltage shapes. A selection is given in the following section to show the behavior of the system and its impact on the specimen. Fig. 3.13 shows voltage and current measurements received while experimenting with open spark gap and without a limiting resistor. The charging voltage of the Marx Generator was set to 390 kV. Due to the arc resistance in the spark

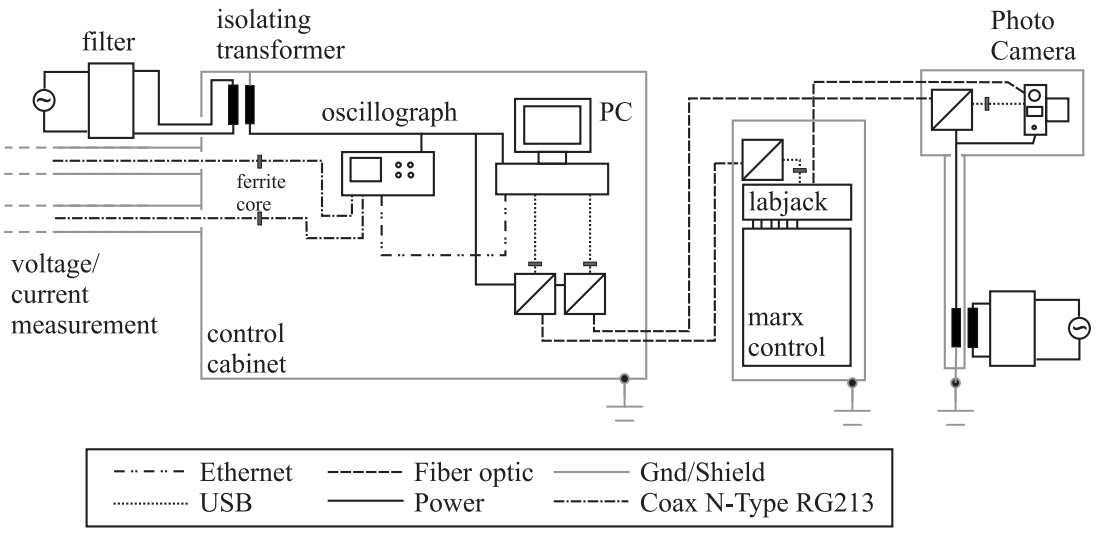

Figure 3.12.: Wiring and shielding scheme of the experimental setup for controlling and recording of measurements

gap, the resulting peak voltage was lower with a value of 382 kV. The initial peak was followed by a drop to 370 kV of approximately 10 ms duration. After 990 ms the voltage was approximately 360 kV. The initial drop was likely to be caused by space charge induced current flow after the extinction of the switching arc. After that drop, the decay due to corona loss was less than 5% per second.

Fig. 3.13 shows as well a measured curve with charging voltage of 390 kV and a very late breakdown happening at about 252 ms. Due to the breakdown onto a floating electrode, the circuit was not discharged, but the voltage level was lowered due to capacitive charge transfer. The observed current peak was rather small and of very short duration. In fact, it was only covered by one data-point of the curve form because the resolution of the oscilloscope drops to 1 μs/pt when recording a full second. Its value was not reliable, since the current flow did not follow a galvanically connected path, but was only the result of displacement current. The same applies for the first current peak, which shows the instant in time, when the spark gap breakdown occurred. In these experiments the experimental setup was upgraded with an automatic earthing mechanism which discharged the floating electrode after each shot.

When adding the limiting resistor on the load side a quasi-DC voltage as in Fig. 3.14 resulted. In this case the charging voltage was 400 kV and a measured peak value of 361 kV. The difference between peak and charging value was higher than in the previous example, indicating a different, though not perfect setting of the spark gap distance. In this case the initial current pulse due to the spark gap breakdown was not captured, but two consecutive breakdowns in the test vessel were observed. The first breakdown happened at approximately 4 μs while the spark gap arc was not yet extinguished. Therefore, no

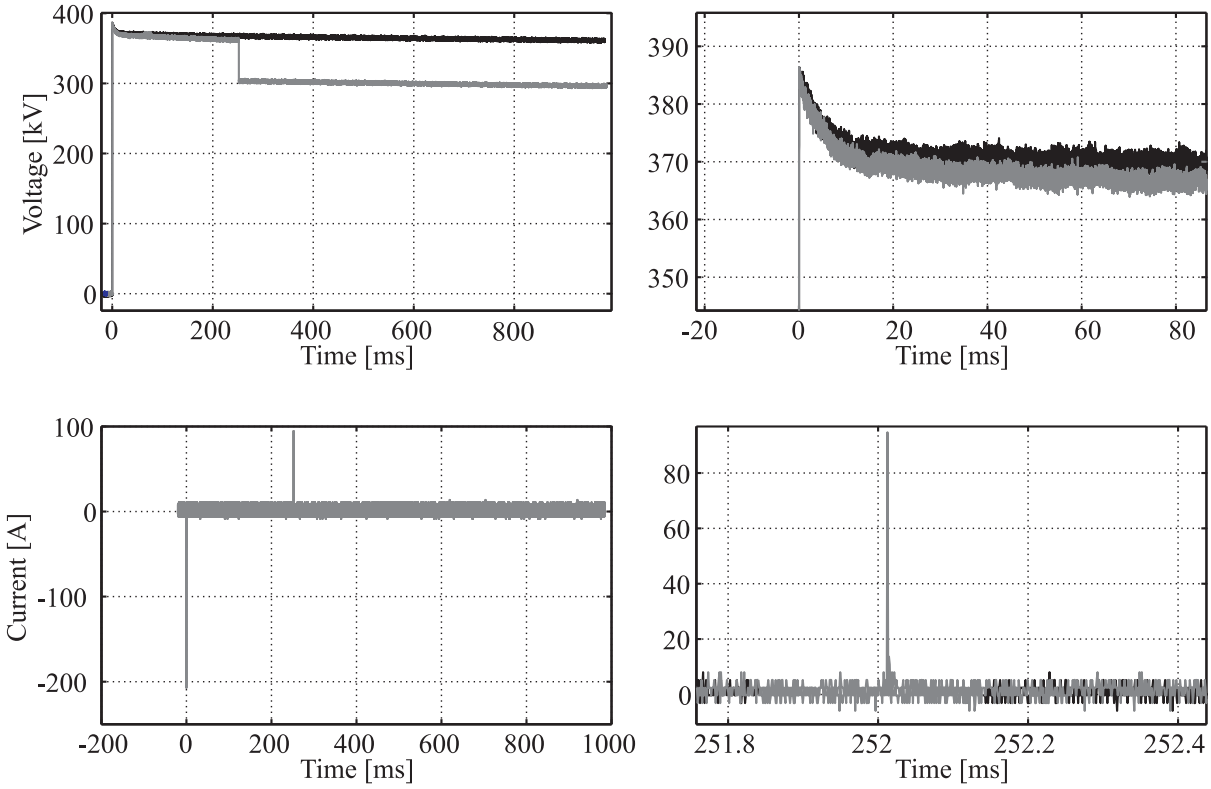

Figure 3.13.: Measured quasi-DC voltage form and corresponding current form with discharge to floating electrode

voltage drop according to this breakdown is visible. The resistor provided a very effective current limitation since it actually stopped the discharge of the source through the SF_6 insulated part of the setup. Still the peak amplitude of the current in this case was much higher (1.243 kA), compared to Fig. 3.13. After about 2.5 ms the stray capacitance of the load side GIS-parts was discharged via the limiting resistor and a consecutive breakdown with a much smaller amplitude of 335 A takes place.

When the spark gap and the earthing switch on the load side were closed, the voltage shape showed the hybrid voltage form with approximately 1.2 μs front-time and 2500 μs time to half value as depicted in Fig. 3.15. The Marx generator was charged to 400 kV and the measured peak voltage showed a value of 413 kV. In this case, the damping by the spark gap resistance in the previous measurements was absent and resulted in a voltage form with a slight overshoot due to the stray inductance of the experimental setup. In this case a breakdown leads to a total discharge of the Marx generator and therefore to a current pulse with 2.306 kA peak value and a long duration in the range of 30 μs.

In order to evaluate the maximum current amplitude in the case of resistive current limitation, experiments with high voltage stress amplitude were executed. Fig. 3.16 shows a lightning impulse shaped voltage wave with 913 kV peak amplitude at charging voltage of 900 kV. The current peak reached almost 3 kA but was of a short duration of

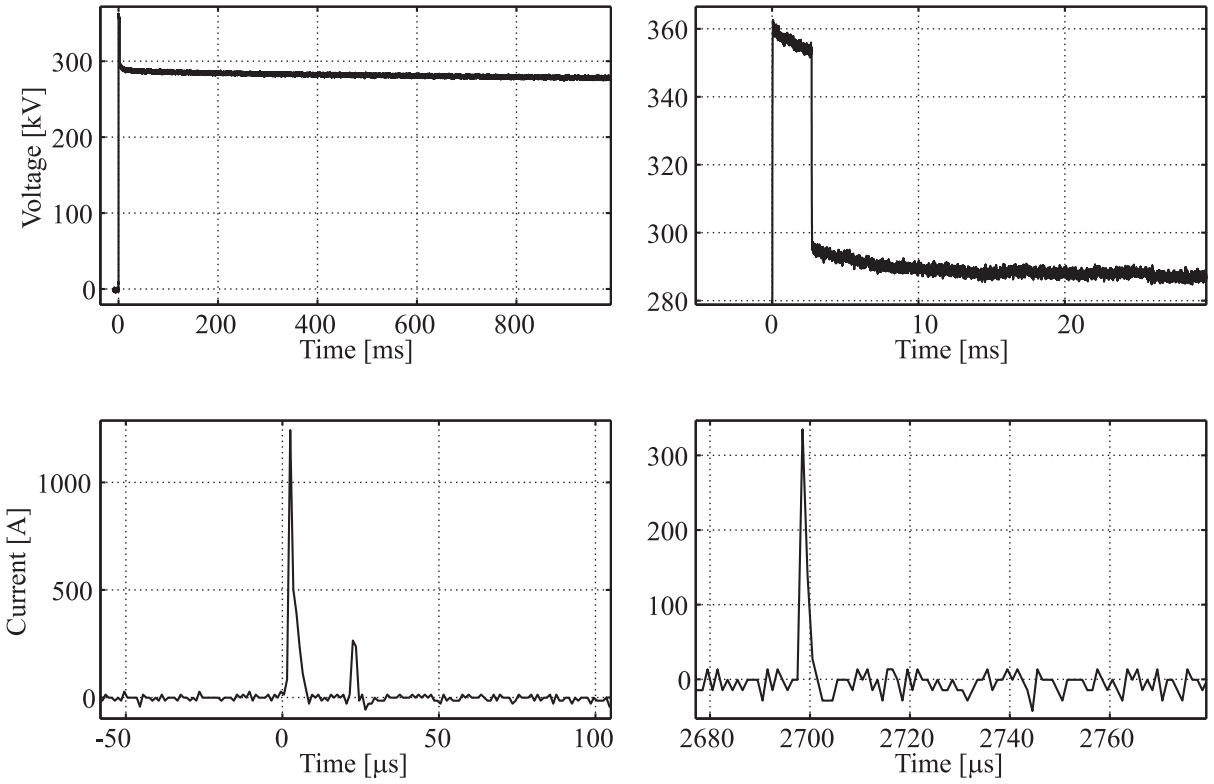

Figure 3.14.: Measured quasi-DC voltage form and corresponding current form with discharge to limiting resistor

approximately 1 μs. Both, voltage and current measurement showed that the discharge across the specimen in the test vessel was stopped by the voltage drop across the limiting resistor.

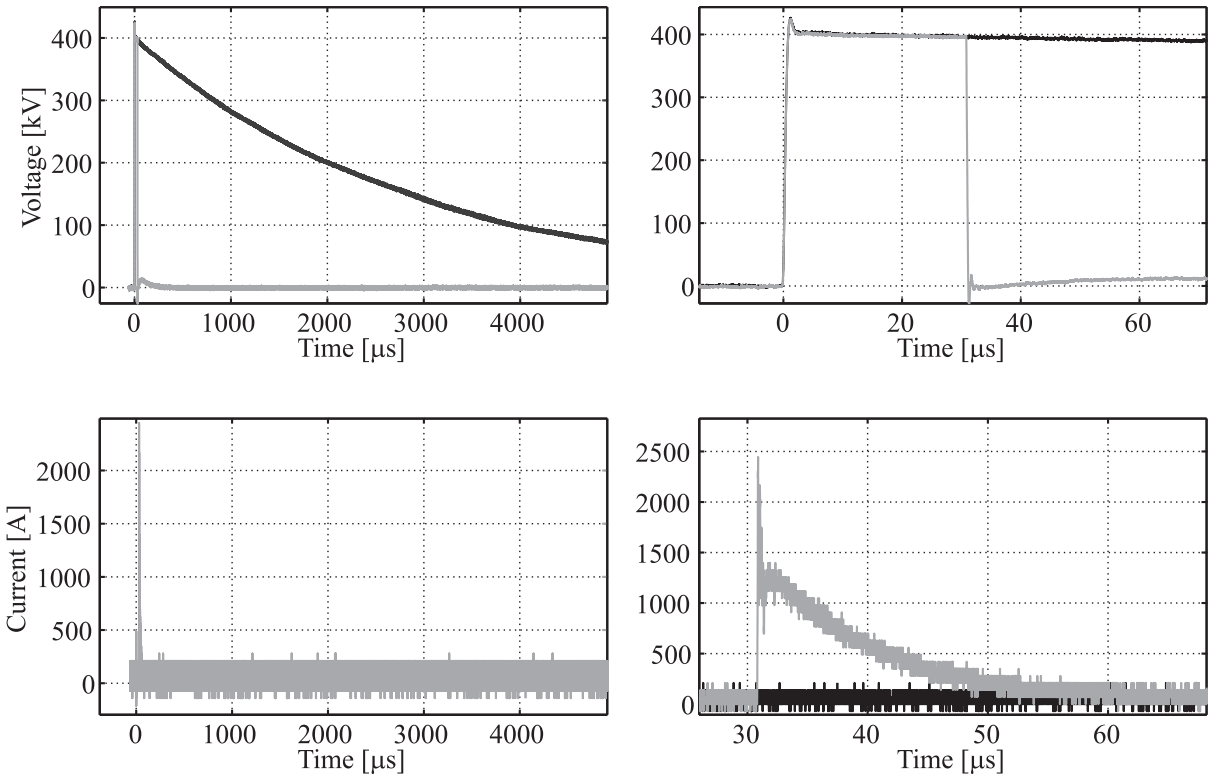

Figure 3.15.: Measured hybrid Lightning/Switching impulse voltage form and corresponding current form with discharge to ground

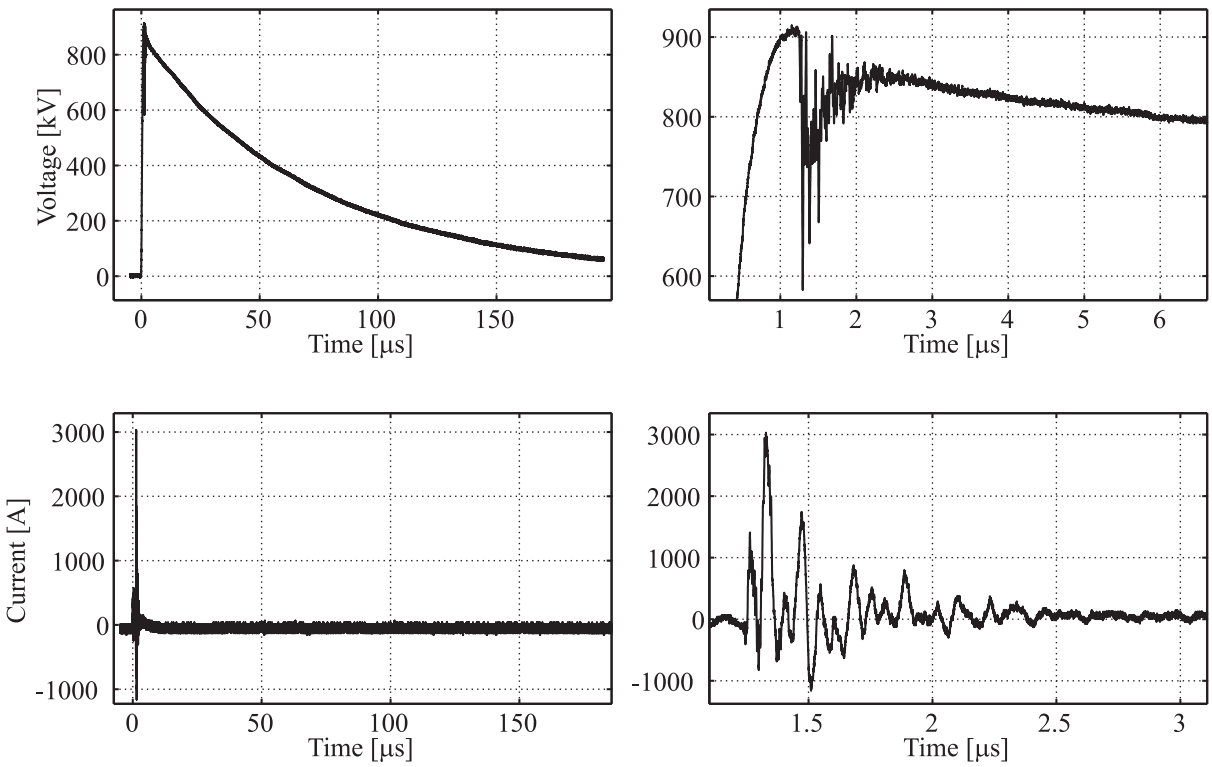

Figure 3.16.: Measured Lightning impulse voltage form and corresponding current form with discharge to limiting resistor

3.3.2. Impact on Electrode

Through a very coarse description of the arc having a time independent arc root voltage v_{root}, the energy dissipated at the electrode surface can be estimated as:

$$E_{arc} = \int_{t=0}^{t=\infty} v_{\text{root}} \cdot i(t)dt \tag{3.3}$$

Therefore the impact on the electrode is directly proportional to the duration and amplitude of the current flow. Inspections by microscope showed the impact of different current shapes on the surface of the electrode. In the case of the complete discharge of the Marx Generator to ground (c.f. Fig. 3.15) the biggest damage of the electrode resulted, as implied by Eq. (3.3) and depicted by spot c.) in Fig. 3.17. The craters had a diameter of several mm and the surface roughness was increased as sensed by hand. The experiments with lower current amplitude showed less impact on the electrode. Limited current led to dark base points according to spot a.) in Fig. 3.17 and breakdown on floating electrode to light base points according to spot b.) in Fig. 3.17. Besides the coloring, no change in surface roughness could be detected, neither by hand nor by magnifying microscope.

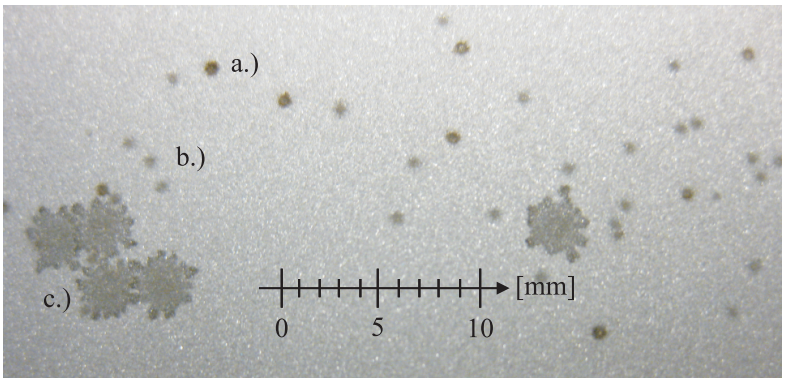

Figure 3.17.: Damage of electrode surface due to different energy impact

3.3.3. Example of Constant Voltage Series

To execute a series of constant voltage experiments, the test vessel and the electrodes were prepared according to section 2.2.3. Each measurement consisted of charging the Marx generator, discharging, recording and storaging of measured voltage and current forms and of the picture taken. Subsequent steps included grounding the setup, ungrounding, application of the AC-source (between 5%-10% of test voltage) to clear ion density in the gas (30 s), break-time (30 s), and final grounding.

Data Postprocessing

After a series was finished, a number of postprocessing functions were used to compute peak voltage, voltage drop, peak current, time to breakdown (Δt from 5% prospective impulse voltage peak to breakdown) and the base point of arc on the electrode surface.

An example series of voltage applications of a fixed arcing contact versus plane electrode (30 mm contact separation) is shown in Fig. 3.18. These measurements were conducted with lightning impulse voltage and an installed limiting resistor (according to Fig. 3.16). The arcing contact carried the negative polarity. The test vessel was filled with SF_6 at 0.6 MPa absolute pressure.

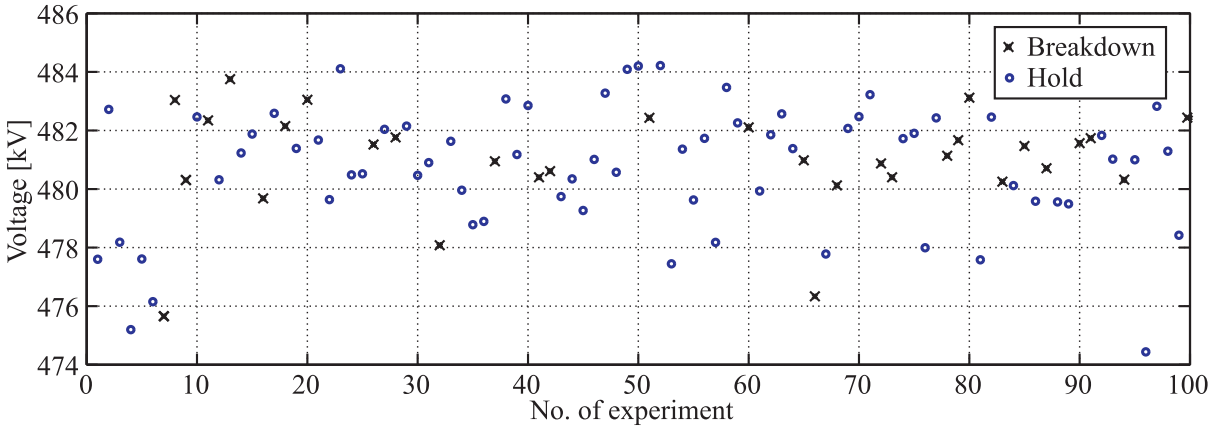

Figure 3.18.: Peak voltages recorded during execution of experimental series. The small deviation of the voltage peak values and the stochastic sequential occurrence of breakdowns indicate a proper measurement

The mean value of the peak voltage applied was 480.8 kV with a standard deviation of 2.02 kV (Fig. 3.18). The series, consisting of 100 voltage applications had 31 breakdowns and 69 holds resulting in an estimated breakdown probability of $p = 31\%$. The mathematical tests for statistic independence resulted in $|z| = 0.75$ for the iteration-test and a maximum $|z|$ of 1.38 and 0.988 when comparing the breakdown probability of groups of twenty measurements with each other and to the probability of the whole series.

In Fig. 3.19 a superposition of all breakdown photos is shown, as well as the reconstructed arc root points. The root points showed low clustering and no location was hit twice consecutively. The time to breakdown analysis revealed that all breakdowns happened after the peak of the lightning impulse voltage (Fig. 3.19c.))

From this series, the following findings were derived:

- The criteria for statistical independency were fulfilled with minimum 90% certainty.
- The root point evaluation showed no obvious clustering.

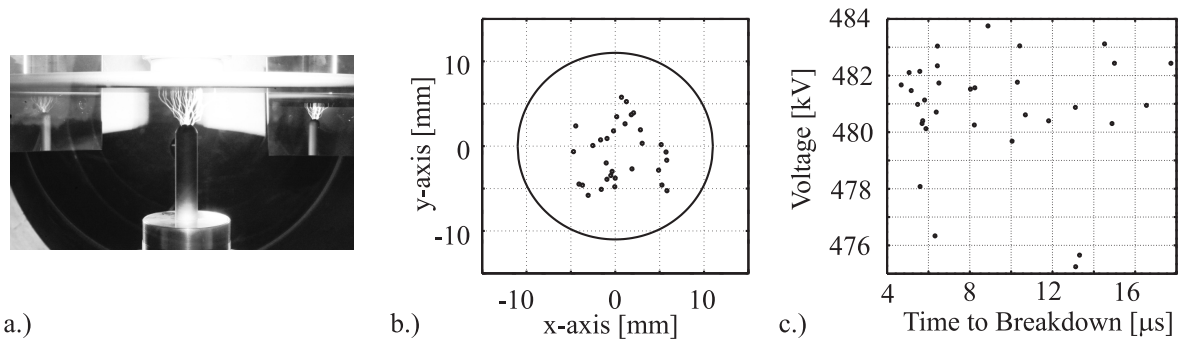

Figure 3.19.: Example of results of constant voltage series: a.) Photos of breakdowns on electrode b.) Reconstructed arc root points on electrode c.) Time to breakdown

- The direct linear correlation coefficient between the deviation in peak voltage from the mean value and breakdown occurrence was less than 6%, implying the series can be interpreted as 'constant' voltage.

Analysis of Root Point Reconstruction

In order to determine the accuracy of the root point reconstruction, a comparison was derived after the execution of a constant voltage experimental series with the main contact of the fixed contact side versus a plane electrode. A photo of the ring electrode and the respective reconstruction is shown in Fig. 3.20. An explicit comparison was not possible since the photography of the electrode and the projection of the arc root points onto the electrode are not subject to the same distortion. However, a manual comparison shows that the patterns are very similar.

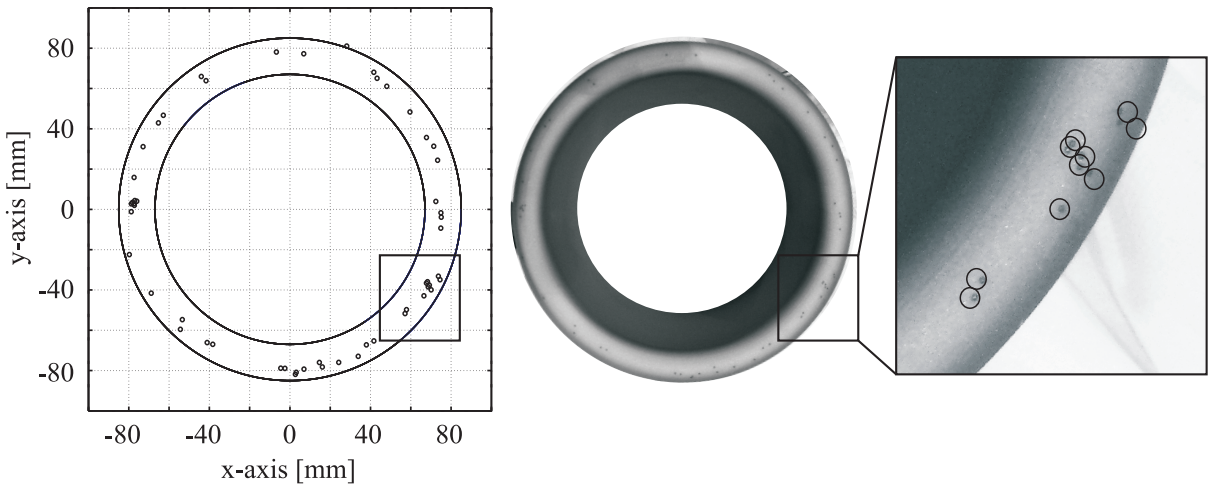

Figure 3.20.: Arc root points: Reconstruction during experimental series and photo of electrode after series

Analysis of Breakdown Path

Typical breakdown pictures are shown in Fig. 3.21. The left hand side was recorded at experiments with voltage of negative polarity at the arcing contact. This application resulted exclusively in single breakdown paths. Fig. 3.21b.) shows a breakdown occurring at the opposite voltage polarity. The branched structure was often observed at this polarity.

a.) 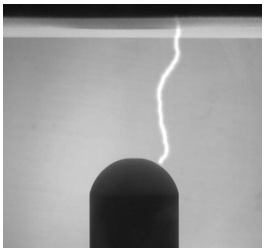 b.) 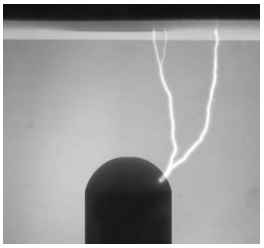

Figure 3.21.: Differing breakdown paths dependent on the voltage polarity applied.
a.) negative arcing contact
b.) positive arcing contact

3.3.4. Statistical Independence

In the present case, the practice of choosing a break between the measurements of 300 s was not sufficient to achieve statistically independent measurements. While experiments with a pressure of 0.2 MPa gave reliable, statistically independent measurements, comparable experiments at a pressure of 0.6 MPa always resulted in series with obvious dependent nature (e.g.: Fig. 3.22). The statistical dependence remained for break-times of 300 s, 480 s and 600 s.

The application of an AC-source between the individual measurements provided an adequate and time saving means of ensuring statistically independent results by removing excessive ions after breakdown occurrence. It was concluded that the ion density in the gas had a major impact on the result and reliability of breakdown experiments. Based on this finding and supported by a calculation (shown in Appendix D) it was concluded that the application of an electric field to control ion density resulted in the removal of all the ions in the test vessel. Once the voltage is turned off, the ion density rises again due to natural cosmic radiation at a quite constant rate [33] until it reaches equilibrium between ionization and recombination. This finding implied certain important consequences for general experimental techniques:

When carrying out **constant voltage tests** at 0.6 MPa SF_6 without applying an electric field to sweep the excessive ions, the equilibrium ion density after a breakdown cannot be reached within a reasonable break times. Therefore, a voltage source has to

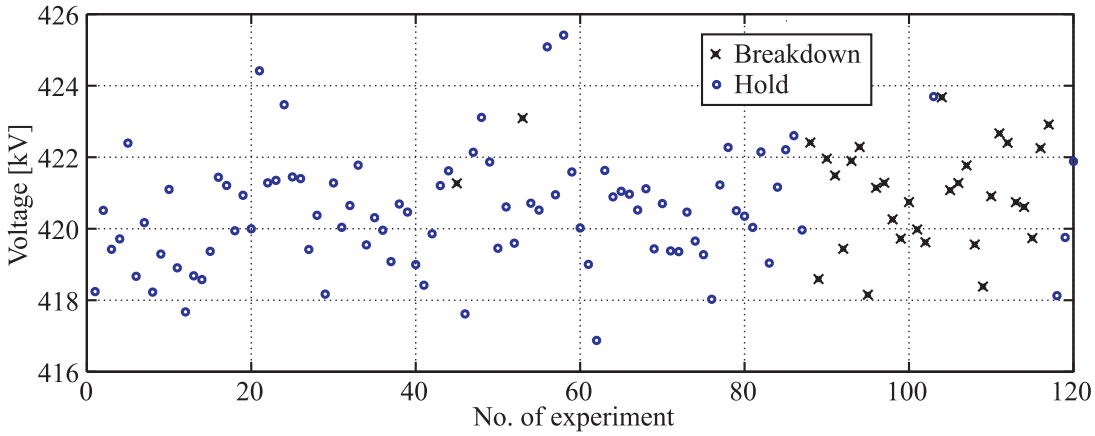

Figure 3.22.: Example of experimental series with clear statistical dependence - 87 measurements in series with two breakdowns followed by 33 measurements with 4 holds

be installed and the break time between the removal of this voltage source and the next voltage application must be constant to reach identical conditions or sufficiently long to reach equilibrium ion density before each measurement. These statements are irrespective of the voltage shape used.

The application of **rising voltage tests** with AC or DC voltage avoids this difficulty since any ions are swept through the individual measurements itself. In this specific case no voltage source between the measurements and no break time is needed to gain statistically independent results. On the other hand, the usage of rising voltage tests with impulse voltage at high pressurized SF_6 will seldomly result in statistically independent experiments. This can be justified with two arguments:

1. If excessive ions are swept in between the impulse-voltage applications, the rising charging time of the Marx-Generator with rising desired peak voltage will result in different equilibrium ion densities at the time of voltage application.

2. If excessive ions are not swept in between the measurements, impulse voltage applications which do not result in breakdown will result in the same effect as the application of an electric field in between the measurements. But due to the short impulse time and according to Eq. (D.1) the sweep might be incomplete and result in an undefined state.

3.4. Results - Measurements

All the results presented in the following section were obtained through breakdown tests with a lightning impulse voltage, an absolute SF_6 pressure of 0.6 MPa in the test vessel and installed limiting resistor.

3.4.1. Fixed Side Contacts vs Plane Electrode - Equal Distance

In order to get insight into the breakdown probability distribution of multi-contact systems three different configurations were investigated. These configurations are depicted in Fig. 3.23a.)- c.). There is arcing contact vs plane electrode (Fig. 3.23a.)), main contact vs plane electrode Fig. 3.23b.) and fixed contact system vs plane electrode (Fig. 3.23c.)). Contact separation and contact distance were identical and set to 30 mm for all three arrangements.

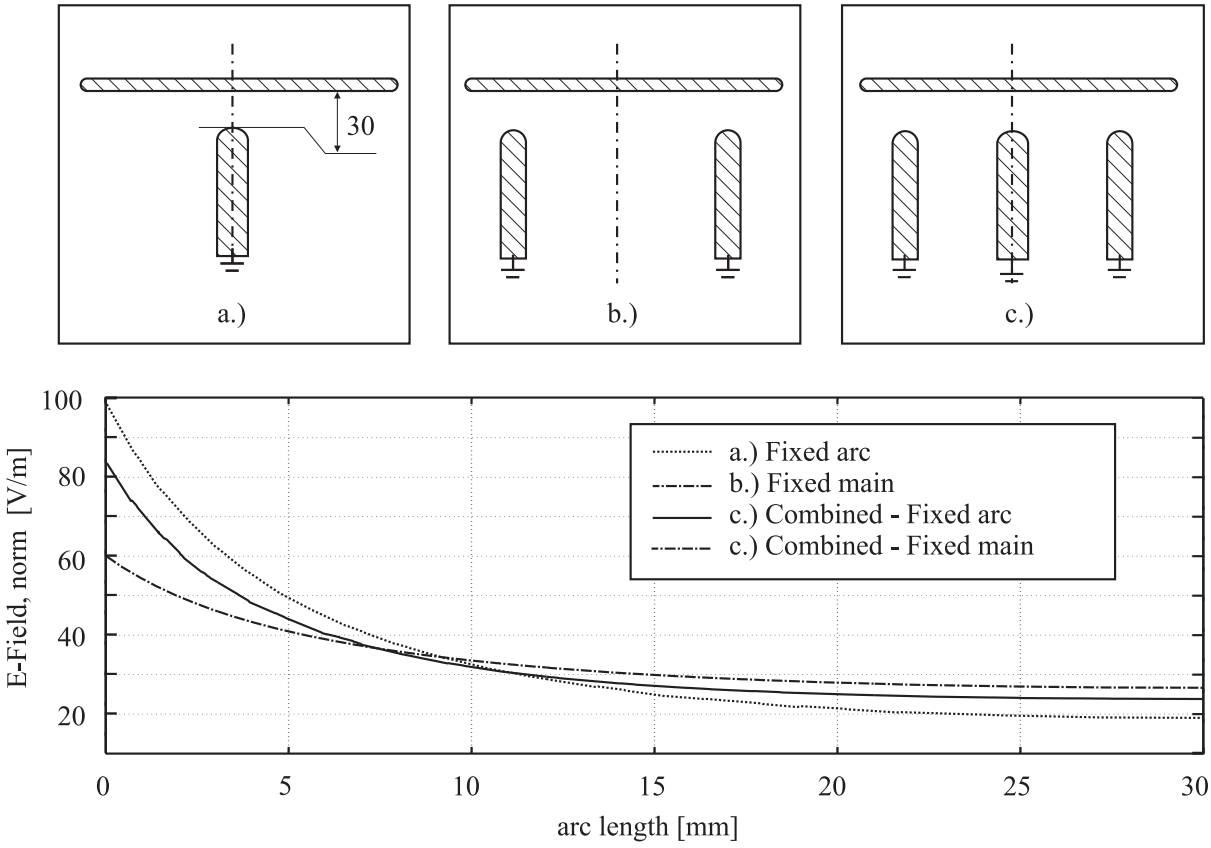

Figure 3.23.: Fixed contact vs. plane arrangement - equal distance:
single and combined electrode arrangements and corresponding electric fields calculated along shortest distance with 1 V potential difference. In the combined electrode arrangement c.) the main contact electric field is identical to b.) whereas the elecric field of the arcing contact is lower compared to a.)

In the lower part of Fig. 3.23 the calculation of the absolute value of the electric field

is shown for each electrode arrangement with an applied potential difference of 1 V. The field was calculated along the shortest distance between opposite electrodes. The characteristic electric field values of all electrode arrangements are summarized in Tab. 3.2. The coordination factor C is the ratio between maximum field on the arcing and main contacts.

The arcing contact vs plane arrangement showed the highest maximum electric field with the lowest field efficiency factor. It showed also the steepest decrease in electric field along the axis of symmetry. In contrast, the electric field between the main contact and the plane electrode had the lowest maximum value but a rather low decay. Consequently the electric field exceeded the value of the arcing contact field at approximately 9 mm from the tip of the electrode (compare to 'arc length' in Fig. 3.23). Interestingly, the electric field between main and contact and plane electrode was almost unaffected by the introduction of the arcing contact (c.f. Fig. 3.23c.)). In contrast, the maximum electric field at the arcing contact was significantly lower in the combined arrangement compared to the single arrangement. In this case the arcing contact was partially shielded by the main contact.

Table 3.2.: Electric Field Values for Contact System with 30 mm Contact distance according to Fig. 3.23 with E_0 as mean electric field, i.e. 1 V divided by the shortest distance between the electrodes

	E_{max} [V/m]	E_0 [V/m]	η	C
a.) arcing contact only	98	33.3	0.34	
b.) main contact only	60	33.3	0.56	
c.) combined contact system				1.4
arcing contact	84	33.3	0.4	
main contact System	60	33.3	0.56	

Fig. 3.24 shows the fitted breakdown probability curves on the basis of a binomial distribution. The distribution in the upper part of the figure was recorded with negative polarity on the inhomogeneous contact side, the lower part of the figure for the opposite polarity as indicated by the letters (A) and (B) in Fig. 3.24. The boundaries for the probability distribution are the 95% confidence intervals. Each curve is the result of between 161 to 600 individual measurements.

The arcing contact vs plane arrangement (c.f. Fig. 3.23a.)) showed the lowest breakdown voltage when the voltage polarity on the arcing contact was negative. In this case the arcing contact had a 50%-breakdown voltage V_{BD-50} of 485 kV with a standard deviation of $\sigma = 6.8$ kV when the binomial distribution was approximated with a normal distribution (curve a.) in upper part of Fig. 3.24). The main contact showed a breakdown voltage V_{BD-50} of 724 kV, being 49% higher than the arcing contact with $\sigma = 13.6$ kV

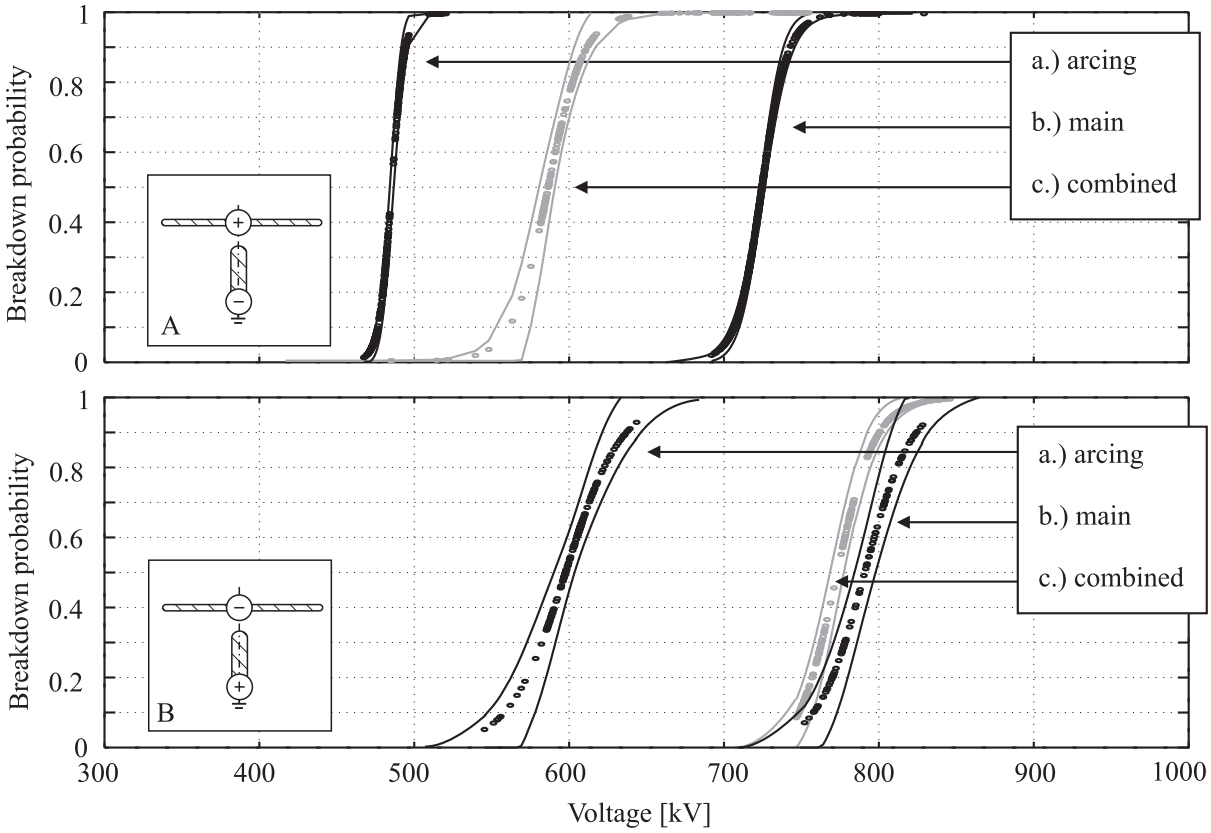

Figure 3.24.: Breakdown probability curves for fixed contact vs plane arrangement for single and combined electrode arrangements with equal distances according to Fig. 3.23. Positive polarity shows higher breakdown voltages and overlapping breakdown probabilities

(curve b.) in upper part of Fig. 3.24). The combined contact system with arcing and main contact 30 mm separated from the plane electrode had $V_{BD-50} = 587\,\text{kV}$ with $\sigma = 19.1\,\text{kV}$ (curve c.) in upper part of Fig. 3.24). The combined contact system showed an increase of breakdown voltage of 21% compared to the arcing contact vs plane arrangement while its maximum electric field was 14% smaller . In this arrangement all breakdowns occurred on the arcing contact.

With positive polarity at the arcing contact, the breakdown voltage of the arcing contact vs plane arrangement was $V_{BD-50} = 598\,\text{kV}$ with a standard deviation of $\sigma = 29.9\,\text{kV}$ (curve a.) in lower part of Fig. 3.24). Breakdown voltage increased by 23% compared to the same arrangement with negative polarity at the arcing contact. Compared to negative polarity, the main contact breakdown voltage increased by 9% to a value of 792 kV with $\sigma = 25\,\text{kV}$ and the breakdown voltage of the combined contact system reached 774 kV and $\sigma = 21.1\,\text{kV}$ (curve b.) and c.) in lower part of Fig. 3.24). In the latter case the breakdown voltage increased by 32% due to polarity effect.

All electrode arrangements had in common that the breakdown voltage was generally lower with negative polarity at the inhomogeneous electrode side. Further, all results

recorded with this polarity showed a smaller standard deviation σ of the normal distribution.

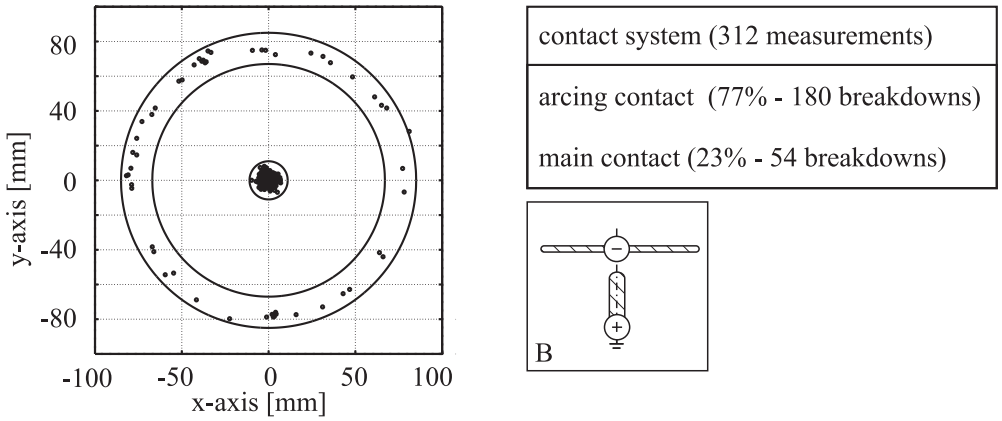

Figure 3.25.: Breakdown distribution on main and arcing contact in the equal distance arrangement Fig. 3.23c.), when tested with positive Lightning Impulse voltage

Notably, in breakdown experiments with the combined electrode arrangement at positive polarity - setup B in Fig. 3.23 breakdowns on both, arcing and main contacts were observed. The distribution of breakdowns on the main and arcing contacts is depicted in Fig. 3.25. The series consisted of a total of 312 measurements with 234 breakdowns and 180 breakdowns on the arcing contact (77%) and 54 breakdowns on the nominal contact (23%).

The arc root point distribution on the right in Fig. 3.25 shows an even distribution on the surface of both electrodes, implying that no significant change in electrode surface condition happened during the experiment.

The time to breakdown of all the measurements is shown in Fig. 3.26 whereas the index a.)-c.) refers to the different electrode arrangements according to Fig. 3.23. The time to breakdown was recorded to be as high as 25 μs for the main contact vs plane arrangement b.). This setup also showed a distinctive trend of longer time to breakdown values at negative polarity on the contact side. This trend was also visible, although not that apparent in the arcing contact or combined contact vs plane arrangement. Noticeable, at negative polarity the time to breakdown did hardly become smaller with rising breakdown voltage.

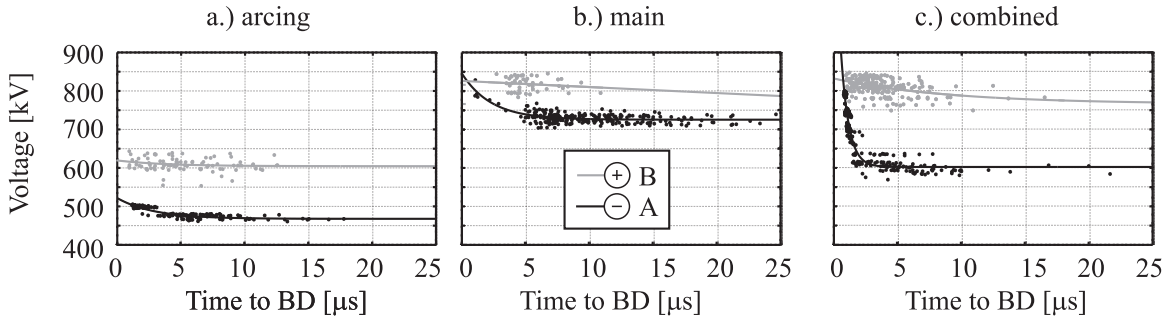

Figure 3.26.: Time to breakdown curves for fixed contact vs plane arrangement for single and combined electrode arrangements with equal distances according to Fig. 3.23

3.4.2. Fixed Side Contacts vs Plane Electrode - Equal Field

The electrodes used in this series were the same as in the previous experiment but different contact distances were set. In the combined system (arrangement c.) in Fig. 3.27) the arcing contact was shifted towards the plane electrode in order to get the same maximum electric field at its tip as the single contact with 30 mm contact distance. Gap width was reduced by 6 mm. The arrangement and the corresponding fields along the shortest distance between the electrodes are depicted in Fig. 3.27.

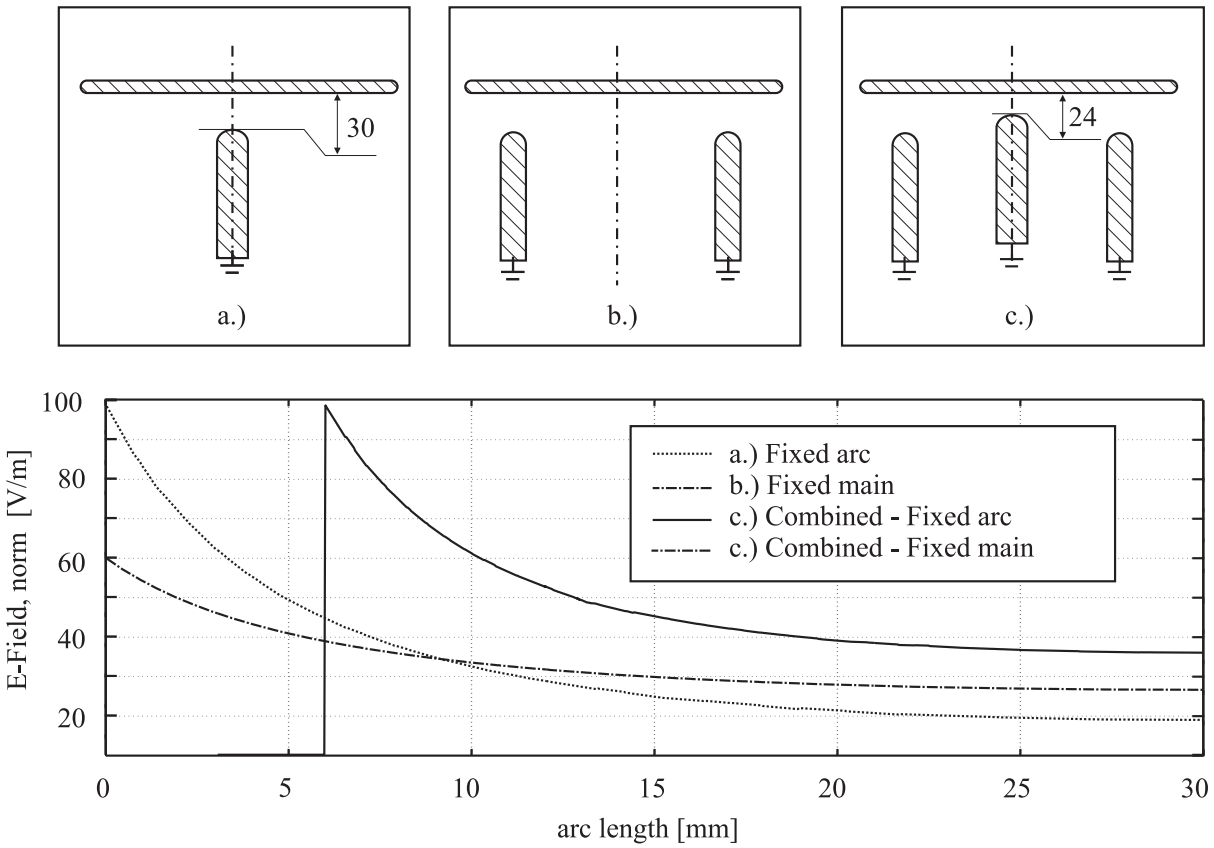

Figure 3.27.: Fixed contact vs. plane arrangement - equal field:
single and combined electrode arrangements and corresponding electric fields calculated along shortest distance with 1 V potential difference. The maximum electric fields in combined and single arrangements were identical, achieved by an exposure of the arcing contact in the combined contact system c.)

As in the previous section, the field between main contact and plane electrode remained identical for arrangement b.) and c.) in Fig. 3.27). In contrast to the previous section the maximum electric field between the arcing contact and plane electrode were also similar in arrangement a.) and c.). Although the decay of the electric field between arcing contact and plane electrode was lower in the combined arrangement (c.f.Fig. 3.27c.)) the maximum electric field and the initial decay were almost identical. The characteristic

field values are summarized in Tab. 3.3. It is noteworthy that only a few values changed

Table 3.3.: Electric Field Values for 30/24 mm Contact System according to Fig. 3.28

	E_{max} [V/m]	E_0 [V/m]	η	C
a.) arcing contact only(30 mm)	98	33.3	0.34	
b.) main contact only (30 mm)	60	33.3	0.56	
c.) contact system				1.63
arcing contact (24 mm)	98	41.6	0.42	
main contact System (30 mm)	60	33.3	0.56	

between the different settings (summarized in Tab. 3.2 and Tab. 3.3). Only the arcing contact field in the combined arrangement was higher, resulting in a higher field efficiency factor and a higher coordination factor.

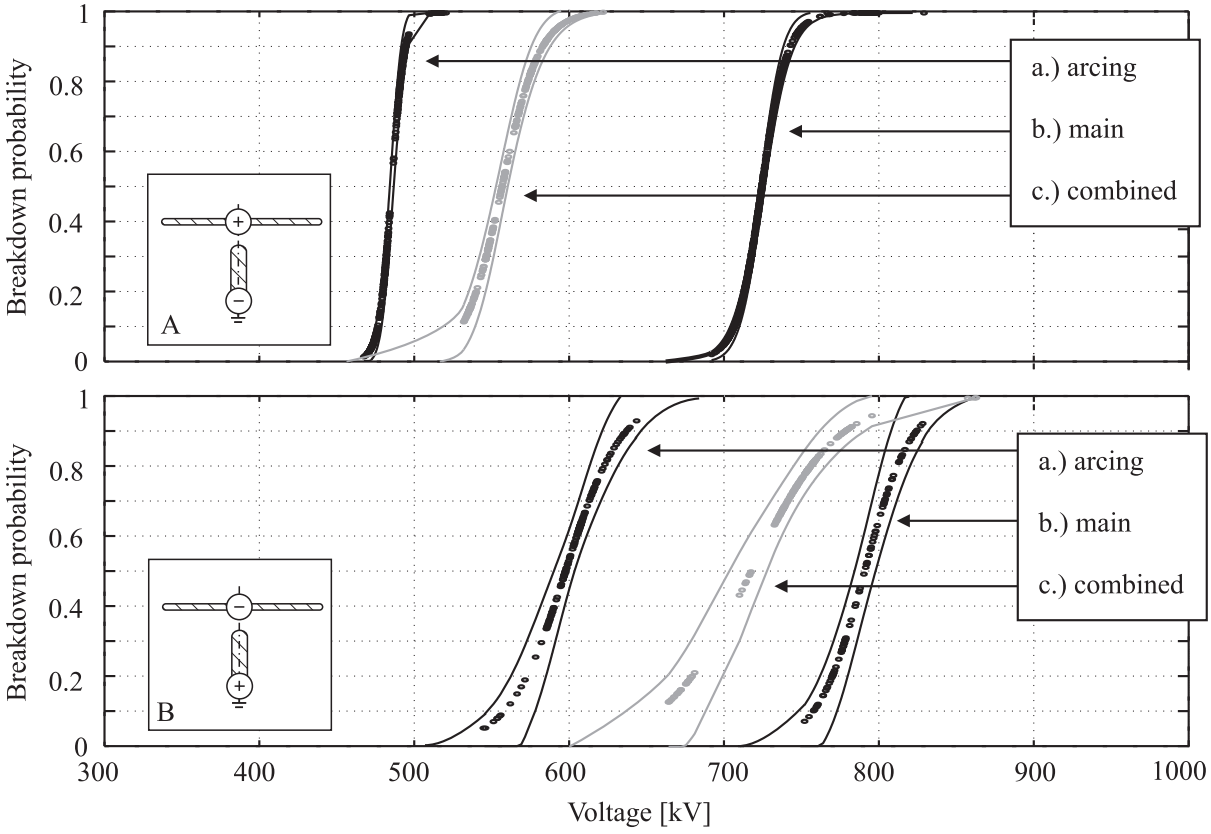

Figure 3.28.: Breakdown probability curves for fixed contact vs plane arrangement for single and combined electrode arrangements with equal maximum electric fields according to Fig. 3.27. Positive polarity shows higher breakdown voltages and overlapping breakdown probabilities

A summary of the breakdown probability and time to breakdown is shown in Fig. 3.28 and Fig. 3.30 respectively. The breakdown probability curves of arcing contact and main contact vs plane are the same as in the previous section and are not described here in

detail. Although the maximum electric field at the tip of the arcing contact was similar in the arcing contact vs plane arrangement (c.f. Fig. 3.27a.)) and the combined contact vs plane arrangement (c.f. Fig. 3.27c.)) the breakdown voltage of the combined system differed significantly. The breakdown probability of the combined system according to Fig. 3.27c.) showed a V_{BD-50} of 557 kV with a standard deviation of $\sigma = 20.1$ kV for negative polarity at the contact side (A) and $V_{BD-50} = 725$ kV and $\sigma = 38.5$ kV at the opposite polarity (B). At polarity A the combined contact system showed a 15% higher V_{BD-50}; at polarity B the difference was 21% compared to the arcing contact vs plane arrangement (curves a.) in Fig. 3.28) . In the combined contact, arrangement c.)the difference in breakdown voltage due to the voltage polarity was approximately 30%.

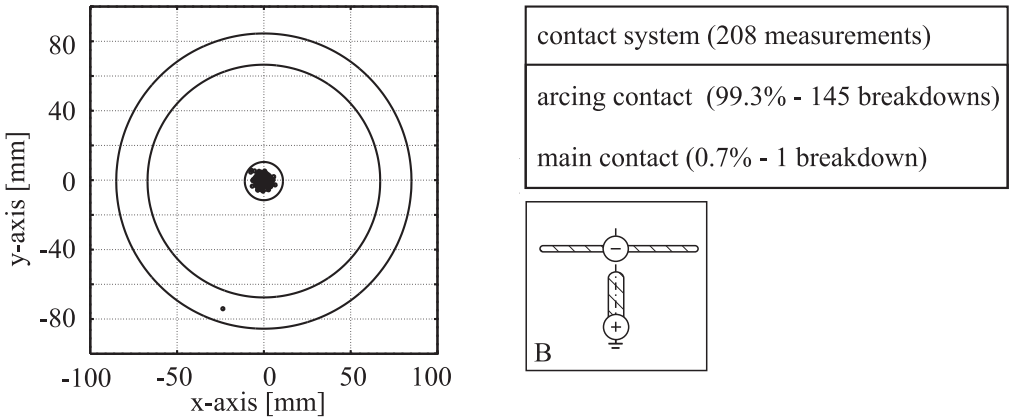

Figure 3.29.: Breakdown distribution on main and arcing contact in the equal field arrangement Fig. 3.27c.), when tested with positive Lightning Impulse voltage

In the combined system breakdowns occurred on both contacts at positive polarity on the inhomogeneous electrode side. Although the coordination factor C was increased, the breakdown probability on the main contact was bigger than zero. Fig. 3.29 depicts the arc root point locations. Out of the whole experimental series, one breakdown occurred on the main contact side. 208 measurements were performed with 145 breakdowns on the arcing contact (99.3%) and one breakdown on the main contact (0.7%).

The time to breakdown curves in Fig. 3.30a.) and b.) are the same as in the previous section and are only shown for a comparison with the arrangement c.). The time to breakdown became only marginally smaller with rising breakdown voltage. This effect was more pronounced at the negative polarity at the contact system.

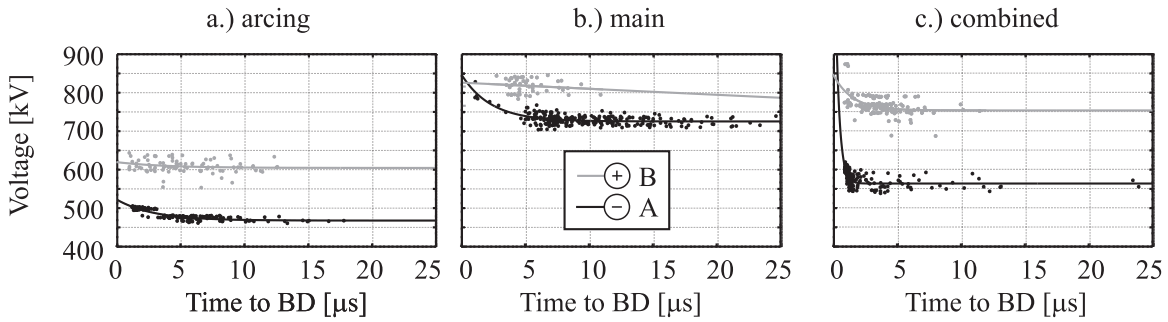

Figure 3.30.: Time to breakdown curves for fixed contact vs plane arrangement for single and combined electrode arrangements with equal field according to Fig. 3.27

3.4.3. Complete Contact System

Next, the breakdown probability distribution was evaluated for a complete circuit breaker contact system consisting of four contacts as depicted in Fig. 3.31. The lower part of Fig. 3.31 shows electric fields calculated along the shortest distance between the contacts, when a voltage of 1 V was applied.

Contact separation across the main contacts was 25 mm for arrangement a.) and 10 mm for arrangement b.) in Fig. 3.31. In order to minimize the influence of different contacts, the shift of the arcing contacts with respect to the main contacts was done such that the coordination factor C of maximum fields was close to 1 on the moving contact side. This was achieved by exposing the arcing contact of the moving contact side by 3 mm with respect to the main contact whereas the arcing contact of the fixed contact side was withdrawn by 5 mm towards the main contact. Noteworthy, the electric fields in Fig. 3.31

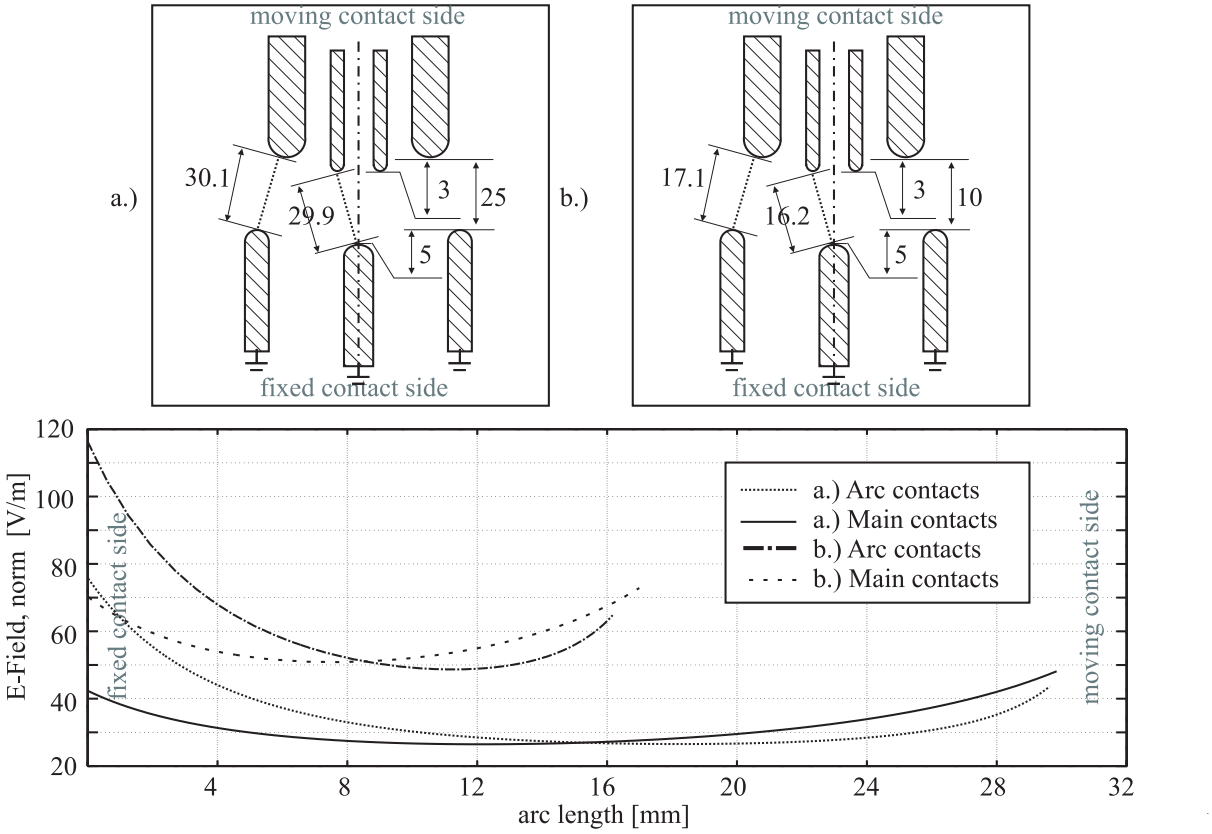

Figure 3.31.: Complete contact system with 25 mm and 10 mm contact separation. Schematic drawing and corresponding electric fields along shortes distance between the electrodes. Electric fields were calculated with 1 V potential difference between the electrodes and the relative distance of the electrode chosen to show unitary coordination on the moving contact side

were calculated along the shortest distance between the contacts and did therefore not necessarily cover the maximum electric field of the respective contact. Consequently, the required coordination factor C is not directly visible from these fields.

Maximum electric field on the electrode surface E_{max} and maximum electric field between the shortest distance of the electrodes $E_{max-line}$ as displayed in Fig. 3.31 are summarized for both arrangements in Tab. 3.4 and Tab. 3.5. Although the arcing contact of the fixed contact side was shifted away from the opposite electrode, its electric field showed a superelevation compared to the main contact. The coordination factor C on the fixed contact side was in any case higher than in the previous sections 3.4.1 and 3.4.2.

Table 3.4.: Electric field values for complete contact system, 25 mm gap distance

	C	fixed arc	fixed main	moving arc	moving main	C
E_0 [V/m]		33.4	33.2	33.4	33.2	
E_{max} [V/m]	1.85	79.9	43.3	49.7	50	0.99
$E_{max-line}$ [V/m]	1.75	75.3	43.0	42.9	49.6	0.86
η_{max}		0.42	0.77	0.67	0.66	
η_{line}		0.44	0.77	0.78	0.67	

Table 3.5.: Electric field values for complete contact system, 10 mm gap distance

	C	fixed arc	fixed main	moving arc	moving main	C
E_0 [V/m]		61.7	58.5	61.7	58.5	
E_{max} [V/m]	1.81	127.3	70.5	74	74.3	1
$E_{max-line}$ [V/m]	1.66	116.6	70.4	64.5	74.5	0.87
η_{max}		0.48	0.83	0.83	0.79	
η_{line}		0.53	0.83	0.96	0.79	

The results of the breakdown experiments are shown in Fig. 3.32. When the fixed contact was tested with negative polarity (A) it showed a 50%-breakdown voltage of $V_{BD-50} = 635\,\text{kV}$ with a standard deviation of $\sigma = 14.8\,\text{kV}$ for 25 mm contact separation (c.f. Fig. 3.31a.)) and $V_{BD-50} = 426\,\text{kV}$ with a standard deviation of $\sigma = 23.1\,\text{kV}$ for 10 mm contact separation (c.f. Fig. 3.31b.)). The breakdown voltage for arrangement a.) was 49% higher than in arrangement b.) whereas the corresponding maximum electric field was 50% higher. All the breakdowns occurred on the arcing contacts.

When stressing the contact system with positive polarity on the fixed contact side, the breakdown voltages were significantly higher. Arrangement a.) had $V_{BD-50} = 868\,\text{kV}$ and $\sigma = 14.3\,\text{kV}$ what represented an increase in breakdown voltage of 37% due to the polarity. Arrangement b.) showed an increase of 38% which meant a breakdown voltage of $V_{BD-50} = 588\,\text{kV}$ and $\sigma = 10.8\,\text{kV}$. The ratio of maximum electric fields on the arcing

contact of the fixed contact side in (B) was the same as (A) (c.f. Fig. 3.31 and Fig. 3.32), namely 50% and the ratio of the breakdown voltages was 47%.

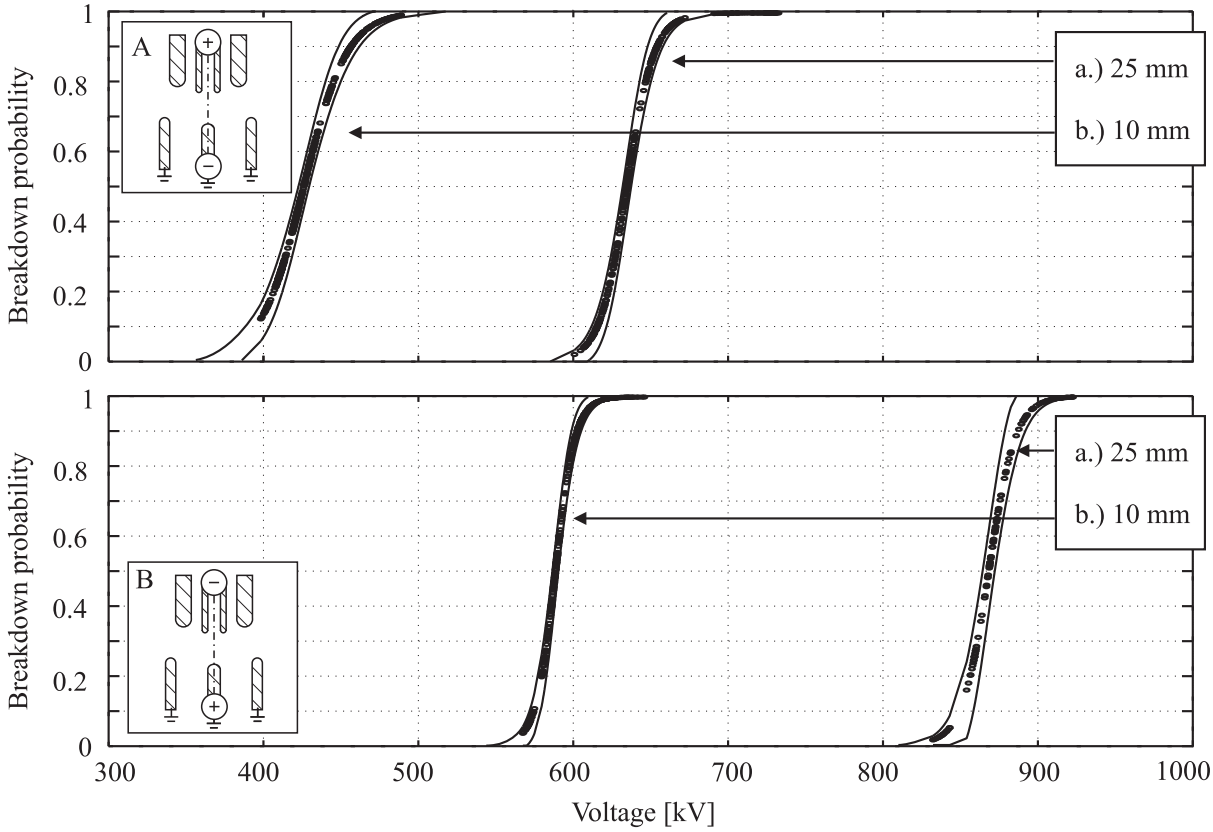

Figure 3.32.: Breakdown probability curves for complete contact system with contact separation of 10 mm and 25 mm according to Fig. 3.31. Positive polarity shows general higher breakdown voltages

In contrast to the breakdown experiments with the fixed contact side on negative polarity (A) where all breakdowns occurred on the arcing contacts, breakdowns occurred on arcing and main contacts when the fixed contact side was on positive polarity (B). In Fig. 3.33 the distribution between breakdowns on the main and arcing contact is shown for both contact separations. The 25 mm arrangement was tested with 142 measurements, whereas 76 breakdowns happened on the arcing contacts (88.4%) and 10 breakdowns on the main contacts (11.6%). At 10 mm contact separation 375 measurements were performed with 246 breakdowns on the arcing (96.5%), 9 on the main contacts (3.5%).

In both investigations a clustering of arcing root points on approximately one third of the electrode could be detected. A detailed analysis of the arc root points however showed that their sequential appearance was stochastic in this area. Furthermore, no surface damage could be detected on the electrode. For these reasons and the fact that the arc root point distribution still covered quite a wide area and not a specific point, it appeared more likely that the reason for clustering is caused by surfaces of opposite contacts which were not exactly parallel to each other.

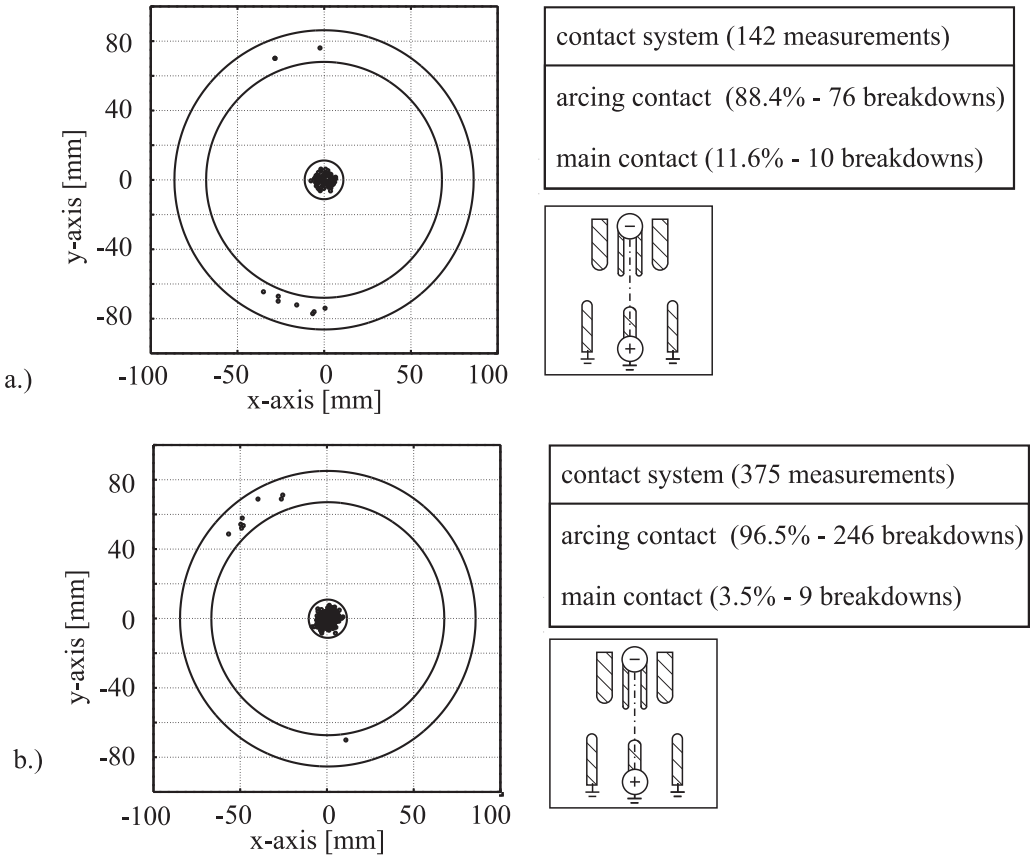

Figure 3.33.: Breakdown distribution on main and arcing contact in the complete contact system with 10 mm and 25 mm contact separation when tested with positive Lightning Impulse voltage. Main contact breakdown probability is significantly reduced with decreasing contact separation

The time to breakdown curves of this experimental series are shown in Fig. 3.34. For both arrangements and polarities times to breakdown were in the range of 1 μs and 20 μs. No breakdown happened after 20 μs and only very few were faster than 1 μs, i.e. happened in the rising front of the applied impulse voltage. Rising breakdown voltages did not provoke linearly decaying time to breakdowns. This non-linearity was especially pronounced when the inhomogeneous contact side was stressed with negative polarity.

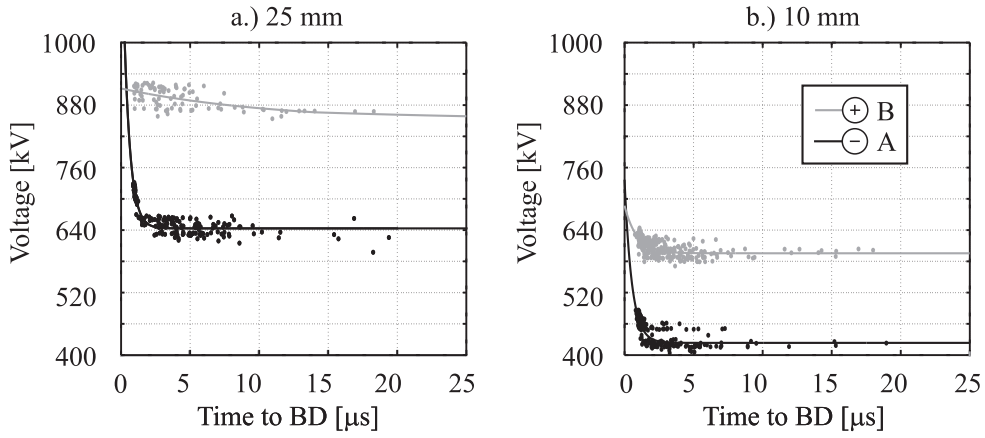

Figure 3.34.: Time to breakdown curves for complete contact system with 10 mm and 25 mm contact separation according to Fig. 3.31

3.5. Results - Calculation

The results presented in this section contain the theoretically calculated breakdown probabilities for the equal field (c.f. section 3.4.2) and equal distance arrangement (c.f. section 3.4.1). It was assumed that at negative polarity a first electron was present (by field emission) as soon as E_{cr} was exceeded. In this case the evaluation of the streamer criterion was used to calculate the breakdown voltage. The streamer integral (section 2.1.3) was performed on the basis of an electric field calculation and calculated along the shortest distance between the electrodes. The approximation for α^* was taken from [12]. The actual breakdown probability curve was distributed between minimum and maximum value of k_{st}.

At positive polarity, the evaluation of the volume-time criterion was used to judge the breakdown probability curve. Measured voltage forms as presented in section 3.3.1 were used to scale the electric field values obtained from FEM-calculations. The electron production rate $\frac{dn_e}{dt}$ was calculated by using the detachment rate from [39] and an initial ion density of $I_0 = 1000\,\mathrm{IonPairs/cm^3}$. This ion density was calculated according to 60 s of ion generation by radiation at a rate of approximately 17 IP/cm s for a laboratory 10 m below ground level (compared to 26-55 IP/cms in [40]).

3.5.1. Fixed Side Contacts vs Plane Electrode - Equal Distance

In Fig. 3.35 the calculated breakdown probability curves are displayed for the three different electrode arrangements and both polarities. For negative polarity, the lowest breakdown voltage was calculated for the arcing contact vs. plane arrangement as $V_{BD-50} = 623\,\mathrm{kV}$ and for the main contact vs. plane arrangement as $V_{BD-50} = 975\,\mathrm{kV}$. The corresponding decision length x_{crit} was 750 μm and 990 μm respectively. The combined contact system resulted in a calculated breakdown voltage of $V_{BD-50} = 734\,\mathrm{kV}$ for the arcing contact and a $V_{BD-50} = 982\,\mathrm{kV}$ for the main contact and a x_{crit} of 750 μm and 1000 μm respectively. These two breakdown curves did not show an overlap.

For positive polarity, the predicted breakdown voltage was higher for arcing contact vs plane as well as for main contact vs plane, being $V_{BD-50} = 894\,\mathrm{kV}$ and $V_{BD-50} = 1120\,\mathrm{kV}$. The combined contact system showed an increased breakdown voltage of $V_{BD-50} = 1078\,\mathrm{kV}$ for the arcing contact and $V_{BD-50} = 1120\,\mathrm{kV}$ for the main contact. Although the 50%-breakdown values are different, the breakdown probability curves show an overlap.

3.5.2. Fixed Side Contacts vs Plane Electrode - Equal Field

The breakdown probability curves calculated for the equal field arrangement are displayed in Fig. 3.36. The curves for arcing contact and main contact vs plane are the same as in

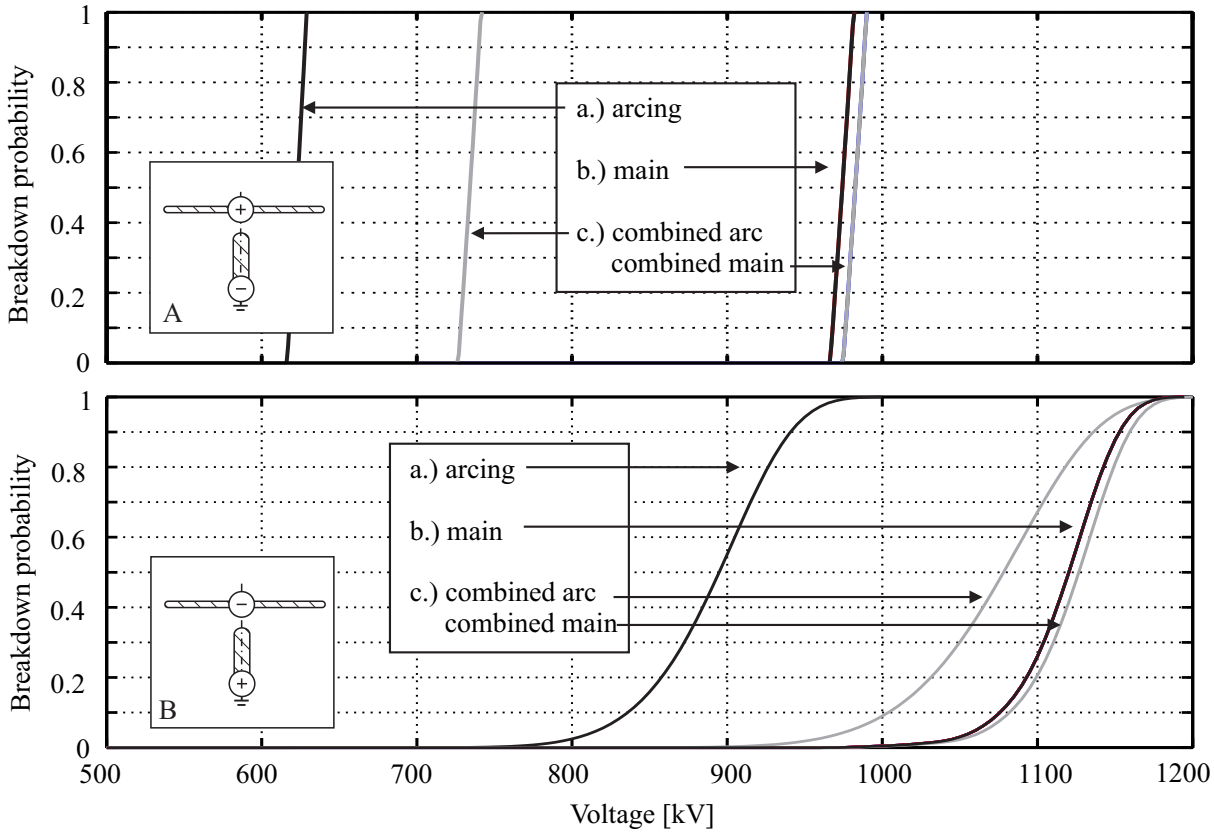

Figure 3.35.: Calculated breakdown probability curves for equal distance arrangement according to Fig. 3.23

the previous section and are not described further here. The breakdown voltage for the combined contact system with reduced distance for the arcing contact was calculated as 626 kV for the arcing contact and 983 kV for the main contact at negative polarity. The decision lenght was in this case increased by 10 μm for the arcing contact and identical to the previous electrode arrangement concerning the main contact. For positive polarity arcing contact had 910 kV and the main contact 1126 kV. Although these two values differ significantly a small overlap of the breakdown probability curves was observed.

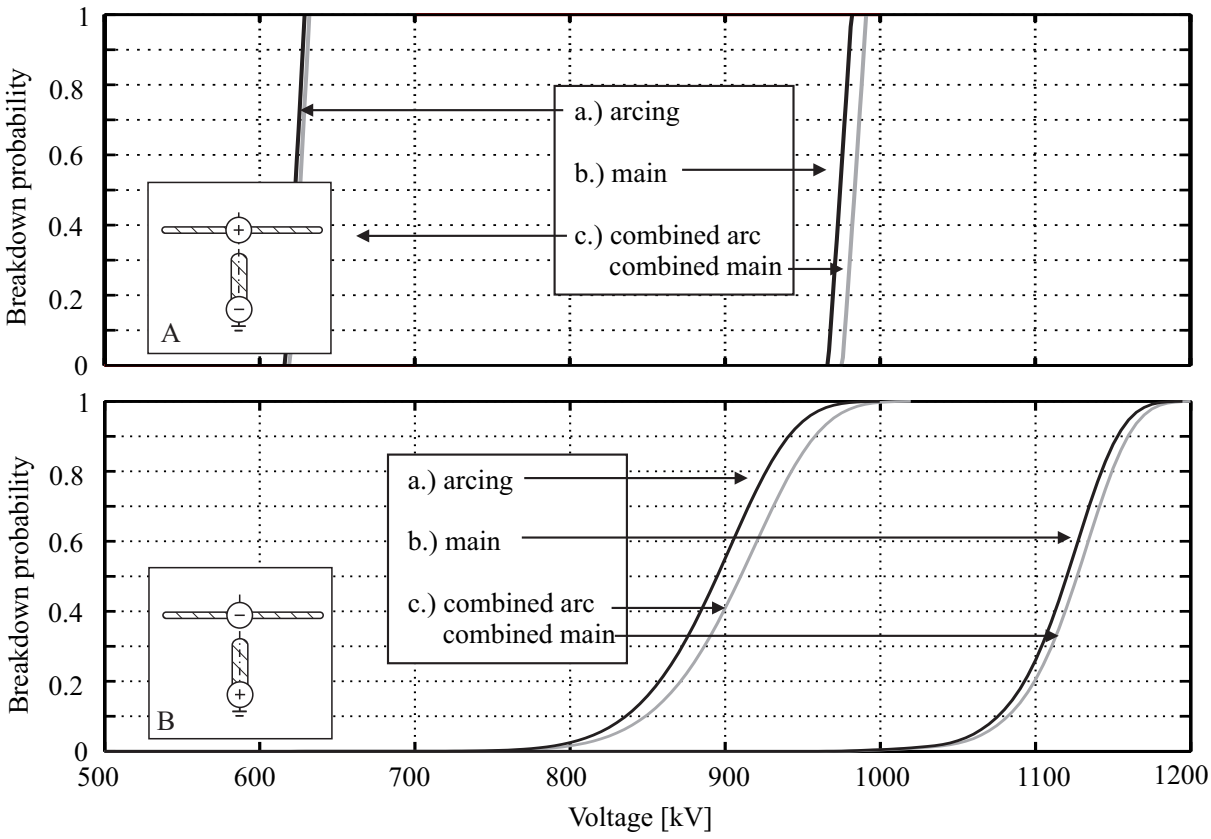

Figure 3.36.: Calculated breakdown probability curves for equal field arrangement according to Fig. 3.27

3.6. Discussion

Analysis of the breakdown statistics of different fixed side contacts vs a plane electrode with equal distance revealed a strong dependence of the breakdown probability on the polarity of the voltage applied. The 50%-breakdown voltage was generally higher when the inhomogeneous contact side was on positive potential. Breakdown voltages of opposite polarities differed most in the combined contact system (32%) followed by the arcing contact vs plane electrode arrangement (23%) and the main contact vs plane arrangement (9%). Thus, the polarity effect of the breakdown voltage was influenced by the maximum electric field and the area of the respective electrode arrangement.
The calculated breakdown voltages show a certain error compared to the measured voltages, which is likely to be explained through the surface roughness of the electrodes. All calculations were performed assuming ideal smooth electrode surfaces, which is no realistic assumption. The short decision length when calculating the streamer integral supports this hypothesis. However, the relative distance between the breakdown curve of different electrode arrangements at different polarity show the same pattern as the measured values. Consequently the polarity effect was presumably caused by first electron statistics. At negative polarity first electrons to initiate discharge are generated by electric field emission as well as collision ion detachment, whereas the process of field emission was absent at positive polarity. This hypothesis was further confirmed by the analysis of the standard deviation of the breakdown probability curves and the analysis of the time to breakdown curve. When contacts were stressed with positive polarity, the standard deviation was at least 1.1-fold increased (compared to the standard deviation of negative stressed electrodes), suggesting a dependence on first electron occurrence. Since the time to breakdown at higher breakdown voltages at negative polarity did not decrease it is reasonable to assume that the time to breakdown in this case was not influenced by first electron statistics. The minimum time for a breakdown formation, i.e. the formative time lag in this setup was approximately $1\,\mu$s.
Comparing breakdown voltages with the maximum electric field E_{max} showed an approximatively linear scale. Dependent on the polarity, the combined contact arrangement showed 21% or 29% higher breakdown voltage at 14% less E_{max} compared to the arcing contact. The main contact arrangement had 49% and 32% increased breakdown voltage at 38% decreased E_{max} compared to the arcing contact.

Experiments with the equal field setup revealed a similar dependency of the breakdown voltage, the standard deviation and the time to breakdown on the voltage polarity. The breakdown voltage at positive polarity on the combined contact system was 30% higher compared to negative polarity, being in the same range as in the equal distance arrangement (32%). The same applied for the standard deviation which was 1.95 times higher at

the positive polarity compared to 1.1 in the combined contact system with equal distance. The time to breakdown curves showed the characteristic exponential shape at negative polarity, indicating the minimum time needed to breakdown, irrespective of first electron occurrence as explained earlier.
In this case no correlation between maximum electric field and breakdown voltage could be derived. Although the electric field at the arcing contacts vs plane arrangement and at the arcing contact in the combined system are very similar, the breakdown voltage in the latter is increased by 14% and 21% dependent on the polarity applied. A similar discrepancy can be drawn from the calculated breakdown voltages: Although the maximum field of the combined system was almost identical to the single contacts, the calculated values were slightly different.

Comparing the combined contact system in both, the equal distance and equal field arrangement, the arcing contact had a 16% higher electric field at 25% less contact distance in the latter. This resulted in a reduction of the breakdown voltage of only 5% and 6% dependent on polarity. Remarkably, although the coordination factor C was 1.4 in the equal distance setup and 1.63 in the equal field setup, the breakdown probability for the nominal contacts was 23% and 0.7% respectively. The breakdown distribution on arcing and main contacts at positive polarity can presumably be explained by the volume-time law and calculation of the breakdown probability for the respective electrode, but the absolute breakdown voltage remains an unexplained finding.

In line with the previous results, the investigation of the complete contact system revealed similar characteristics. Breakdown voltage increased when the contact side with higher electric field (lower field efficiency factor) was stressed with positive polarity. A rise of the breakdown voltage of 37% and 38% was detected for 25 mm and 10 mm contact separation respectively. Time to breakdown curves showed a similar behavior as in the contact vs plane arrangements, leading to the conclusion that also in the complete contact system first electron statistics account for the polarity effect. However, opposite to the previous described results, in this experimental setup the standard deviation was decreased at positive polarity. The ratio of standard deviation is in this case 0.96 and 0.46 for 25 mm and 10 mm arrangements, respectively.
At 25 mm contact separation the maximum coordination factor on the fixed contact side was as high as 1.85 and 0.99 on the moving contact side, resulting in an overall breakdown probability of 11.6% at the main contacts. In the 10 mm arrangement the fixed contact side coordination drops to 1.81 whereas the moving contact side coordination rises to 1, resulting in a lower main contact breakdown probability of 3.5%. The strongly decreased breakdown probability of the main contacts observed in the 10 mm arrangement compared to the 25 mm contact separation presumably can be explained by differences of the

coordination factors of both contact sides. Apparently in the 10 mm arrangement the slightly elevated coordination factor on the moving contact side had a greater impact on the overall dielectric coordination than the strongly lowered coordination factor on the fixed contact side.

Taken together these results suggest:

- The breakdown voltage is lower at negative polarity on the contact side with higher inhomogeneity. The polarity effect apparently increases with decreasing field efficiency factor and decreases with increasing area of the electrode.
- Breakdown voltages of single contacts provide no sufficient means to describe breakdown probability curves of a multi-contact system even when the maximum electric fields at the individual electrodes are the same.
- A significantly higher field stress on the arcing contact does not prevent breakdowns on the main contacts. Breakdown probability distribution of the individual contacts apparently relies on the maximum electric field and on the area of the electrodes, resulting in different overlapping distributions.
- The coordination factor at the high field contact side should be at least 1.85 if the opposite contact side is not coordinated. A coordination on both contact sides seemed to decrease main contact breakdown probability.

Consequently, a possible scenario for breakdown across nominal contacts in real application can be described as follows: A closing circuit breaker misses the opportunity for pre-ignition at the instant of peak voltage with the polarity of lower breakdown strength. If the circuit breakers closing speed is big enough to decrease contact distance within one halve wave below the breakdown level of opposite polarity, a pre-ignition happens. If the contact shape and coordination in the same range as in this work, this pre-ignition happens across the main contacts with a probability of approximately 10%.

4. VFT in Circuit Breakers

In the last chapter, implicit distortion of the dielectric coordination has been investigated. This chapter focusses on possible mechanisms of an explicit distortion: the influence of very fast transient oscillations in high voltage circuit breakers. In this chapter a methodology to simulate very fast transient voltages within a circuit breaker interrupter unit is described. The method aims at identifying parameters which provoke excessive overvoltages at the breaker contacts. These parameters were identified by simulation and the influence of VFT on the breakdown behavior and the dielectric coordination was subsequently tested experimentally.

The generating source for very fast transient phenomena in circuit breakers is the same as at disconnect switch induced VFT: This is very fast arc formation and the subsequent stepwise equalization of potentials. This happens in high voltage circuit breakers as well as in disconnect switches, e.g. during closing operation (pre-ignition) and during opening after the thermal recovery phase (re-ignition or re-strike). The major difference between circuit breaker and disconnect switch induced VFT is the repetition rate of arc formation. While the latter can have several hundred arc formations during a switching operation - the circuit breaker has only one.

A pre-ignition on the arcing contacts of a circuit breaker may induce over-voltages at its main contacts, or - in the case of multi chamber breakers - overvoltages in the next interrupter unit. Overvoltages at the main contacts can increase the probability of a breakdown.

4.1. VFT Simulation Model

In this approach a model to accurately simulate traveling wave phenomena inside a high voltage circuit breaker was developed. This model incorporated all internal irregularities while its parameters are still easily adaptable. The model of the interrupter unit had to allow a simple but accurate parameter study in order to investigate the VFT development within the circuit breaker after an ignition. Moreover, the mechanism of impulse propagation in the circuit breaker and its dependency on the geometry have to be investigated. Since both requirements are difficult to achieve using 3-dimensional Finite Element Modeling (FEM) electrical field calculation, the computation of a circuit breaker model using equivalent network elements was chosen.

Due to the fast propagation of these transients, the movement of the circuit breaker contacts during a switching operation was neglected.

4.1.1. Bandwidth of Model

In contrast to the pulse propagation in GIS (section 2.3.1) the time of travel through a circuit breaker is short compared to the rise-time of impulse front. Therefore the necessary bandwidth could not be estimated using Eq. (2.17) but by the source voltage shape itself.

To determine the frequency content of the steep front potential rise, a general approach was chosen. The frequency spectrum of an exponential pulse with different rise times was calculated. Eq. (4.1) shows the analytical Fourier transformation of an exponential pulse.

$$u(t) = e^{-\frac{t}{\tau}} \quad \bullet\!\!-\!\!\circ\, U(f) = \frac{\tau}{1 + j2\pi f\tau} \tag{4.1}$$

Calculating Eq. (4.1) with different $\tau = 0.2 \ldots 2\,\text{ns}$ results in different frequency spectra, as shown in Fig. 4.1, where the amplitude of $|U(f)|$ was normalized for each curve. The 3 dB-point for the curves was in between 8 MHz and 800 MHz. This range represented the upper boundary of the necessary model bandwidth.

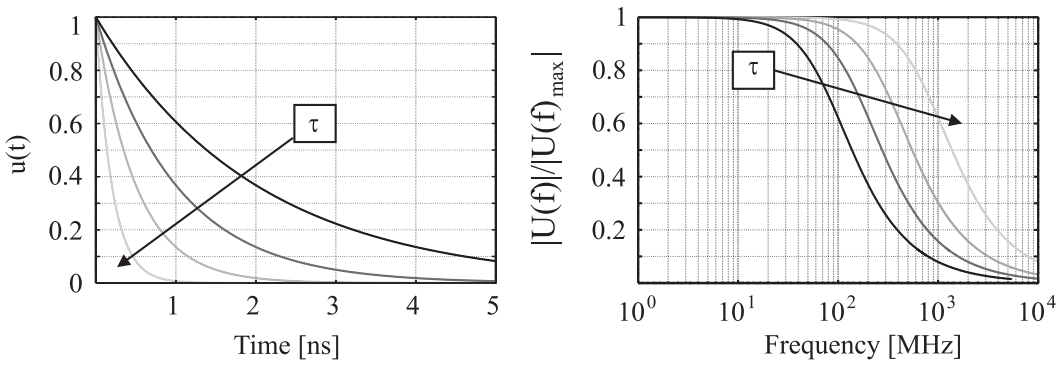

Figure 4.1.: Exponential voltage decay and corresponding norm of analytical Fourier transformation

4.1.2. Modeling Guidelines

Based on the necessary bandwidth of the model, the corresponding short wavelengths, the size of the object to model and the basic coaxial design of the circuit breaker (Fig4.2a.)), the breaker chamber was represented by pieces of transmission lines. The equations to describe potentials and currents on a certain transmission line are given by Eq. (4.2) -

(4.5), the general solutions of the telegrapher's equation by Oliver Heaviside [41].

$$\underline{V}(x) = \underline{V}_+(x)e^{-\underline{\gamma}x} + \underline{V}_-(x)e^{\underline{\gamma}x} \tag{4.2}$$

$$\underline{I}(x) = \underline{I}_+(x)e^{-\underline{\gamma}x} - \underline{I}_-(x)e^{\underline{\gamma}x} \tag{4.3}$$

$$\underline{\gamma} = \sqrt{(R' + j\omega L')(G' + j\omega C')} \tag{4.4}$$

$$\underline{Z}_w = \frac{\underline{V}_+}{\underline{I}_+} = \frac{\underline{V}_-}{\underline{I}_-} = \sqrt{\frac{R' + j\omega L'}{G' + j\omega C'}} \tag{4.5}$$

The distributed elements R', L', C' and G' (Fig. 4.2c.))represent the transmission line and can be summarized in the characteristic impedance $\underline{Z}_w$. To calculate a certain part of the circuit breaker, its characteristic impedance $\underline{Z}_w$ and its length has to be known. The calculation of this parameter is illustrated with respect to the general geometry of a coaxial line (Fig. 4.2b.)). The sizes indicated are representative measures for a high voltage circuit breaker.

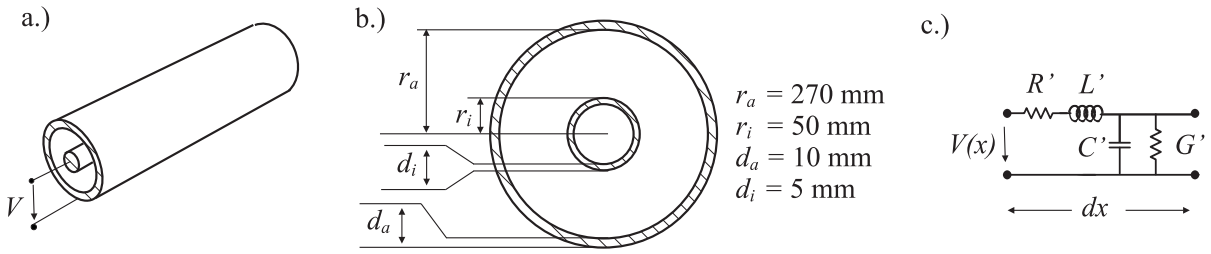

Figure 4.2.: Illustration of distributed parameters:
a.) coaxial transmission line
b.) dimensions of line, representative for circuit breaker design
c.) equivalent circuit

Resistance and Inductance

The resistance per unit length R' of the coaxial line was calculated as the sum of the resistances of the inner and outer conductor:

$$R' = R'_{in} + R'_{out} = \frac{\rho}{\pi(r_i^2 - (r_i - d_i)^2)} + \frac{\rho}{\pi((r_a + d_a)^2 - r_a^2)} \tag{4.6}$$

ρ is the specific resistivity of the material used. Due to the skin effect [41], the resistances is increased for higher frequencies. That is to say, the current is not flowing in the whole area of the conductor anymore. The skin depth can be approximated through:

$$\delta_s = \sqrt{\frac{\rho}{\pi\mu f}} \quad . \tag{4.7}$$

The skin depth is exemplarily depicted in Fig. 4.3 for different non-magnetic materials. The lower the conductivity of a certain material, the lower the skin depth. At approximately 170 Hz and 40 Hz for the inner and outer conductor respectively, the skin depth gets smaller than the diameter of the conductor (c.f. Fig. 4.2) for very good conductive materials.

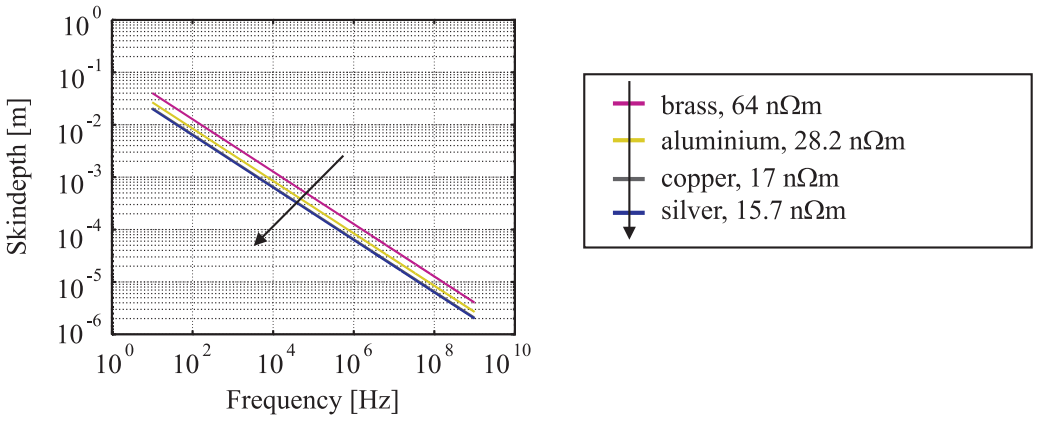

Figure 4.3.: Skin depth for different conductive materials dependent on frequency

Assuming the current flow is evenly distributed within the area formed by the skin depth, the frequency dependent resistance of the coaxial conductor was calculated as:

$$R'(f) = \sqrt{\frac{\mu\rho f}{4\pi}} \left(\frac{1}{r_i} + \frac{1}{r_a} \right) \tag{4.8}$$

For an accurate description of breakdown initiated traveling waves, the resistance of the arc would have to be considered. This resistance would be in the range of some Ω [37] and therefore exceed the resistance of the coaxial line. Hence, the resistance of the coaxial line conductors was neglected in any further calculations.

The inductance per unit length L' of the coaxial line is calculated through:

$$L' = \frac{\mu}{2\pi} \log \left(\frac{r_a}{r_i} \right) \tag{4.9}$$

The frequency dependent values for $R'(f)$ and $\omega L'$ for an aluminium coaxial line (geometry as in Fig. 4.2) are depicted in Fig. 4.4. Even for the lowest frequency of 1 kHz the influence of the inductance is 10 times higher than the resistance R' but in the same order of magnitude as the arc resistance.

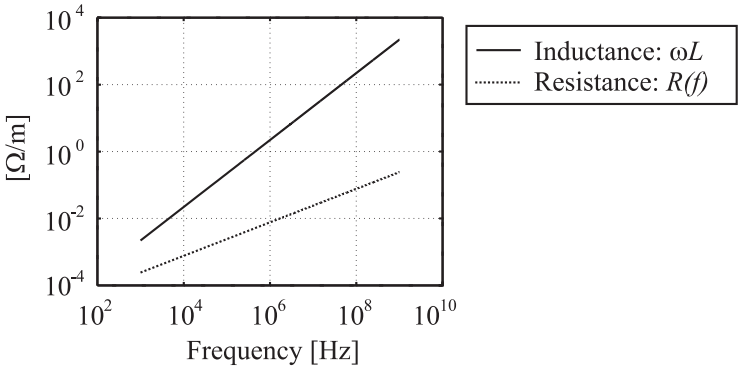

Figure 4.4.: Reactances of coaxial line (Fig. 4.2b.)) made of aluminium dependent on frequency

Conductance and Capacitance

With respect to the geometry in Fig. 4.2 the conductance per unit length G' was calculated, using the following equation:

$$G' = \frac{2\pi}{\rho \log\left(\frac{r_a}{r_i}\right)} \quad . \tag{4.10}$$

The capacitance per unit length C' is defined in a similar way, according to equation (4.11):

$$C' = \frac{2\pi\varepsilon}{\log\left(\frac{r_a}{r_i}\right)} \quad . \tag{4.11}$$

The conductivity of a gas is extremely low due to the presence of few charged particles. Consequently, the measurement of its conductivity is a rather ambitious task. In order to allow a simple comparison, a low conductivity of $\rho = 5 \cdot 10^{12}\,\Omega\mathrm{m}$ was chosen[1]. Fig. 4.5 shows the frequency dependent values of $\omega C'$ and G'. The capacitive part is the dominating one and therefore the calculation of the conductance is omitted.

Consequences for Modeling

The neglect of any damping part for the model calculation leads to real and frequency independent values of the characteristic impedance $\underline{Z}_w$ - c.f. Eq. (4.12).

The propagation value $\underline{\gamma}$ becomes purely imaginary having the meaning of a simple time delay. In this case, the propagation velocity v can be calculated using $\underline{\gamma}$. The conductive materials used for constructing a circuit breaker are generally non-magnetic ($\mu_r \approx 1$) and there are only a few non-conductive parts whereas the biggest non-conductive part is the insulating gas ($\varepsilon_r \approx 1$). Hence the propagation velocity v is equal to the speed of light

[1] This is approximately equivalent to porcelain

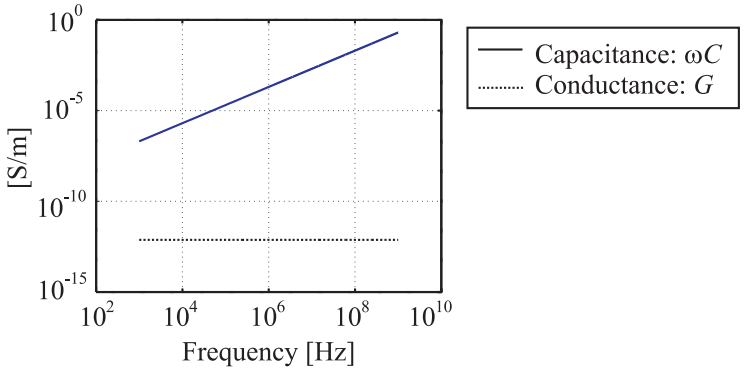

Figure 4.5.: Admittances of coaxial line (Fig. 4.2b.)) made of aluminium dependent on frequency

c_0 - c.f. Eq. (4.13).

$$Z_w = \sqrt{\frac{L'}{C'}} = \frac{1}{2\pi}\sqrt{\frac{\mu_0}{\varepsilon_0}}\log\left(\frac{r_a}{r_i}\right) \tag{4.12}$$

$$v = \frac{\omega}{|\underline{\gamma}|} = \frac{1}{\sqrt{L'C'}} = \frac{1}{\sqrt{\varepsilon_0\mu_0}} = c_0 \tag{4.13}$$

Scattering Parameters

To describe the properties of an electrical quadrupole A (Fig. 4.6) at a certain frequency it is common practice to determine the voltage at port 1, when port 2 is an open circuit and to determine the current at port 1 when port 2 is short circuited [42]. At higher frequencies it becomes difficult to define an open or short circuit, since these act more as capacitive or inductive elements.
Therefore the properties of an electrical network at higher frequencies are described by Scattering Parameters (S-Set) [43]. The S-Set describes the frequency dependent reflection coefficients of the network based on a 50 Ω load. $\underline{S}_{11}$ and $\underline{S}_{22}$ represent the input reflection factors at port 1 and port 2 respectively. $\underline{S}_{12}$ and $\underline{S}_{21}$ represent the forward reflection factor from one port to the other. Since the measured item is a completely linear, time-invariant and passive component the amplitude of the S-Parameters will always be between $1 \ldots 0$ or $0 \ldots -\infty$ dB. Furthermore, $\underline{S}_{12}$will be equal to $\underline{S}_{21}$. For reasons of clarity only the real part of $\underline{S}_{11}$ and $\underline{S}_{12}$ will be displayed here.

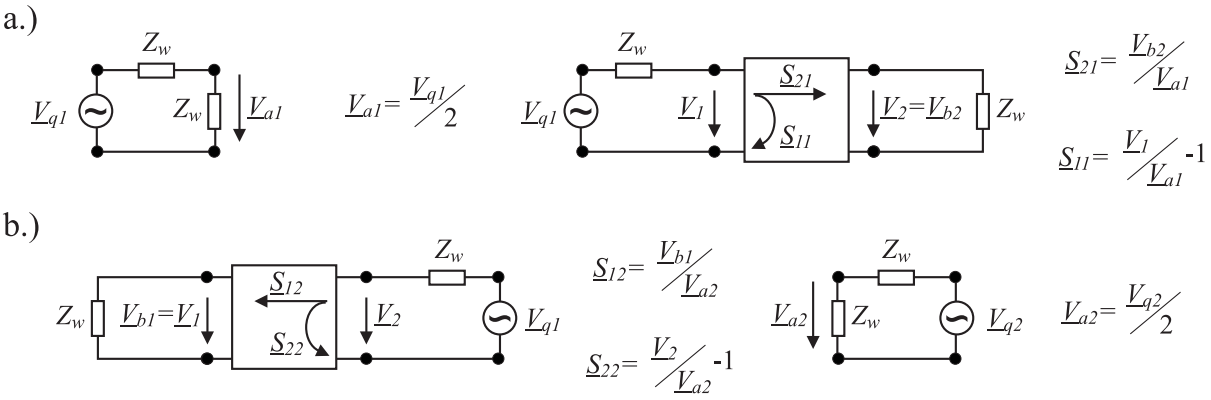

Figure 4.6.: Schematic description of S-Parameters [41]:a.) $\underline{S}_{11}$, $\underline{S}_{21}$b.) $\underline{S}_{22}$, $\underline{S}_{12}$

4.1.3. Limitation of Model

Propagation Mode

The representation of the circuit breaker as a system of concatenated transmission lines gives only an accurate image of the transversal electromagnetic wave propagation in the circuit breaker (TEM Mode). Propagation modes of higher order cannot be represented by this kind of simulation. However, due to the size of the specimen, higher electrical propagation modes can be excited as well. The first higher mode which can propagate in a coaxial system is the H_{11}-Mode and its cutoff frequency f_c is given by [41]:

$$f_c = \frac{c_0}{\lambda_c} \qquad \lambda_c \approx \frac{\pi}{\sqrt{\varepsilon_r}}(r_i + r_a) \tag{4.14}$$

Using representative dimensions from Fig. 4.2b.) the cutoff-frequency results in $f_c = 298\,\mathrm{MHz}$. By a careful setup of the experiment, the excitation of higher modes may be reduced. This can be achieved by avoiding any sharp edges in the measurement setup as these promote electromagnetic radiation.

Open and Short Circuit

Many of the coaxial conductors composing the inner structure of the circuit breaker form an open or short circuit at some specific point. These were represented in the simulation using lumped elements like inductors and capacitors. These values were estimated through geometrical consideration or electro-magnetic field calculation, but the precise value have to be validated through measurements. Therefore, these elements represented an uncertainty in the accuracy of the model.

4.1.4. Model Implementation and Calculation

The basis for the model calculation was the circuit breaker shown in Fig. 4.7. It was a SF_6 insulated, puffer type interrupter with one interrupting unit and rated voltage of 300 kV. The criterion for radial discretization was set to a relative change in surge impedance of more than 5%. The longitudinal discretization took any item into account which implied a traveling distance of more than 1 cm. It was assumed that the few non rotation-symmetric parts of the circuit breaker would not have a significant influence on the accuracy of the model. The model was implemented in Microcap9, a P-Spice based simulation tool.

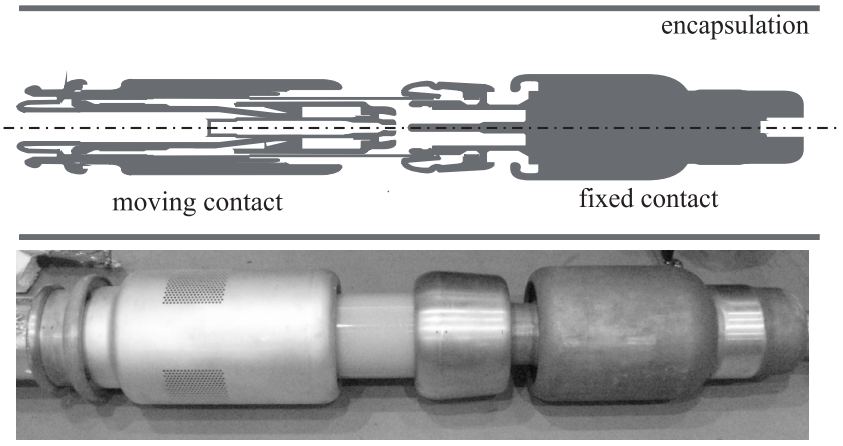

Figure 4.7.: Schematic drawing and photo of high voltage circuit breaker interrupting unit posing the basis for model calculation

Example of model calculation

The modeling procedure is explained exemplarily at the innermost item of the circuit breaker, the fixed contact, depicted in Fig. 4.8. First the analysis and discretization of the respective item was performed (Fig. 4.8a.) and b.)). The simulation program used the impedance Z_w and the time delay Δt as input values. Z_w was calculated using Eq. (4.12) and the radii r_i and r_a were obtained from the geometry. The time delay Δt was calculated using Eq. (4.13) and the length l of the item $\Delta t = l/v$. The model was implemented based on these parameters (Fig. 4.8c.)). The network elements Ai1-Ai4 represented the coaxial transmission line which was formed by the arcing contact and the inner surface of the main contact, whereas elements Aa1-Aa5 represented the coaxial transmission line formed by the outer surface of the main contact and the grounded enclosure. The main contact acts therefore as outer conductor for one transmission system and as inner conductor for the second system. The connection between the two surfaces is shown between elements Aa1 and Ai1. The non-rotation symmetric short circuit between arcing contact and

main contact after Ai3 was represented by a lumped inductance and a resistance. Since only part of an incident wave was reflected at that short circuit, the fixed contact was extended by element Ai4 which was terminated by an open circuit represented by a small capacitance.

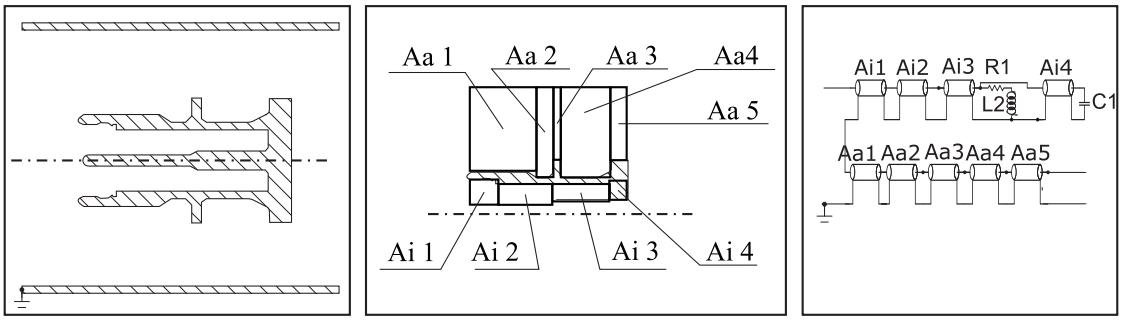

Figure 4.8.: Example for modeling procedure at the fixed contact system: a.) original geometry b.) segmented part for modelling c.) model implementation

4.2. Model Validation: Measurement and Simulation in Frequency Domain

Due to the disretization guidelines, the full circuit breaker model consisted of a large amount of elements. In order to validate the accuracy of the model, calculations were accompanied by high frequency measurements on a real circuit breaker. The validation procedure started with one small part of the breaker and the corresponding model (Fig. 4.8). Both, the hardware and software breaker were expanded stepwise, where each step was validated by comparing measurement and simulation.

4.2.1. Measurement Setup

The respective item was characterized through the measurement of the S-parameters. The measurement instrument was a vector network analyzer (VNA - Rohde&Schwarz ZVL3) with its appropriate calibration Kit (ZCAN50). Connections were made with two $50\,\Omega$ cables with N-Connectors.

The measurement of passive, distributed elements, being long compared to the electrical wavelength was a delicate task. The major difficulty was separating the influence of the connection between cable and measured object and the object itself. A non-invasive technique to provide this connection was the usage of tapered lines (Fig. 4.9). These lines provide a reflection free connection between two items of different size but equal surge

impedance by enlarging the transmission line, while keeping the ratio of inner and outer diameter constant. The surge impedance can be varied through the opening angles of inner and outer conductors according to Eq. (4.15) [44], [45]. Despite the time delay through the line, which was determined by calibration, the connection does not have an influence on the result of the measurement.

$$Z_w = \frac{1}{2\pi}\sqrt{\frac{\mu_0}{\varepsilon_0}}\log\left(\frac{\tan\frac{\upsilon_2}{2}}{\tan\frac{\upsilon_1}{2}}\right) \tag{4.15}$$

In the present case, angles of $\upsilon_1 = 6.8°$ and $\upsilon_2 = 15.6°$ were chosen to obtain an impedance of $Z_w = 50.09\Omega$. Although this is a ell established technique, the production of these connections in an accurate way is difficult and expensive. The construction of these lines to match the GIS-equipment in Tab. 3.1 was divided in two parts: The first part of the tapered line which was attached to the 50Ω cable is especially sensitive to imprecisions in design due to the small distances between the conductors. This part was manufactured

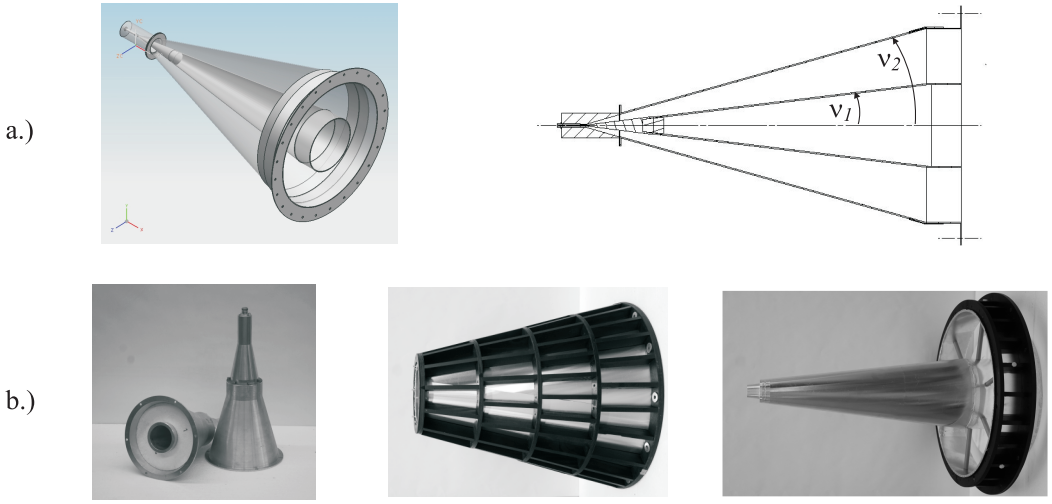

Figure 4.9.: Schematic drawings and photo of constructed tapered lines for high frequency measurements with opening angles υ_1 and υ_2 defining the surge impedance of the line

using a lathe. For the second part, with a lower absolute precision requirement, a wooden frame was used to provide the necessary shape and mechanical stability. It was covered with an 0.8 mm thick aluminium sheet which could be easily bent into the desired shape. The final setup is displayed in Fig. 4.10. Further experimental experience to achieve proper results of high frequency measurements are summarized as follows:

- Any connection shall be firm and give a low resistive connection. An incomplete connection will act as a capacitive element which is in the same order of magnitude as the items under investigation.

- Discontinuities or gaps in the conductive system manifest at higher frequencies. Their influence can be minimized through a cover of conductive tape.

- Commercial low density styrofoam is a convenient material to support the inner conductor or the measurement object. It has very low influence on the measurement result.

- Connections between tapered lines and object of measurement should be done through cone-shaped conductors (c.f. Fig. 4.10b.) and Fig. 4.11). Discrete radius adaptations cause discontinuities in the measurement results. According to Eq. 4.12 these cones manifest a logarithmic change in surge impedance which cannot be implemented accurately in the model. The cone had to be laterally discretized and represented as stepwise change in surge impedance (c.f. conical connector in Fig. 4.10). Best results were achieved by discretizing the cone into steps with constant change in surge impedance and variable time delay for each element.

a.) 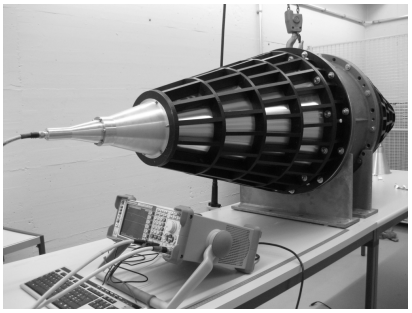 b.) 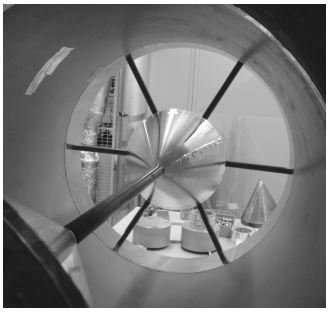

Figure 4.10.: High frequency measurement setup:
a.) Vector Network Analyzer (VNA), cables and tapered line
b.) Joint of inner conductor using cone shaped interconnectors

An example of such a measurement is schematically depicted in Fig. 4.11. Measurement device, cable and tapered lines are shown as well as the conical connection and the actual object of interest, the fixed contact part of the circuit breaker.

4.2.2. Comparison of Simulation and Measurement

Circuit Breaker

The measurement of the S-parameters according to Fig. 4.11a.) was compared to the simulation of the S-parameters according to Fig. 4.11b.) and both are shown in Fig. 4.12. Measured and simulated parameters showed a similar behavior up to a frequency of approximately 520 MHz.

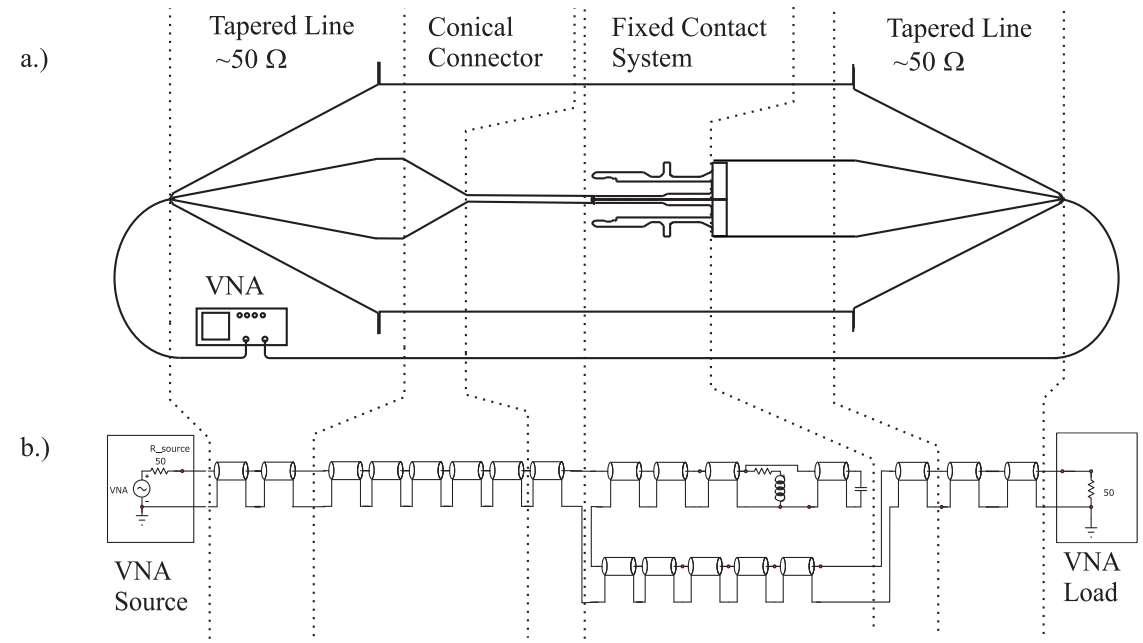

Figure 4.11.: High frequency measurement setup for the fixed contact part of the circuit breaker. Schematic drawing of setup (top) and corresponding implementation in the model (bottom)

Comparison of this kind were made for all individual parts of the breaker: fixed contact, fixed contact with shield, moving contact, moving contact with shield, adjacent connections and full circuit breaker in closed and open position. The model lost accuracy with increasing number of elements. The comparison of the fully assembled circuit breaker in closed position is shown in Fig. 4.13. For the full circuit breaker there was a fair consistency between simulation and measurement up to 450 MHz.

Conclusively, the calculation of a transmission-line model gave an accurate representation of the high frequency behavior of the circuit breaker. Even though it consisted of several concatenated coaxial systems, comparison between measurement and simulation showed acceptable agreement.

The comparisons in Fig. 4.12 and Fig. 4.13 illustrate that a frequency of 500 MHz represents the upper boundary for experimental setups with reasonable effort.

Grading Capacitors

When a circuit breaker consists of two or more interrupting units in series, grading capacitors are usually installed in parallel to the interrupting unit in order to provide equal voltage distribution between the respective units. Their integration into the circuit breaker model is difficult for two reasons: Firstly, these elements are not straight conductors but sandwich structures of conductors and insulating media. Therefore, the inner structure of the grading capacitor can not be modeled by coaxial transmission lines.

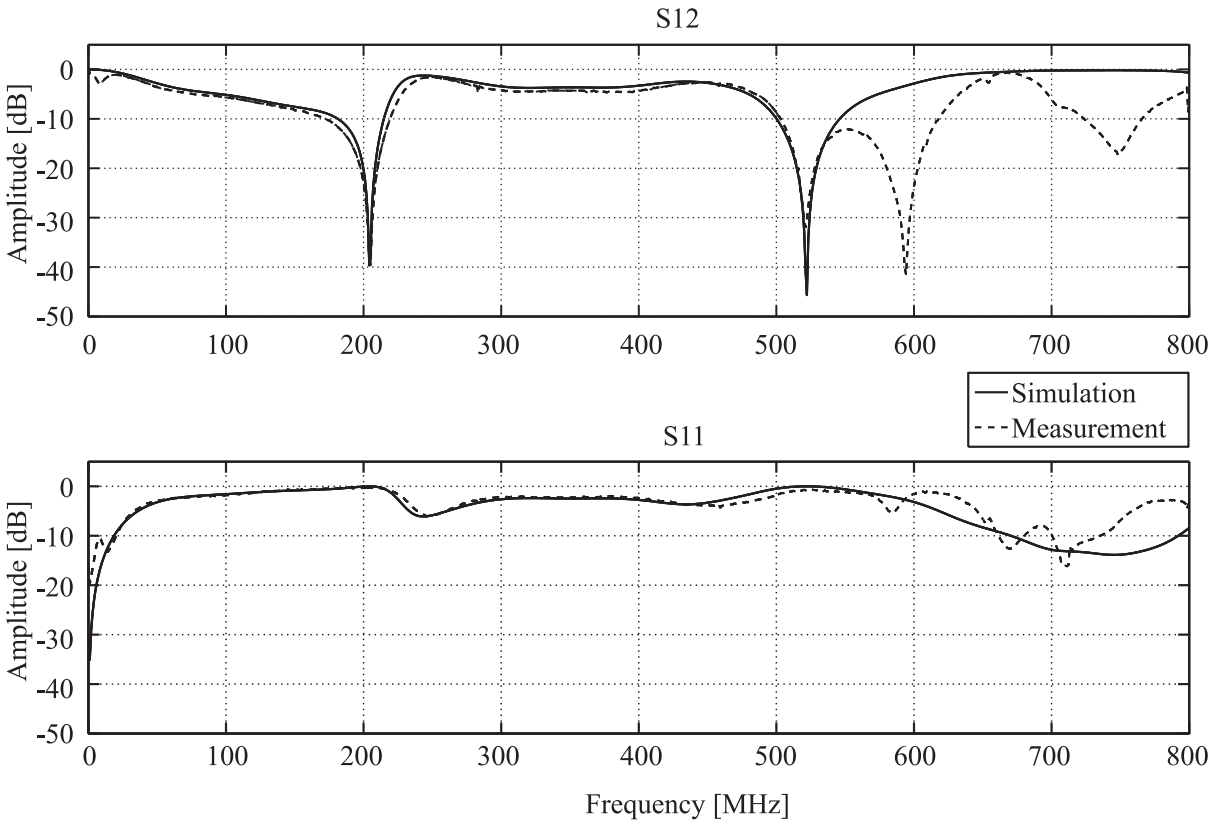

Figure 4.12.: Comparison of measured and simulated S-parameters of the fixed contact system according to Fig. 4.11 shows acceptable agreement up to approximately 500 MHz

Secondly, grading capacitors are not aligned rotationally symmetric within the enclosure.

Thus, in order to describe their high frequency behavior different capacitors were measured. The characterization of a 700 pF capacitor is exemplarily described here. Fig. 4.14 shows a picture of the experimental setup, used to describe the behavior of the capacitor itself, i.e. as straight line conductor and its corresponding representation as lumped circuit.

The comparison of measured an simulated S-parameters is shown in Fig. 4.15. The model of the capacitor, consisting of lumped elements representated the capacitor up to a frequency of approximately 120 MHz accurately. Above this frequency effects arose which could not be reproduced neither by using lumped nor by distributed elements. In the measured curve of the S_{12}-parameter the main influencing parameters of the grading capacitor could be identified: The initial rise was proportional to the capacity ($C1$ in Fig. 4.14), whereas the following straight line was characteristic for the capacitors forward resistance ($R1$ in Fig. 4.14). The decay of the curve after approximately 160 MHz was roughly described by the inductance $L1$ in Fig. 4.14.

In order to quantify the influence of a non-rotation symmetric aligned grading ca-

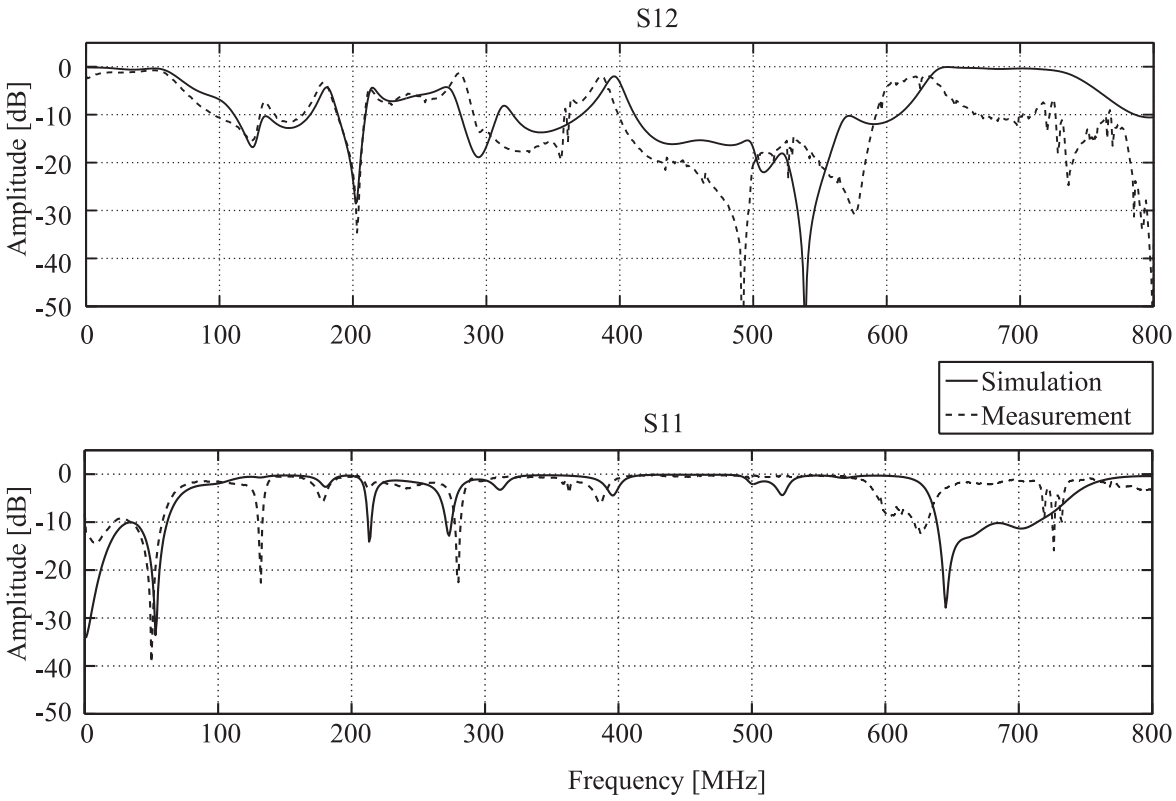

Figure 4.13.: Comparison of measured and simulated S-parameters of the complete circuit breaker according to Fig. 4.7 in closed position shows acceptable agreement up to approximately 450 MHz

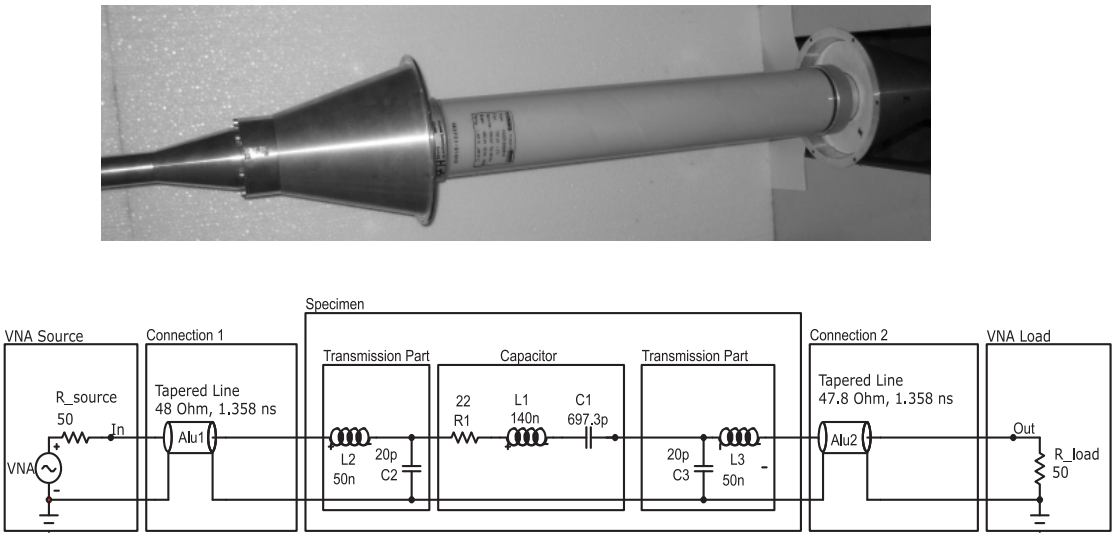

Figure 4.14.: Measurement setup no.1 for high frequency characterization of a grading capacitor. Photo of the experimental setup (top - without enclosing pipe) and corresponding representation of the capacitor in the model

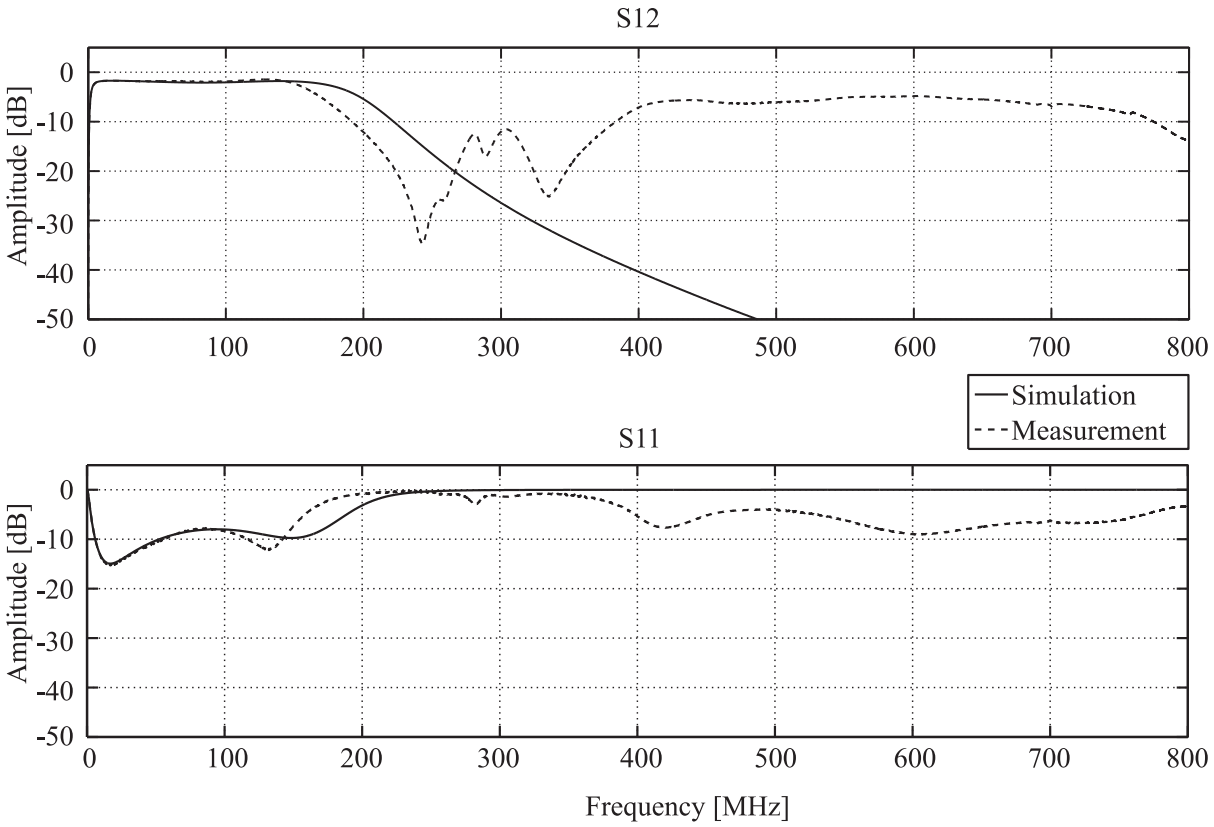

Figure 4.15.: High frequency measurement and simulation of grading capacitor according to experimental setup in Fig. 4.14 shows a fair agreement up to 120 MHz

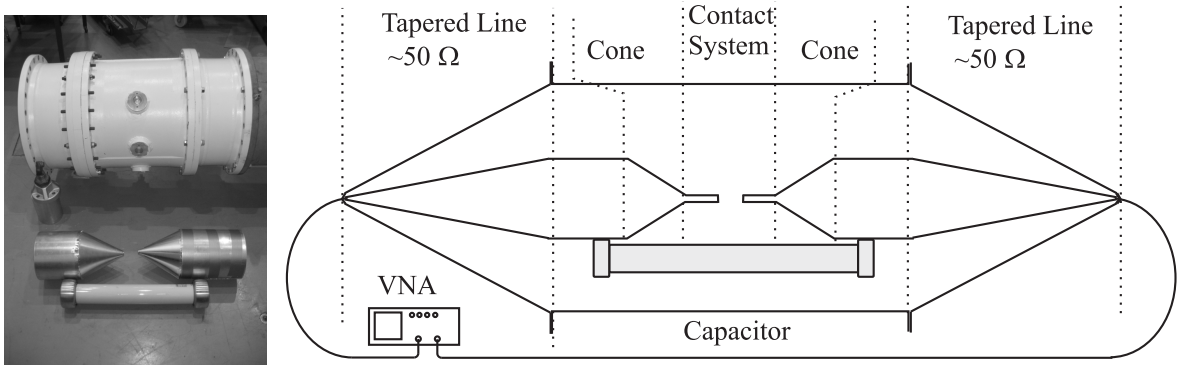

Figure 4.16.: Measurement setup no.2 for high frequency characterization of a grading capacitor and its influence on a transmission line system. Photo of the experimental setup (left) and schematic drawing of the whole measurement setup

pacitor, a measurement parallel to a coaxial line was performed (c.f. Fig. 4.16). This setup was measured with and without capacitor installed and should reveal, whether the grading capacitors have an influence on the transmission behavior of the circuit breaker.

The measurements of the setup with and without grading capacitors are shown in Fig. 4.17. The measurement representing the pure transmission line showed a clear capacitive behavior up to a frequency of approximately 650 MHz. This was mainly determined by the stray capacitance between the two tips of the contact system (c.f. Fig. 4.16). Above 650 MHz significant losses through the excitation of higher modes occurred. The measurement including the grading capacitor showed very similar behavior as in the previous measurement (c.f. Fig. 4.15). Noteworthy the measured curves are very similar between approximately 195 to 220 MHz. In this frequency range the grading capacitor did not affect the transmission system.

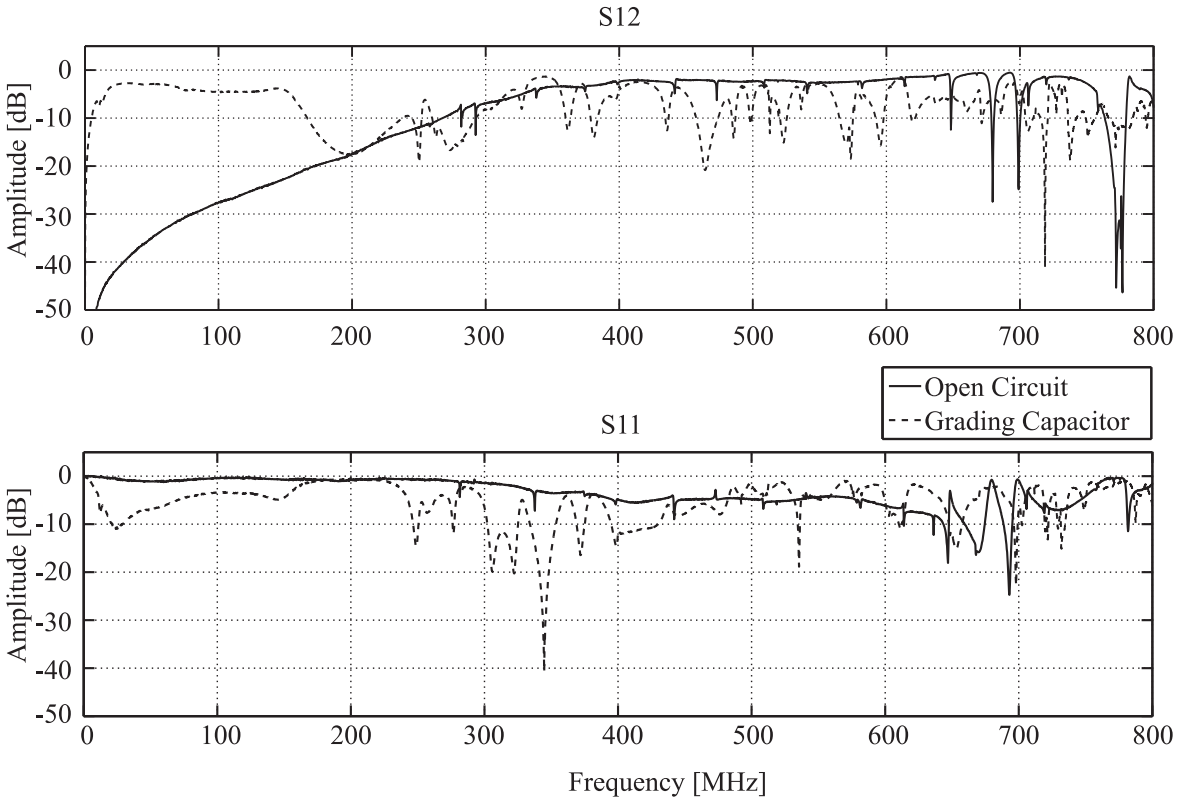

Figure 4.17.: Measurement of S-parameters according to experimental setup in Fig. 4.16. The solid line shows the measurement without capacitor (open circuit) and the dotted line the measurement with built in grading capacitor. The high frequency behavior of the two setups is identical at approximately 200 MHz

4.3. Model Application: Simulations in Time Domain

In order to investigate the development of VFT within the circuit breaker unit and to analyze the potential distribution in the breaker, the implemented and validated model was used for transient simulations.

4.3.1. Single Unit Interrupter

The circuit breaker model as in Fig. 4.18 was expanded with two connecting lines, a voltage source (1 V) and a load resistor having the same surge impedance as the connecting line. In this simulation the voltage development across the main contacts, excited by a breakdown across the arcing contacts was studied.

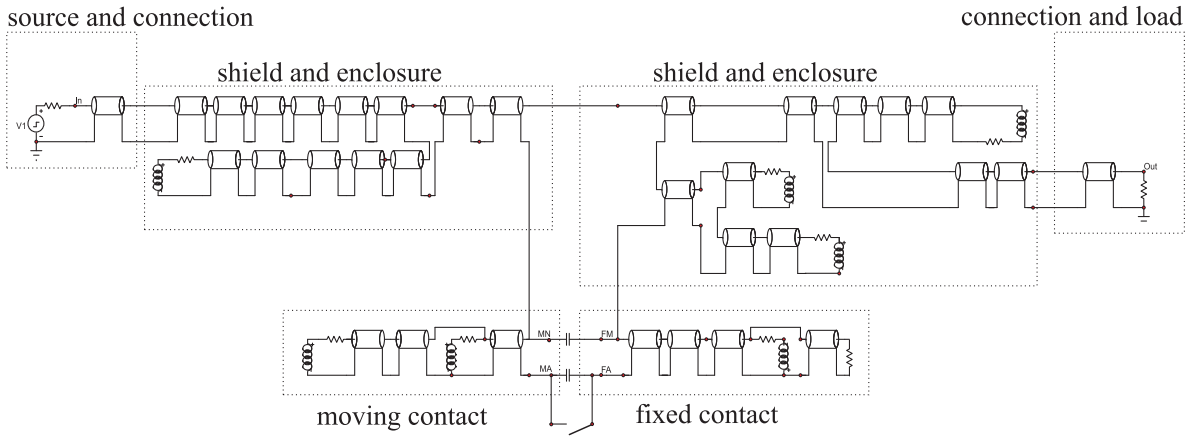

Figure 4.18.: Complete model of high voltage circuit breaker as used for simulation of transient voltages within the switching unit

The breakdown was modeled as infinitely fast switching action. Arc resistance and inductance were neglected in order to get a worst case observation. An example of such a simulation is shown in Fig. 4.19a.). The voltage across the arcing contact dropped instantaneously from one to zero, while the voltage across the main contacts followed with a high frequency oscillation.
This high frequency oscillation was investigated with respect to the influence of the following parameters:

- Short circuit connection between arcing and main contacts
- Inner length of arcing contacts
- Further network elements (source and connection/connection and load in Fig. 4.18

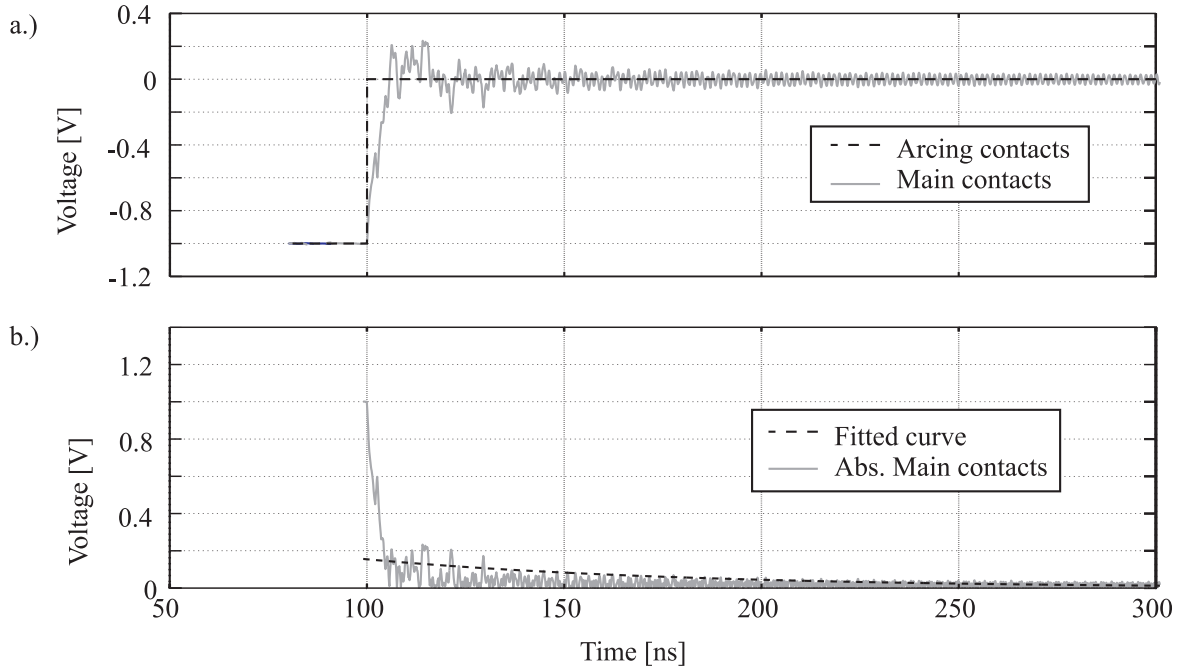

Figure 4.19.: Example of transient simulation:
a.) Pre-ignition across the arcing contacts and subsequent transient voltage across the main contacts
b.) Absolute value of transient voltage across main contacts and fitted curve used to quantify the severity of the transient voltage

A breakdown in a gas insulated electrode arrangement is the consequence of a voltage drop of certain amplitude and duration across these electrodes. The severity of the transient voltage shape as exemplarily depicted in Fig. 4.19a.) is therefore quantified by its amplitude and duration. To get a comparable number out of the transient simulation the factor Q was introduced. Q was calculated by the multiplication of maximum amplitude V_{max} and decay time Δt till 10% of V_{max} of the transient voltage. V_{max} and Δt were calculated out of the fitted absolute value of the transient simulation by an exponentially decaying voltage drop, c.f. Fig. 4.19b.). Since the initial drop of the transient voltage is always the same irrespective of simulation parameters the transient voltage was fitted by a simple exponential function. Therefore, the fit was a representative description for the duration and amplitude of the transient simulation without overrating its initial value.

In Fig. 4.20 the parameter Q (norm) is exemplarily plotted across the value of the inductive connection between arcing and main contact on the moving and fixed contact side respectively (c.f. inductive elements in Fig. 4.18 at moving and fixed contact). In this specific case 100 parameter combinations were tested and evaluated.

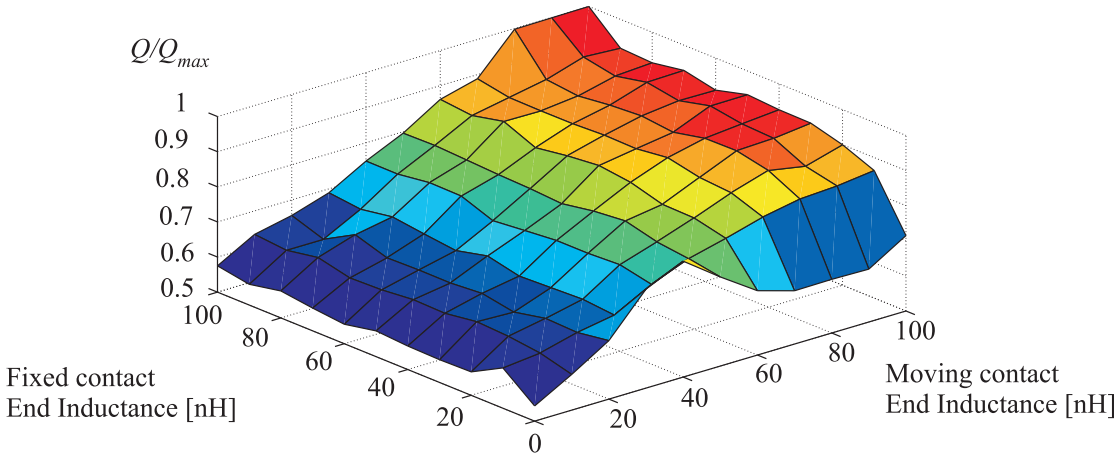

Figure 4.20.: Illustration of the analysis of the influence of different inductances forming the connection between main and arcing contact on moving and fixed contact side. The factor Q determines the severity of the VFT and grows with rising inductance

4.3.2. Double Unit Interrupter

For the investigation of traveling waves within a double unit or two chamber breaker, a series connection of two models for a single unit interrupter was used. The analysis followed a different path than in the single unit interrupter. Under the assumption that the effects of potential differences between arcing and nominal contacts were based on the same rules as before, the focus in this case was more on the exciting source.

The source in this case was a pre-ignition in one interrupting unit, inducing high frequency oscillations in the second one. The ignition itself was modeled the same way as described in section 4.3.1. Since the connection of the two interrupting units was only one coaxial line, no major oscillations were expected.

Assuming two transmission lines as in Fig. 2.9, having the same surge impedance and a potential drop of 1 pu in between them, a breakdown would lead to -0.5 pu pulse traveling towards the source and 0.5 pu pulse traveling towards the load. The ratio of the split-up is determined by the ratio of the characteristic impedances of the respective lines.
In order to receive a high amplitude oscillation within a double unit circuit breaker, the initial step must be as high as possible. Consequently, the source side must have a low characteristic impedance and the load side a high impedance.

4.4. Results of VFT Simulations

4.4.1. Single Unit Interrupter

Systematic investigation with parameter variations were performed similar to the example shown in section 4.3.1. The main criteria influencing a high frequency oscillation across the main contacts, excited by a breakdown at the arcing contacts could be summarized as follows:

- The weaker the short circuit connection between main and arcing contact, the more severe the VFT at the main contacts was . Weak in this respect refers to a connection with higher inductance.

- VFT at main contacts increased with increasing length and surge impedance of the coaxial line formed by the arcing and main contacts.

- The influence of the network connection of the circuit breaker manifested whenever there was a mismatch between connecting line and load impedance. Maximum amplitude was higher for a big mismatch irrespective of the actual value, whereas the decay-time was higher for a low mismatch. Therefore, the two effects compensated each other. One of the parameters could become important depending on whether the amplitude of very fast transient voltages or its duration impact the dielectric strength of SF_6 more.

- The introduction of lumped capacitors on either side of the circuit breaker have the biggest impact. VFT were favored through capacitors with opposite sizes, e.g. small capacitor on source side and big capacitor on load side.

Fig. 4.21 shows an example of a transient simulation which can be viewed as worstcase scenario. This was obtained by implementing moving and fixed side contacts as coaxial conductors with equal length and characteristic impedance ($Z_w = 180\Omega, l = 1$ m) terminated with a big inductor ($L = 100$ nH) and with a low capacitive source (0.5 nF) and a high capacitive load (3 nF).

In Fig. 4.21 the voltage drops across arcing and main contacts are depicted. Due to the pre-ignition simulated, the voltage across the arcing contacts dropped instantaneously from 1 V to 0 V at 1 μs. Consequently, the voltage across the main contacts decayed to 0 V as well but within a longer time frame ($> 3\,\mu$s) and with an oscillation around zero with very high frequency. The peak voltages of the transient oscillation reached -0.7 V and +0.5 V respectively.

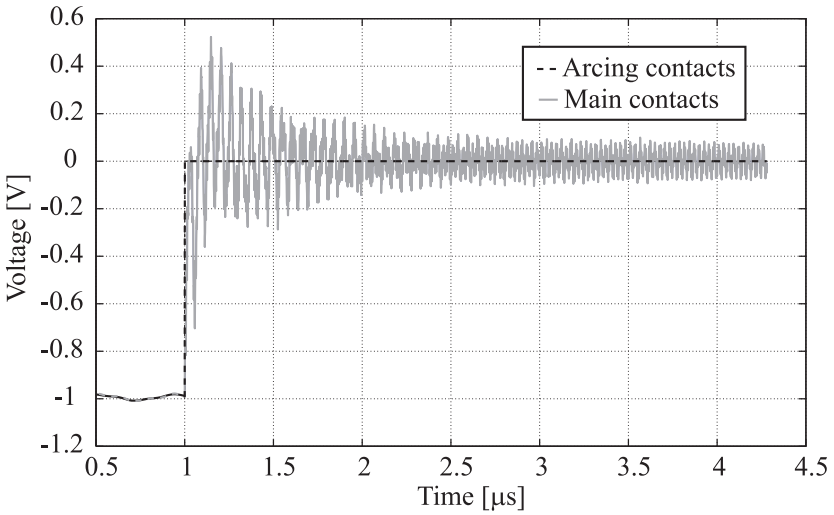

Figure 4.21.: Single unit interrupter: Transient voltage across main contacts during pre-ignition on arcing contacts reaching a peak value of 0.5 V

4.4.2. Double Unit Interrupter

Concerning the inner structure of the circuit breaker, simulations using the double unit model revealed equal trends in the development of VFT across main contacts in one chamber when excited through a pre-ignition in an adjacent chamber. However, VFT provoking adjacent elements were in this case a low impedance source and a high impedance load. The simulation in Fig. 4.22 shows the transient voltage across main and arcing contacts of a switching unit excited through the breakdown in an adjacent unit with a source side capacitor of (3 nF)[2] and a load side impedance of (350 Ω). Despite the adjacent elements, the simulation was performed with the identical parameters as in the previous section, only the circuit breaker was doubled.

Noteworthy, the initial value of the transient simulation in Fig. 4.22 is around 0.1 V. The initial voltage drop was the result of different stray capacitances within the breaker which determined the static voltage distribution before the pre-ignition event occured. At time 1 μs the switching of one interrupting unit occurred and caused a transient oscillation across the still insulating interrupting unit. This oscillation is of similar duration as in Fig. 4.21 but its amplitude is significantly higher. Values of 1.65 V were reached.

Although the lumped equivalent circuit representing a grading capacitor (c.f. Fig. 4.16) was only accurate in a small frequency range, it was used to simulate the transient voltage development in a double unit circuit breaker after pre-ignition at one contact side. The parameters of the simulation remained unchanged except for the addition of the grading capacitors. The result is shown in Fig. 4.23. In this case the initial amplitude of transient

[2]The capacitor represents a voltage source with low impedance with respect to VFT

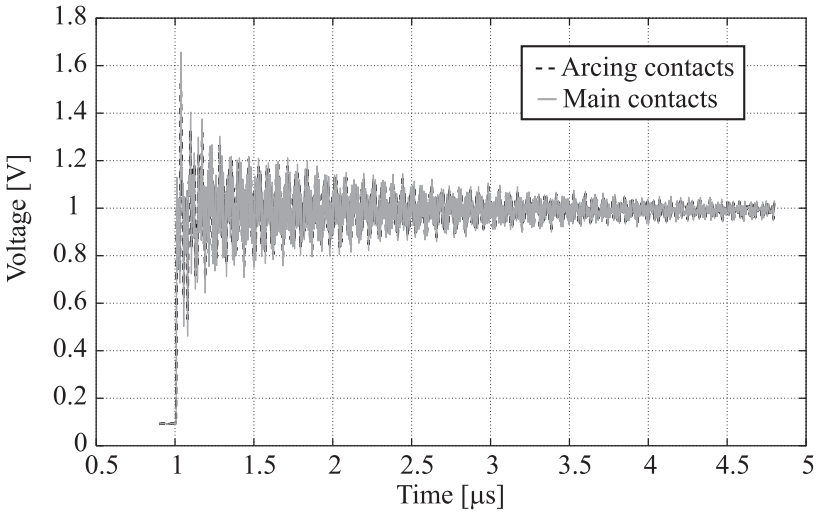

Figure 4.22.: Double unit interrupter: Transient voltage across main and arcing contacts during pre-ignition in adjacent chamber reaching a value of approximately 1.65 V

simulation was 0.5 V representing the desired effect of grading capacitors to get an even voltage distribution between the two interrupting units. The amplitude and duration of the transient voltage was much smaller than in the previous simulation, but the amplitude was still exceeding 1 V.

Noteworthy both simulations, Fig. 4.22 and Fig. 4.23 did not show significant differences between transient voltages across main and arcing contacts.

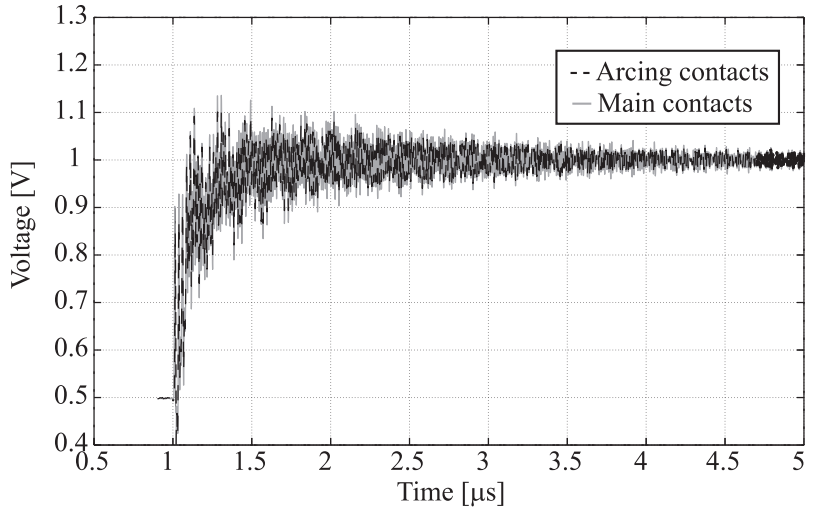

Figure 4.23.: Simulation of transient voltage in double unit interrupter with grading capacitors reaching a value of approximately 1.11 V

4.5. Measurement of Breakdown Probability Distribution with VFT

In order to investigate whether the transient distortion of potential and electric field distribution do have an effect on the breakdown behavior of the contact system, breakdown experiments were carried out using the experimental setup and method of investigation described in section 3.2.

4.5.1. Single Unit Interrupter

In order to provoke the formation of VFT at the main contacts, the experimental setup was modified. Changes were made at the contact system and the load side guided by simulation results of section 4.4.1 to maximize the amplitude and duration of transient potential differences between the contacts. The solid connection between arcing and main contacts on both sides was replaced by a thin wire in order to simulate a high inductive connection (Fig. 4.24). Further, the limiting resistor on the load side of the experimental setup was supplemented with a load capacitor with $C_l = 1.98\,\mathrm{nF}$.

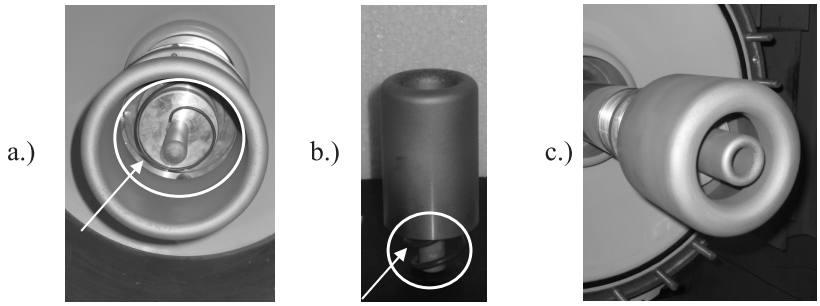

Figure 4.24.: Manipulation of contact system by introducing a high inductive connection between arcing and main contacts to provoke VFT in test vessel

A simulation of the whole experimental setup was implemented in order to estimate the VFT voltage occurring at the main contacts of the specimen after the pre-ignition across the arcing contacts. The lightning impulse voltage applied in the simulation was set to 1 V and the (ideal) breakdown at the arcing contacts happened at $t = 1\,\mu\mathrm{s}$. The simulated voltages across the contacts are shown in Fig. 4.25. The arcing contact voltage dropped instantaneously to zero whereas the main contact voltage shows a high frequency oscillation with peak amplitude of 0.2 V and approximately $4\,\mu\mathrm{s}$ duration.

A slight misalignment occurred during the installation of the electrodes. The arcing contact on the moving contact side was shifted from the rotation axis resulting in a contact separation of 11.1 mm at one side and 12.9 mm on the other side. This resulted in a change of electric field values on the contacts. The field on the main contacts was

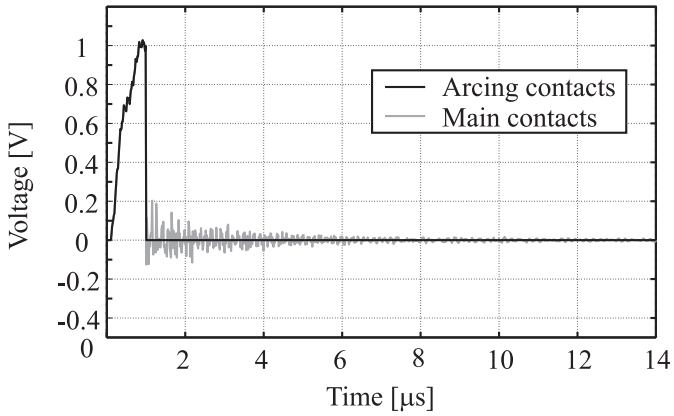

Figure 4.25.: Simulated voltages across main and arcing contacts in experimental setup

unaffected by the change in arcing contact alignment but the electric fields on the arcing contacts were increased. The maximum electric field values are summarized in Tab. 4.1.

Table 4.1.: Electric field values for complete contact system, 10 mm gap distance and decreased arcing contact distance

	C	fixed arc	fixed main	moving arc	moving main	C
E_{max} [V/m]	1.83	129.2	70.5	76.5	74.3	1.03

The results of the breakdown experiments are depicted in Fig. 4.26. For comparison, the breakdown probability distribution of the full contact arrangement with 10 mm contact separation (c.f. Fig. 3.31) stressed with Lightning Impulse voltage are shown as well. When the polarity of the applied Lightning Impulse voltage was negative on the modified fixed contact side (A in Fig. 3.31) the 50%-breakdown voltage was $V_{BD-50} = 376\,\text{kV}$ with a standard deviation of $\sigma = 14.7\,\text{kV}$ (c.f. Fig. 4.26). At the positive polarity (B) the breakdown voltage was $V_{BD-50} = 448\,\text{kV}$ and $\sigma = 30\,\text{kV}$. Therefore in the modified arrangement the breakdown voltage was 13% and 31% smaller than in the full contact arrangement according to Fig. 3.32)b.).

However, during 417 experiments with (A) and 396 experiments on (B) polarity according to Fig. 3.31, no breakdowns on the main contacts were detected.

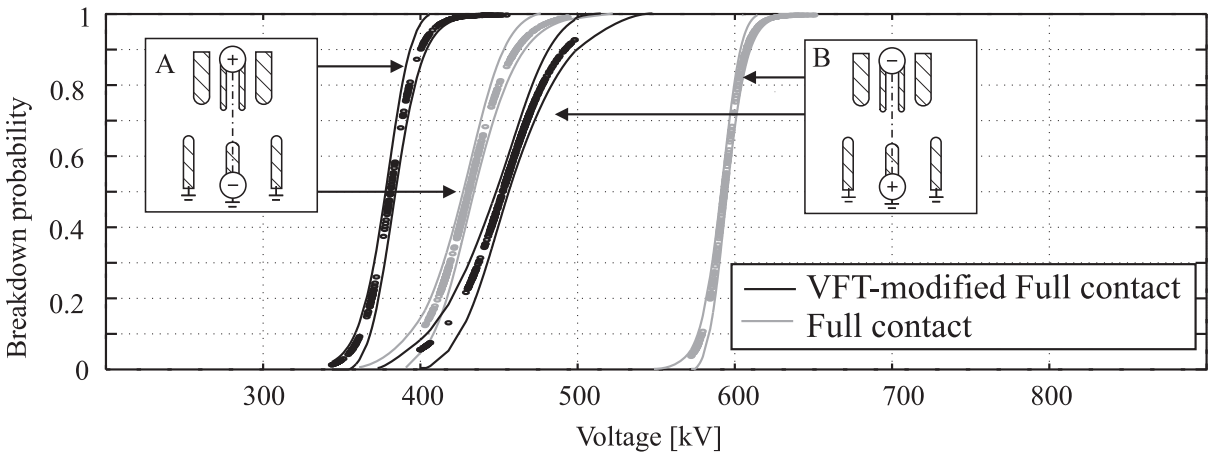

Figure 4.26.: Breakdown probability curves of modified setup and normal setup according to Fig. 3.31 tested with positive and negative Lightning Impulse voltage.

4.5.2. Double Unit Interrupter

To analyze the impact of VFT as occurring in a double unit interrupter, the same contact arrangement was used as in the experiments described in section 3.4.3 having contact separation of 10 mm. The experimental setup of chapter 3.2 was used, whereas the disconnector on the source side was slightly opened before each voltage application. Hence a pre-ignition occurred in the disconnector and consequently a VFT was applied onto the contact system similar to what would occur in a two chamber circuit breaker. No further changes of the experimental setup were made, since the capacitive source side and the resistive load side already represent the worst case scenario for traveling waves as derived in section 4.3.2.

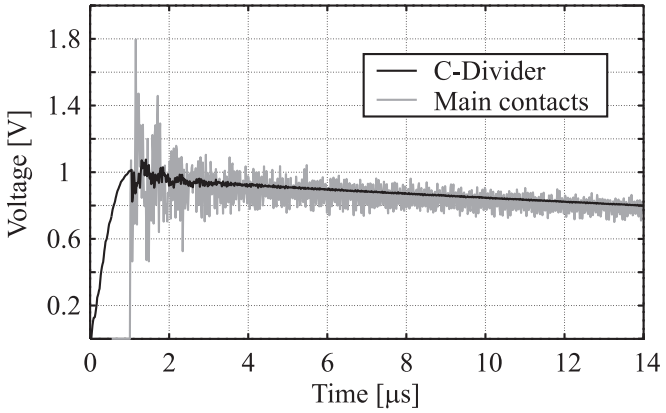

Figure 4.27.: Simulated voltage in experimental setup caused by a pre-ignition across the disconnector on the source side (c.f. Fig. 3.4): simulated voltage as measured by capacitive voltage divider and across main contacts of specimen

A simulation of the whole experimental setup was implemented in order to estimate the amplitude and duration of the VFT voltage stressing the contact system after the pre-ignition of the disconnector. The simulated voltages presumably occurring at the capacitive voltage divider and across the main contacts of the specimen are depicted in Fig. 4.27. In the simulation, the Marx generator was charged to a voltage level of 1 V and the pre-ignition at the disconnector happened at $t = 1\,\mu$s. The simulated voltage across the voltage divider (Fig. 4.27) consisted of two components: the lightning impulse voltage shape as produced by the Marx generator and the superimposed VFT voltage triggered by the pre-ignition of the disconnector. The resulting transient oscillation across the main contacts of the contact system lasted several μs and its amplitude was as high as 1.8 V. The voltage drop across the arcing contact is not shown, since no significant difference to the main contact voltage could be detected.

A measurement example of the corresponding voltage shape is shown in Fig. 4.28. Two different breakdowns are clearly visible: The first at approximately about 1.2 μs

representing the pre-iginition across the gap of the disconnector, whereas the second breakdown at 1.9 μs indicated the breakdown in the circuit breaker contact system.

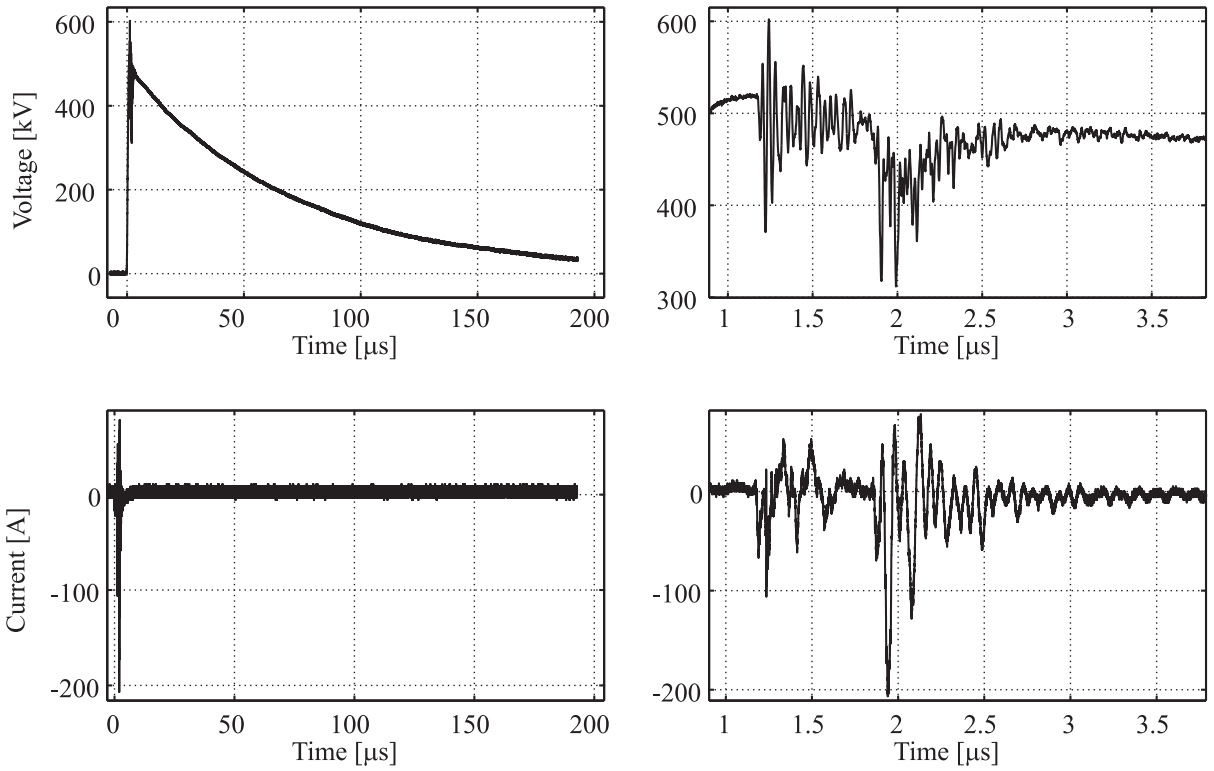

Figure 4.28.: Measured voltage and current forms imitating VFT in a double unit interrupter recorded by experimental setup according to Fig. 3.4

The results of this experimental series are shown in Fig. 4.29. Voltages were calculated as in the previous measurements by determining the peak voltage of the measured voltage (c.f. Fig. 4.28). Therefore, the breakdown voltages displayed 'VFT' in Fig. 4.29 is based on a lightning impulse voltage with much smaller amplitude. In order to allow a comparison, the breakdown probability distributions of the fullcontact arrangement with 10 mm contact separation (c.f. Fig. 3.31) are shown as well. If the voltage at the fixed contact side had a negative polarity (A), the breakdown voltage was $V_{BD-50} = 394\,\text{kV}$ with a standard deviation of $\sigma = 14.9\,\text{kV}$. At the opposite polarity (B) V_{BD-50} was 574 kV with a standard deviation of $\sigma = 15.8\,\text{kV}$. This is a reduction in breakdown voltage of 8% and 2% towards the same contact system tested with lightning impulse voltage only.

All the experiments executed with negative polarity at the arcing contacts showed 100% breakdown occurrence on the arcing contacts. Remarkably the analysis of arc base points at the opposite polarity showed a different distribution than in Fig. 3.33b.). The voltage application with positive polarity on the fixed contact side showed a large number of breakdowns at the main contacts (c.f. Fig. 4.30). Out of 160 experiments, 28 breakdowns occurred on the arcing contacts (31%) and 63 on the main contacts (69%).

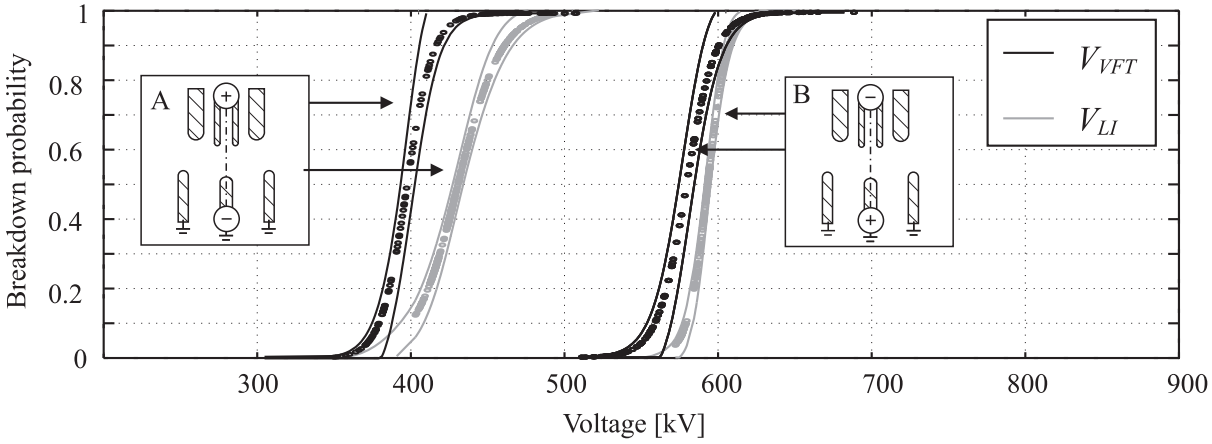

Figure 4.29.: Breakdown probability curves of full contact system stressed with Lightning Impulse and VFT superimposed on Lightning Impulse according to Fig. 4.28 imitating VFT in a double unit interrupter

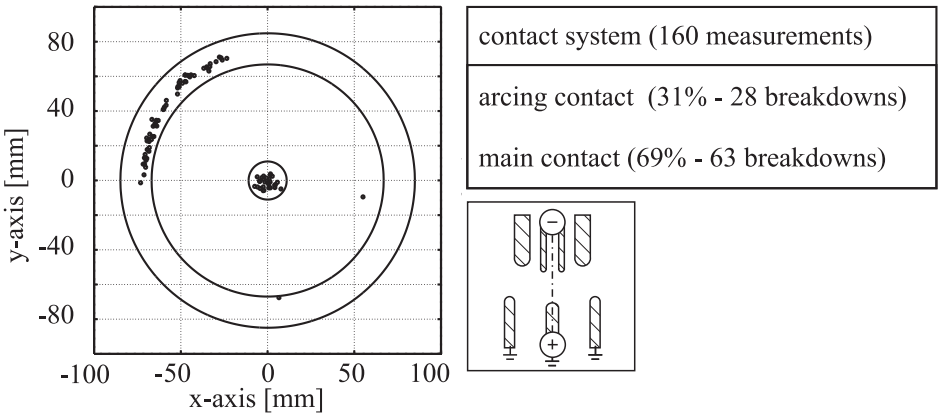

Figure 4.30.: Breakdown distribution on main and arcing contact of complete contact system (Fig. 3.31b.)) when stressed with VFT voltage according to Fig. 4.28

A clustering of arc root points was visible on the moving contact side, covering about a quarter of the electrode. It was assumed that a significant change in surface roughness was not responsible for this finding. Since these experiments were executed directly after the ones described in section 3.4.3 the reasons for the clustering are likely to be the same. Characteristic breakdown pictures recorded during this series are shown in Fig. 4.31. Beside single breakdown path (Fig. 4.31a.)) branching of arcs occurred quite often (c.f. Fig. 4.31 b.)). In one of 91 breakdowns one picture was taken which showed two breakdowns. One occurred on the main the second on the arcing contacts (c.f. Fig. 4.31c.)). The recording of two breakdowns in one experiment led to a failure in the arc root point detection algorithm what resulted in the reconstruction of a dot in between the electrodes in Fig. 4.30.

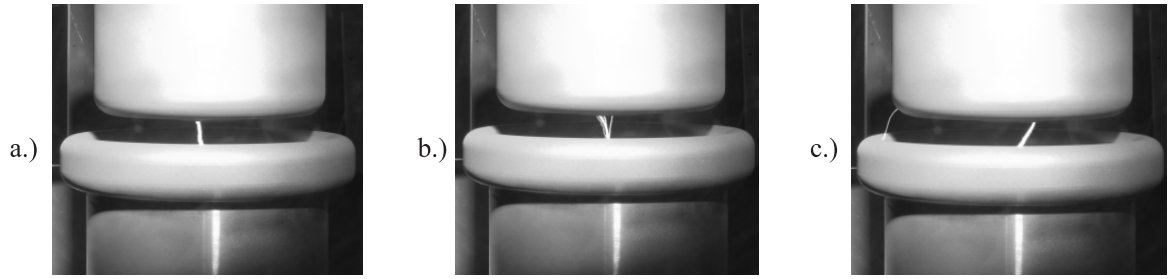

Figure 4.31.: Differing breakdown paths recorded during breakdown experiments on the complete contact system with VFT voltage: Straight a.), branched b.) and double breakdown c.)

4.6. Discussion

The simulation using the circuit breaker model is a well suited and intuitive tool to evaluate very fast transient phenomena associated with switching actions in high voltage circuit breakers. Analysis revealed the influence of certain parameters of the circuit breaker geometry on VFT overvoltages.

In the single interrupting unit, the occurrence of VFT across the main contacts of the circuit breaker as the result of a pre-ignition across the arcing contacts was analyzed. The important parameters are either belonging to the inner structure of moving and fixed contact or to adjacent parts, i.e. load elements.
The short circuit connection between arcing contact and moving contact on both contact sides was identified to have an impact on amplitude and duration of VFT occurring across the main contacts. Simulations with values between $0 \ldots 100\,\mathrm{nH}$ showed an increase of VFT amplitude and duration with rising inductance. In realistic circuit breakers this short circuit connection is usually designed as low inductive and low resistive element to guarantee an undistorted current commutation during opening. Thus, the design of a high inductive connection in future designs is not expected.
An increasing inner length and surge impedance of moving and fixed contact side showed also an increased VFT. In order to get a significant influence caused by the length ($v = c_0$) of these transmission lines based on the speed of breakdown in real applications ($2\,\mathrm{ns}$), it should be bigger than $1\,\mathrm{m}$. This requirement contradicts the general trend towards compact future circuit breakers. An increasing surge impedance of the contacts implies either an increased outer radius and/or a decreased inner radius of the coaxial transmission system. In realistic circuit breakers both values are restricted. For compactness and dielectric strength the outer radius has to be small and for optimal current carrying the inner radius has to be big.
The biggest influence on VFT occurrence in circuit breakers with single unit interrupter was caused by the introduction of lumped capacitors at the terminals of the circuit breaker. The influence increased with opposed sizes of the capacitors. In service such an arrangement is represented by a circuit breaker equipped with a line to ground capacitor. A realistic worstcase simulation showed a maximum amplitude across the main contacts with $0.5\,\mathrm{V}$ amplitude (excitation: $1\,\mathrm{V}$) and approximately $3\,\mu\mathrm{s}$ duration. Although any damping elements were neglected, none of the simulations performed resulted in VFT overvoltage exceeding 1pu across the main contacts. A VFT across the main contacts which was triggered by a breakdown at the arcing contacts reached a peak to peak voltage higher than the voltage before breakdown, but it was always an oscillation around zero. Therefore the peak value did not exceed the initial stress.
The results of the breakdown experiments to evaluate the effects of VFT on the main

contact breakdown probability distribution in a single interrupter unit supported this argumentation. Within 813 breakdown experiments no breakdown occurred on the main contacts. It has to be pointed out that only a single arrangement with a high coordination factor was tested. This setup is not comparable to any other experiments presented in this book.

In the double interrupting unit, the occurrence of VFT across the main contacts of the circuit breaker as the result of a pre-ignition in the adjacent switching unit was analyzed. Therefore, the voltage across the contact system is at least as high as 1 V. The differences in voltage across main and arcing contacts were caused by the same parameters as in the single interrupting unit but their variation had no significant impact. The influence of load elements on amplitude and duration of the VFT was far more important. Simulations with adjacent surge impedances with opposed values had the biggest influence and a worstcase simulation showed an amplitude of 1.65 V (exciting: 1 V) and approximately 3 μs duration. Noteworthy even though the simulated VFT did show a high amplitude and frequency, no major difference between potential drop across arcing and main contacts could be observed.
The results of the breakdown experiments to evaluate the effects of VFT on the main contact breakdown probability distribution in a double unit interrupter are in line with these findings. Measurement of the voltage applied showed a VFT voltage superimposed to the lightning impulse voltage shape. The VFT promoting setup had a breakdown voltage which was significantly decreased by 8% and 2% depending on the voltage polarity applied and compared to the same contact system subjected to lightning impulse voltage stress only. Further, a dramatic increase in breakdown occurrence on the main contacts (69%) was detected, compared to the same contact system subject to lightning impulse voltage stress only (3.5%). Since the simulation showed no significant potential difference between arcing and main contact, changes in the electrodynamic field distribution are presumably not the underlying cause. Concerning the high frequency breakdown mechanism in SF_6, the withstand voltage is lower if leader formation is promoted by a displacement current. Due to their larger area, the main contacts showed a much higher stray capacitance compared to the arcing contacts. This fact would lead to a higher displacement current in the event of a high frequency voltage oscillation. It was not clear whether the high frequency breakdown mechanism led to the decrease in breakdown voltage but it was doubtless responsible for a significant change in breakdown location distribution. Further it was not clear whether the occurrence of VFT or a different cause led to the record of more than one arc during one experiment.

The characterization of a grading capacitor revealed its action as a short circuit from a frequency of a few MHz up to about 120 MHz. In this frequency range the grading

capacitor mitigated the effect of VFT since the short circuit did not allow a voltage drop across the circuit breaker contact. Depending on the inner structure of the grading capacitor frequency bands existed where they acted as an open circuit (200 MHz). VFT with corresponding frequency were therefore not affected by grading capacitors. The simulation incorporating the grading capacitor model with limited reliability, showed a significantly lower amplitude compared to the identical setup without grading capacitor. Irrespectively, the VFT across the main contacts of the circuit breaker exceeded 1 V (excitation: 1 V).

Concluding, a VFT stress with negative polarity at low coordinated contact sides had a higher breakdown voltage than the opposite polarity but a probability for main contact breakdown bigger than 50%. According to this mechanism two different scenarios depending on the construction type of double unit circuit breaker can be derived:
In a metal-clad circuit breaker the contact systems are aligned symmetrically since they move in the same direction simultaneously. Therefore a pre-ignition in the first unit, causing VFT onto the second unit may only happen at the undesirable polarity if the same scenario applies as described in section 3.6. In this case the breakdown probability at the main contacts is higher than at the arcing contacts.
In live tank circuit breakers the contact systems are aligned asymmetrically because the accelerating control rod is installed in the support in between the switching units. In this case a pre-ignition according to the weak voltage polarity induces VFT onto the succeeding contact system with the critical polarity. Obviously this effect is damped significantly by the switching arc resistance, the grading capacitors and the suboptimal propagation in live tank systems. However, this mechanism becomes critical and a potential risk when the boundary conditions mentioned do not persist in the future.

5. Conclusion and Outlook

The present work aimed to increase the understanding of the dielectric coordination of high voltage circuit breakers. Two different concepts distorting the dielectric coordination were investigated: An implicit distortion by unforeseen overlap of breakdown probability curves of single contacts when combining them to a contact system and an explicit distortion by the development of VFT in a circuit breaker.

Implicit distortion was investigated by electrostatic field calculation and by the development and construction of an experimental test stand to accurately define the breakdown probability distribution of SF_6 insulated contacts. It could be concluded that the breakdown probability distribution of a combined contact system can not easily be extrapolated out of the probability of the individual single contacts. Further, the distribution of the locations of the breakdowns was strongly dependent on the voltage polarity applied.

Explicit distortion was investigated by the development, implementation and validation of an equivalent network model of a high voltage circuit breaker. Using this model, transient simulations revealed the occurrence of certain VFT overvoltages based on the geometrical characteristics of the circuit breaker. It was concluded that no significant VFT arise in a single interrupting unit breaker, but its effect could become severe in a double unit interrupting unit. By conducting corresponding breakdown experiments, at the double unit breaker setup a major change in the distribution of breakdown location was detected. This effect is likely to be mitigated by the application of grading capacitors across the contacts.

Based on these findings, design criteria for future gas-insulated high voltage circuit breaker contact systems can be extended: If the maximum electric field at certain electrodes is used as coordination and breakdown criteria it has to be evaluated through breakdown experiments with the combined contact system. Analysis of single contacts and extrapolation of these results to combined contact systems does not result a correct design.
Further, the breakdown probability on the main contact system can generally be decreased by coordinating both sides of the contact system.

Although interesting conceptual issues were derived within this work, a consistent and quantitative explanation for the phenomena detected, could not be found. Future work may address some of the following questions:

- The breakdown probability curve of combined contact systems may be described by

using maximum electric field, individual contact distance and the effective electrode area. A dependence of the breakdown voltage on these parameters can be found by further experimental investigation and theoretical analysis.

- The influence of the voltage polarity on the location of breakdown (arcing or main contact) remained an unexplained finding.

- Generally, an increasing coordination factor is favorable for the dielectric coordination of circuit breaker contacts. It was found that different coordination factors on different contact sides influenced the location of breakdown occurrence significantly. However, this hypothesis is based on few data and needs further investigation and clarification.

- The investigation of VFT voltage development using an equivalent network model posed a simple and accurate tool to evaluate potential developments within the circuit breaker. However it gave no information about the size of the electric field within the circuit breaker. To analyze a specific situation, the implementation of an electrodynamic FEM-simulation would show a clearer image.

- The dependence of breakdown location on the voltage shape (lightning impulse vs VFT) was explained by the onset of a breakdown according to the high frequency mechanism in SF_6. Further investigation and quantitative argumentation should set this hypothesis on a solid argumentative basis.

- The influence of grading capacitors on the breakdown development in a double unit circuit breaker was only theoretically derived. These findings need to be confirmed by actual breakdown experiments.

A. Abbreviations and Symbols

A.1. Abbreviations

VFT Very Fast Transient Voltages

IEC International Electrotechnical Commission

GIS Gas Insulated System

DC Direct Current

AC Alternating Current

FEM Finite Element Modeling

pu per unit

SF_6 Sulfur Hexafluoride

A.2. Symbols

η	Field efficiency factor [1]
E	Electric field [V/m]
E_0	Homogeneous electric field [V/m]
α^*	effective ionization coefficient [1/m]
V	Voltage [V]
I	Current [A]
γ	Propagation factor [1/m]
p	Probability
p	Pressure [MPa]
ρ	Conductivity [Ω/m]
f	Frequency [Hz]
c_0	Speed of light [m/s]
ϵ_0	Dielectric permittivity [F/m]
ϵ_r	Relative dielectric permittivity [1]

μ_0	Permeability [N/A^2]
μ_r	Relative permeability [1]
λ	Wavelength [m]
ω	Harmonic frequency [1/s]
r	Radius [m]
d	Diameter or distance [m]
δ_s	Skin depth [m]
Z_w	Surge impedance [Ω]
S	Scattering parameter [1]
R'	Resistance per length [Ω/m]
L'	Inductance per length [H/m]
G'	Conductance per length [S/m]
C'	Capacitance per length [F/m]

B. Contact Separation vs. Contact Distance

To clarify the terminology of contact travel l, contact separation s and contact distance d the three parameters are depicted in Fig. B.1.
Contact travel l is usually used to describe the movement of the breaker. Therefore it includes the overlap of the contacts in closed position. Contact separation s is the distance between the contacts if both were plane electrodes whereas contact distance d is the shortest distance between the electrodes. Noteworthy s can become zero even if the contacts do not touch. The parameter d can be calculated as follows:

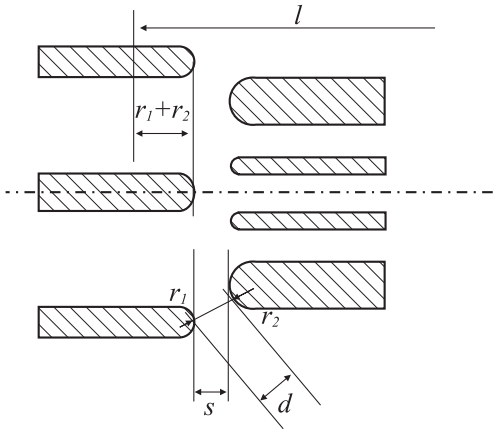

Figure B.1.: Schematic contact system, explaining contact travel l, contact distance d and contact separation s

$$d = \sqrt{(r_1 + r_2)^2 + (r_1 + r_2 + s)^2} - (r_1 + r_2) \tag{B.1}$$

C. Electric Field Calculation

Every electric field calculation shown in this book was optained using the FEM-Tool COMSOL Multiphysics (V3.5a). The results of these calculations is very sensitive on the input and boundary values, which are summarize here:

- Application mode: Electrostatics (emes), 2D axial symmetry
- Subdomain setting: $\rho = 0$, $\varepsilon_r = 1$
- Boundary settings: c.f. Fig. C.1
- Standard mesh generator, usually $>$ 30'000 elements.
- Data extraction by PostProcessing - cross section plot parameters

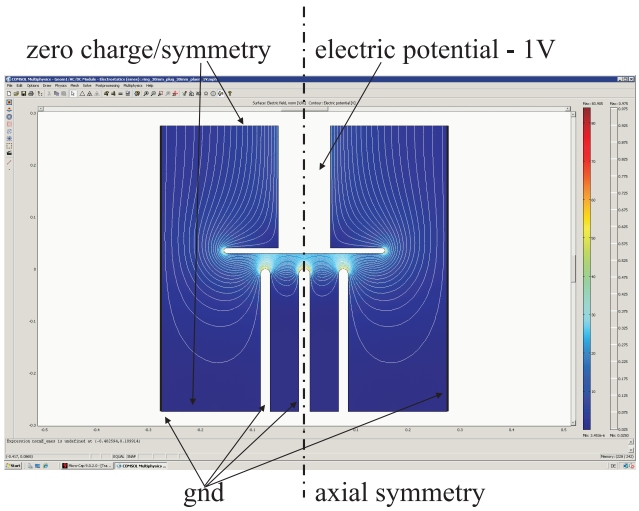

Figure C.1.: Boundary settings for basics circuit breaker contact geometry

D. Ion Velocity

A rough estimation of the ion drift velocity [12] in an SF6 vessel can be calculated:

$$v_{SF_6^-} = bE \qquad b = \text{Ion Mobility Factor} \tag{D.1}$$

Assuming a Voltage of 100 kV across the contacts in Fig. 3.2, a maximum electric field of 122 kV/cm would result. The ion mobility at 0.6 MPa is around 0.4 cm^2/Vs and allows an ion drift velocity of 488 m/s.
Assuming DC-voltage and a homogeneous electric field, an ion can travel across the gap in Fig.3.2 in approximately 20.5 μs. Accordingly the application of the voltage for 2 μs would results in travel of about a tenth of gap.
Through application of an electric field in the same order of magnitude for several seconds, it can be concluded that all the ions within the gap are accelerated towards and recombined at the respective electrode.

Bibliography

[1] "Energy and environment report 2008," European Environment Agency, EEA Report 6, 2008.

[2] D. Amer, C. Fawdreay, C. Flurscheim, S. Gonek, M. John, M. Kennedy, D. Legg, E. Maggi, J. Morton, M. Reece, and J. Sullivan, *Power circuit breaker theory and design*, 2nd ed., C. Flurscheim, Ed. Peter Peregrinus Ltd., 1982.

[3] "IEC 60071-1, Insulation co-ordination, Part 1: Definition, principles and rules," International Electrical Comittee, Tech. Rep., 2010.

[4] A. Schwaiger, *Elektrische Festigkeitslehre*, 2nd ed. Verlag von Julius Springer, 1925.

[5] E. Kuffel, W. Zaengl, and J. Kuffel, *High Voltage Engineering*, 3rd ed. Elsevier Ltd., 2000.

[6] D. Blair, P. Chatterton, J. Craggs, J. Dutton, M. Grey, R. Holmes, J. Rees, R. Sigmond, and R. Waters, *Electrical Breakdown in Gases*, J. Meek and J. Craggs, Eds. John Wiley and Sons, 1978.

[7] M. Kriegel, X. Zhu, R. Alexander, F. Chille, M. Glinkowski, A. grund, F. Heil, H. Kim, R. Robin-Jouan, L. van der Sluis, R. Smeets, and T. Uchii, "Simulations and Calculations as Verification Tools for Design and Performance Assessment of High-Voltage Equipment," *Electra*, no. 234, pp. 13–18, October 2007.

[8] S. A. Boggs, F. Chu, N. Fujimoto, A. Krenicky, A. Plessl, and D. Schlicht, "Disconnect switch induced transients and trapped charge in gas-insulated substations," *IEEE Transactions on Power Apparatus and Systems*, vol. PAS-101, no. 10, pp. 3593–3602, 1982.

[9] H. Raether, *Electron avalanches and breakdown in gases*. Butterworth, London, 1964.

[10] Pedersen, A. and McAllister, W. and Crichton, G.C. and Vibholm, S., "Formulation of the Streamer Breakdown Criterion and its Application to Strongly Electronegative Gases and Gas mixtures," *ETZ-A 67*, pp. 395 – 402, 1984.

[11] J. Kindersberger, "The statistical time-lag to discharge inception in SF_6," Ph.D. dissertation, TU Munchen, 1986.

[12] W. Mosch and W. Hauschild, *Hochspannungsisolierung mit Schwefelhexafluorid*, M. Kahle, Ed. Dr. Alfred Huethig Verlag, Heidelberg, Basel, 1979, vol. 1.

[13] A. Kuechler, *Hochspannungstechnik*, 2nd ed. Springer, Berlin Heidelberg New York, 2005.

[14] A. Pederson, "The Effect of Surface Roughness on Breakdown in SF_6," *IEEE Transaction on Power Apparatus and Systems*, vol. 94, no. 5, pp. 1749–1754, September 1975.

[15] W. Boeck, "Volumen-Zeit Gesetz beim Stossspannungsdurchschlag von SF_6," *ETZ-A 96*, pp. 300–305, 1975.

[16] M. Seeger, L. Niemeyer, and M. Bujotzek, "Partial Discharges and Breakdown at Protrusions in Uniform Background Fields in SF_6," *Journal of Physics D: Applied Physics*, vol. 41, 2008.

[17] L. Niemeyer, L. Ullrich, and N. Wiegart, "The Mechanism of Leader Breakdown in Eletronegative Gases," *IEEE Transactions on Electrical Insulation*, vol. 24, no. 2, pp. 309–324, 1989.

[18] H. Hiesinger, "Der Hochfrequenz-Durchschlagsmechanismus in SF_6 bei schwingenden transienten Überspannungen," Ph.D. dissertation, TU Munchen, 1991.

[19] D. Buchner, "Der Energie-Durchschlag-mechanismus in in SF_6 bei steilen transienten Überspannungen," Ph.D. dissertation, TU Munchen, 1995.

[20] W. Boeck, W. G. 15.03, and S. C. 15, "GIS Insulation Properties in Case of VFT and DC stress," Cigre, Tech. Rep., 1996.

[21] K. Tekletsadik and L. Campbell, "SF_6 Breakdown in GIS," *IEE Proceedings - Science, Measurement and Technology*, vol. 143, no. 5, pp. 270 – 276, 1996.

[22] W. Hauschild and W. Mosch, *Statistical Techniques for High-Voltage Engineering*. Peter Peregrinus Ltd., 1992, vol. 1.

[23] "IEC 60060-1, High-voltage test techniques - Part 1: General definitions and test requirements," International Electrical Comittee, Tech. Rep., 2006.

[24] W. Dixon and A. Mood, "A method for obtaining and analysing sensitivity data," *Journal of American Statistical Association*, pp. 109–126, 1948.

[25] M. Fisz, *Wahrscheinlichkeitsrechnung und mathematische Statistik*. Berlin: Deutscher Verlag der Wissenschaften, VEB, 1965.

[26] W. Stevens, "Distribution of groups in a sequence of alternatives," *Annals of Eugenics*, vol. 9, pp. 10–17, Jan 1939.

[27] W. Wallis, "Rough and ready statistical tests," *Industrial Quality control*, vol. 8, pp. 35–40, 1952.

[28] L. Sachs, *Statistische Auswertungsmethoden*. Springer Verlag, Berlin, 1968.

[29] W. Wallis and G. Moore, "A significance test for time series analysis," *Journal of American Statistic Association*, vol. 36, pp. 401–409, 1941.

[30] R. G. Baumgartner, "Untersuchungen ueber die Gültigkeit des Ähnlichkeitsgesetzes in Schwefelhexafluorid," Ph.D. dissertation, ETH Zurich, 1977.

[31] C. Lederle, "Isoliervermögen SF_6-isolierter Elektrodenanordnungen mit dielektrischer Beschichtung," Ph.D. dissertation, TU Muenchen, 2008.

[32] C. Lederle and J. Kindersberger, "The Influence of Surface Roughness and Dielectric Coating on AC and DC Breakdown Voltage in SF_6," *Proceedings of the XIVth International Symposium on High Voltage Engineering*, 2005.

[33] N. Wiegart, L. Niemeyer, F. Pinnekamp, W. Boeck, J. Kindersberger, R. Morrow, W. Zaengl, M. Zwicky, I. Gallimberti, and S. Boggs, "Inhomogeneous Field Breakdown in GIS - The Prediction of Breakdown Probabilities and Voltages - Part I," *IEEE Transactions on Power Delivery*, vol. 3, no. 3, pp. 923 –930, July 1988.

[34] N. Fujimoto, S. Boggs, and G. Stone, "Mechanisms and Analysis of Short Risetime GIS Transients," *Proceedings of CIGRE Symposium on New and Improved Materials for Electrotechnology*, pp. 1010–03/1–6 600, 1987.

[35] N. Fujimoto and S. Boggs, "Characteristics of GIS Disconnector-induced Short Risetime Transients Incident on Externally Connected Power-System Components," *IEEE Transactions on Power Delivery*, vol. 3, no. 3, pp. 961–970, 1988.

[36] D. Povh, H. Schmitt, O. Völcker, and R. Witzmann, "Modelling and Analysis Guidelines for Very Fast Transients," *IEEE Transactions on Power Delivery*, vol. 11, no. 4, pp. 2028 – 2034, October 1996.

[37] R. Witzmann, "Schnelle transiente Spannungen in metallgekapselten SF_6-isolierten Schaltanlagen," Ph.D. dissertation, TU Munchen, June 1989.

[38] WG33.02, "Guidelines for representation of Network Elements when calculating transients," Cigre, Report, 1990.

[39] X. Xu, S. Jayaram, and S. Boggs, "Prediciton of Breakdown in SF_6 under Impulse Conditions," *IEEE Transaction on dielectrics and Electrical Insulation*, vol. 3, no. 6, pp. 836–842, December 1996.

[40] N. Wiegart, L. Niemeyer, F. Pinnekamp, W. Boeck, J. Kindersberger, R. Morrow, W. Zaengl, M. Zwicky, I. Gallimberti, and S. Boggs, "Inhomogeneous Field Breakdown in GIS - The Prediction of Breakdown Probabilities and Voltages - Part II," *IEEE Transactions on Power Delivery*, vol. 3, no. 3, pp. 931 –938, July 1988.

[41] W. Baechtold, *Lineare Elemente der Hoechstfrequenztechnik*, 2nd ed. vdf, Hochschulverlag AG, ETH Zurich, 1998, vol. 1.

[42] C. Desoer and E. Kuh, *Basic Circuit Theory*. McGraw-Hill Book Company, 1969.

[43] T. Lee, *Planar mocrowave engineering*. Cambridge University Press.

[44] N. Marcuvitz, *Waveguide handbook*. Peregrinus London, 1993.

[45] O. Zinke and H. Brunswig, *Lehrbuch der Hochfrequenztechnik*, 2nd ed. Springer-Verlag Berlin, Heidelberg, New York, 1973, vol. 1.

Curriculum Vitae

Philipp Simka

Personal Data

Name	Philipp Simka
Address	Rotwandstrasse 53
	8004 Zurich
	Switzerland
Phone	+41 (0)78 764 01 37
e-Mail	psimka@alumni.ethz.ch

Date of birth	16. December 1978
Place of birth	Chur, Switzerland
Citizenship	Swiss and German
Matrial status	married

Education

07/2006 - present	PhD, ETH Zurich, Switzerland Institute of Energy Transmission and High Voltage Laboratory Title of thesis: *Dielectric Coordination of High Voltage Gas Circuit Breakers*
10/1998 - 05/2005	MSc Electrical Engineering, ETH Zurich, Switzerland Major field of studies: Energy Transmission and High Voltage Technology Electromagnetic Fields and Microwave Electronics Final grade: 5.5 Title of master thesis: *Using Transit Times of Partial Discharges* Grade: 6 Honored with the prize: *Premio IM 2005*
06/1998 - 10/1998	Military Service, Swiss Army Salvation Troups

Working Experience

03/2006 - 06/ 2006	ABB High Power Laboratory, Ludvika, Sweden Lab assistant, internship
05/2005 - 11/2005	VSETH, Zurich, Switzerland Project Manager *Opening Student House*
07/2003 - 09/2003	Brasser AG, Zizers, Switzerland Light- and Soundengineer
07/2002 - 08/2002	Etablissements Slama Frères, Oued Ellil/Tunis, Tunisia Software developer, internship

Additional Qualifications

Languages:	German - mother tongue English - fluent French - good Italian - good
Computer skills:	MacOSX, Windows, Linux Standard applications for office, data analysis and presentation Experienced in: Matlab, Microcap, Comsol, Latex, Corel Draw Basic knowledge in: C, C++, Java

Extracurricular Activities

02/2004 - 02/2006	Board member of Challenge Snow-Fun-Club, VSETH
04/2004 - 04/2008	Member of the supervisory board of Woko Student housing commission, ETH
10/2003 - 02/2004	Undergraduate teaching assistant Lecture *Basic circuit theory* Institute of Energy Transmission and High Voltage Laboratory
10/2003 - 02/2004	Undergraduate teaching assistant Lecture *Basic electro technique* Power Electronic Systems Laboratory
10/2000 - 10/2003	Vice president, Board member of Amiv Association of electrical and mechanical engineering students

Hobbies

Sports	Snowboarding, Mountain Biking
Other	Eventmanagement, interior and light design

List of Publications

Measuring Breakdown Probabilities of SF_6 Insulated Low Inhomogeneous Electrodes
Simka P., Franck C.M.
Conference Record of the XVIII International Conference on Gas Discharges and Their Applications, GD 2010

A Complete Circuit Breaker Model for Calculating Very Fast Transient Voltages
Simka P.
Conference Record of the 2010 IEEE International Symposium on Electrical Insulation, 2010.

An Approach to Model Very Fast Transients in High Voltage Circuit Breakers
Simka P.
Conference Record of the 2008 IEEE International Symposium on Electrical Insulation, 2008. ISEI 2008. Page(s): 449 - 452